Università degli Studi di Napoli
"Federico II"

Dottorato in Scienze Chimiche

XXVIII Ciclo

Iron Oxide Nanoparticles as MRI Contrast Agents: a Physico-chemical Insight

Ph. D. candidate

Alessandra Luchini

Tutors: Prof. Luigi Paduano and Prof. Gerardino D'Errico

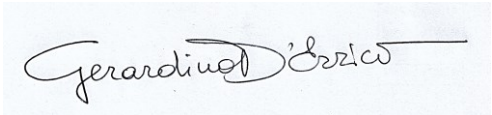

2013-2016

Preface

This Ph. D. thesis is the result of the work carried out during the last three years in the field of the physical chemistry of colloids and interfaces, with particular focus on inorganic nanoparticles. Even if the following discussions are mainly devoted to iron oxide nanoparticles, learning from the literature and testing modified protocols, the synthesis of different metal and metal oxide nanoparticles, such as gold and zinc oxide nanoparticles, was object of research. The acquired chemical synthesis skills were complemented by collecting experience in the structural characterization of colloidal systems by means of light and neutron scattering. Thus, both the preparation and the characterization of nanoparticle-based systems was explored gaining knowledge in different scientific fields.

This Ph. D project was partially funded by MIUR and supported by the Institut Laue Langevin (ILL), the Julich Center for Neutron Science (JCNS) and ISIS at the STFC Rutherford Appleton Laboratory, providing beam time for the experiments involving neutrons. Furthermore, other experiments were also performed with the support of the Partnership for Soft Condensed Matter (PSCM) laboratories at ILL.

Contents

Introduction

Nanoscience and Nanotechnlogy are research fields based on the development, the study and the technological exploitation of materials with nanometer size. In this respect, inorganic nanoparticles made of metal, semiconductors or magnetic materials play a pivotal role with their optical electrical and magnetic properties being radically different from the corresponding bulk material. Indeed, their technological applications are based on the possibility of finely tuning the properties of the nanoparticles according to their size.

Inorganic nanoparticles are clusters of atoms. Metal oxide nanoparticles can be composed by atoms of the same metal element or by alloys of different metals. On the other hand, in the case of metal oxide nanoparticles, oxygen and metal atoms are arranged in space in the form of nanocrystals. Even if composed by several atoms, the restricted size of the nanoparticles with respect to bulk materials is responsible for peculiar properties frequently relying on quantistic effects. A classical example is represented by gold nanoparticle suspensions exhibiting the characteristic dark-red color ascribed to visible light absorption by nanoparticle surface plasmons. The specific wavelength corresponding to the maximum in the absorbance spectrum is determined by the radius of gold nanoparticles.

Considering the great size reduction of the devices developed in the last years for biomedical applications, it is possible to state that also medicine is getting more and more "*nano"*. Owing to their optical, electrical and magnetic properties, the inorganic nanoparticles are exploited in highly sensitive diagnostic techniques and combined diagnostic and therapeutic applications. Specifically, SuperParamagnetic Iron Oxide Nanoparticles (SPIONs) are reported as effective Magnetic Resonance Imaging (MRI) contrast agents. Furthermore, their ability to produce local heating when exposed to an external magnetic field makes them high-promising candidates for anticancer therapy in the hyperthermia treatment. According to these very attractive applications, recent scientific research produced a large variety of synthetic pathways for the obtainment of SPIONs. In particular, SPION surface modification has emerged as imperative to induce properties such as stability in aqueous media and biocompatibility.

On the grounds of the reports recently published in the literature, the objective of this Ph. D. project was the establishment of a robust strategy for the preparation of SPION aqueous suspensions suitable for biocompatible applications. For this purpose, a novel functionalization strategy based on

hydrophobic interaction was developed to stabilize SPIONs in aqueous media. The explored functionalization strategy avoids any purification step and is extremely versatile.

The structure and the composition of nanodevices are critical variables for their utilization in any technological field. Consequently, the here presented project was also aimed at the identification of a suitable combination of different techniques for the assessment of physical properties of the prepared SPIONs. In particular, the performed characterization was decisive for the rational design of functionalized SPIONs with controlled size considerable and biocompatibility. The investigation of the prepared functionalized SPIONs was enriched by defining a physico-chemical approach suitable for the characterization of their interaction with biologically relevant systems, i.e. lipid bilayers mimicking the plasma cellular membrane. This Ph. D. project took advantage of collaborations with research groups in pharmaceutical and biomedical fields to test an effective application of the prepared SPIONs. Hence, all the steps from the synthesis to the *in vivo* application were explored.

In Chapter 1, the main results recently published in the literature with regard to the synthesis and technological applications of SPIONs are discussed. A detailed description of the preparation protocols adopted for the obtainment of functionalized SPIONs together with a concise presentation of the instrumentations used for their characterization is reported in Chapter 2. The structure and the composition of the prepared nanoparticles is investigated in Chapter 3. Once the obtainment of effective SPIONs was verified, functionalized SPIONs were prepared using different amphiphilic molecules (Chapter 4). As a result, monodispersed functionalized SPIONs with high biocompatibility and effective activity as MRI contrast agents were obtained (Chapter 5). Nevertheless, reliable information is often required about the behavior of nanoparticles in biological systems. For this purpose, the interaction between the functionalized SPIONs and lipid bilayers mimicking of the plasma cellular membrane was characterized. (Chapter 6). Finally, as a further step in the development of functionalized SPIONs for biomedical applications, the versatility of the optimized functionalization strategy was exploited to prepare prototypes of theranostic nanoparticles as well as dualmodal imaging contrast agents (Chapter 7). Besides the discussion of the experimental results, a brief theoretical presentation of some of the used characterization techniques is reported in the appendices.

Chapter 1 - *SPIONs and their Applications in Biomedicine*

SuperParamagnetic Iron Oxide Nanoparticles (SPIONs) have great potentialities for several technological applications ranging from data storage to biosensing, diagnostic and cancer therapy. Due to all these attractive applications, in the last 10 years an increasing number of synthetic protocols were published for the preparation of suitably designed SPIONs. The principal synthetic and functionalization routes recently proposed for SPIONs as Magnetic Resonance Imaging (MRI) contrast agents, multimodal imaging devices and nanocarriers for potential drugs are discussed here. Functionalized SPIONs have been approved by the United States Food and Drug Administration (FDA) as MRI contrast agents for clinical use owing to their high *in vivo* stability and low toxicity. Even if a great amount of *in vivo* experiments have been published, little information is available about their behavior in biological systems at the molecular level. Recently, the scientific research has been focused on the characterization of the interaction between inorganic nanoparticles and their targeted biological systems, such as proteins and cellular membranes. Some of the main results obtained in this field are here reported.

1.1 SuperParamagnetic Iron Oxide Nanoparticles (SPIONs).

The most important iron oxides present in nature are Fe_3O_4, magnetite (also known as black iron oxide, magnetic iron oxide, ferrous ferrite or Hercules stone), γ-Fe_2O_3, maghemite, and α-Fe_2O_3, hematite (also known as ferric oxide, iron sesquioxide, red ochre, specularite, specular iron ore, kidney ore, or martite). Maghemite is a metastable oxide with respect to magnetite and hematite, which is frequently encountered as a solid solution together with magnetite. Both magnetite and maghemite are characterized by ferromagnetic properties and an inverse spinel structure.

In magnetite, the oxygen atoms form a cubic closed packed arrangement with Fe (III) ions randomly distributed in the tetrahedral and octahedral sites (Figure 1.1.1). On the other hand, in maghemite, the oxygen atoms still form a cubic closed packed arrangement, but only two-thirds of the available sites for Fe(III) ions are filled. Thus, maghemite has a very similar crystalline structure with respect to magnetite, but vacancies in the cationic sublattice are present. This difference makes very difficult to distinguish the two iron oxides from a crystallographic point of view.[1, 2]

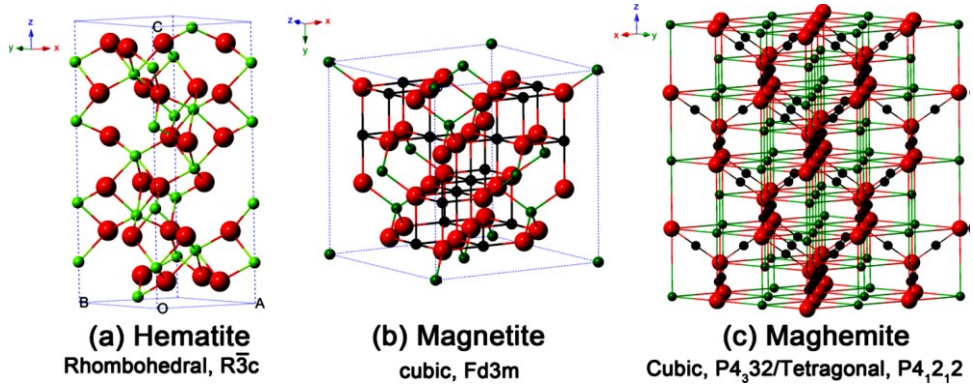

Figure 1.1.1: *Crystal structure and crystallographic data of the hematite, magnetite and maghemite (the black ball is Fe^{2+}, the green ball is Fe^{3+} and the red ball is O^{2-}). [2]*

The magnetic properties of a ferromagnetic material can be characterized by measuring its magnetization as a function of the external magnetic field (H). The magnetization (M) arises from the sum of all the atomic magnetic moments within the material. In a bulk ferromagnetic material, the magnetization magnitude is usually less than its theoretical value because the atomic magnetic moments are not all perfectly aligned, but they are organized in domains each having its own magnetization. The number of domains within a ferromagnetic material decreases with its size until a critical size is achieved. Below the critical size, whose value depends on the material composition, a single domain structure is present. The main feature of a single-domain ferromagnetic material is the S-shaped hysteresis loop in the M vs. H plot with an extremely low value of the associated coercive field (H_c).[1]

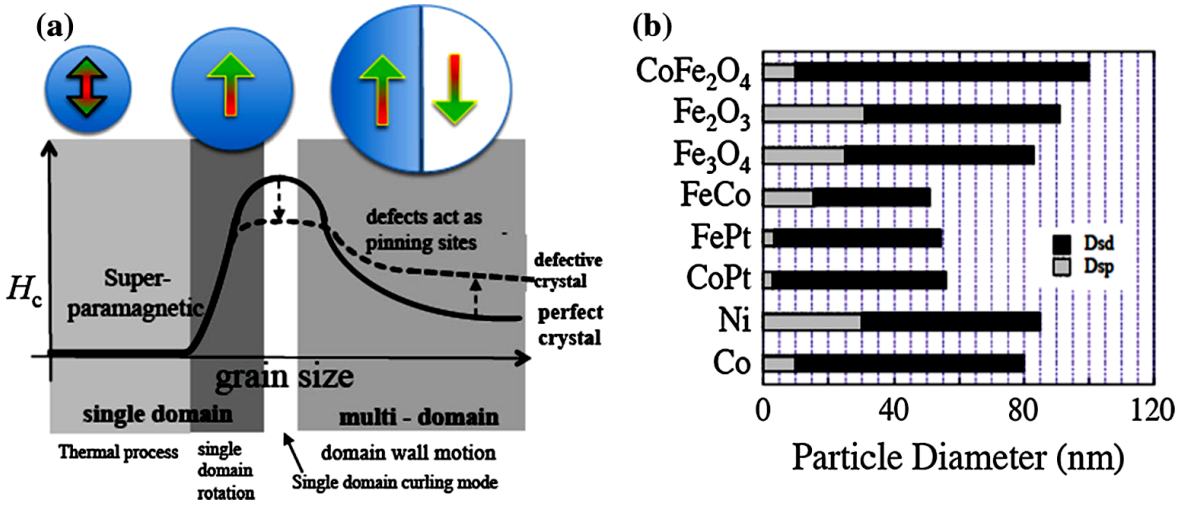

Figure 1.1.2: *Magnetic behavior of nanoparticles of diameter, D, defined as a function of their coercivity represented by H_c. For superparamagnetic particles the characteristic sizes depend on their intrinsic properties; critical sizes for the observation of superparamagnetism for a variety of common ferromagnetic nanoparticles are shown in panel b.[3]*

The prediction of a single magnetic domain in ferromagnetic particles below the critical size was introduced by Frenkel and Dorfman[4] with the critical size corresponding to about 20 nm radius being the typical value for spherical ferromagnetic nanoparticles as calculated by Kittel[5].

From a physical point of view, the magnetic properties of an ensemble of single-domain ferromagnetic materials can be described according to the magnetization at thermal equilibrium analogous to Langevin treatment of atomic paramagnetism. The difference is that instead of dealing with atomic magnetic moments, the magnetic moment of a single-domain ferromagnetic nanoparticle, which contains several atoms, has to be considered. Thus, the magnetization behavior of a single-domain particle in thermodynamic equilibrium at all fields is identical to that of atomic paramagnetism, but extremely large susceptibilities are involved.[6] This means that single-domain ferromagnetic particles, such as iron oxide nanoparticles below 20 nm, can exhibit a strong magnetic response to an applied external magnetic field, but their magnetization can be completely removed if the external magnetic field is turned off.

The magnetic behavior of single-domain ferromagnetic particles at thermal equilibrium was termed superparamagnetism by Bean *et al.*in 1959.[6] Fe_3O_4 iron oxide nanoparticles with radius below 20 nm exhibits superparamagnetic behavior and are known as SPIONs (SuperParamagnetic Iron Oxide Nanoparticles).

The magnetic moment orientation of SPIONs is randomized at room temperature in the absence of an external magnetic field. If the magnetization of SPIONs is measured as a function of the temperature, it is possible to identify a characteristic temperature, known as blocking temperature T_B, at which the nanoparticles become superparamagnetic.[7]

$$T_B = \frac{KV}{25K_B} \tag{1.1.1}$$

As shown in equation (1.1.1), where K is the magnetic anisotropy constant and K_B is the Boltzmann constant, the value T_B depends on the particle volume V.

The size of a SPION has a strong influence on its magnetic property. When the nanoparticle diameter is below 3 nm, SPION magnetic property changes drastically to the simple paramagnetic behavior.[8] This size effect is ascribed to the spin property of the atoms present at the SPION surface. Indeed, the magnetic spins on SPION surface are disordered and constitute a spin-canted layer with thickness corresponding to about 0.9 nm for Fe_3O_4 nanoparticles. The canted-spin layer reduces the superparamagnetic behavior exhibited by the nanoparticle. Thus, if the particle radius gets close to the characteristic spin-canted thickness, the magnetic behavior will be paramagnetic-like. [9]

1.2 Technological applications of SPIONs.

Because of their unique magnetic properties, together with the possibility of suitably modify their surface, SPIONs have been proposed for a large variety of different technological applications.[8] SPIONs can be used as extractants for the removal of target molecules from aqueous media by exploiting magnetic precipitation techniques.[10] Nanomagnetic systems[11], such as in high density magnetic tape recording, were designed using SPIONs.[12] In addition, SPIONs are extensively utilized as catalysts owing to their high specific surface and accessibility[13]. As an example, SPIONs resulted to be more effective than conventional large-size iron oxide particles for oxidation of CO and oxidative pyrolysis of biomass.[14] But, the most popular application of SPIONs is in biomedicine (Figure 1.2.1), owing to their high biocompatibility and the possibility to be used for simultaneous diagnostic and therapeutic purposes.[9, 15-18]

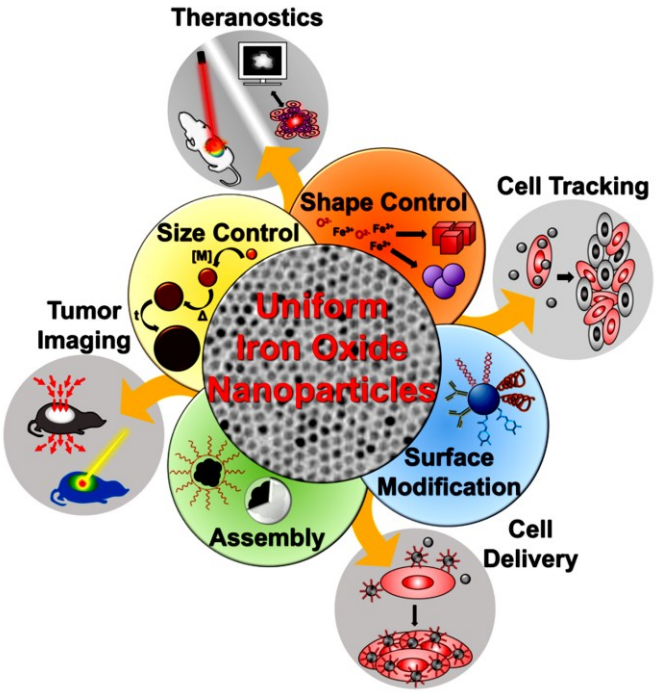

Figure 1.2.1: *Schematic representation of SPION applications in the biomedical field.[8]*

SPIONs have been introduced and approved for clinical use by United States Food and Drug Administration (FDA) as MRI contrast agents.[19] Furthermore, upon anchoring to their surface specific molecules such as chelating agents of radionuclides or fluorescence probes, functionalized SPIONs have also been introduced as multimodal imaging agents.[20] Drugs with specific functionalities can be suitably bound on SPION surface, but also the magnetic properties of the iron oxide core are currently exploited for hyperthermia treatment.[21] Thus, the diagnosis of different pathologies through MRI, or eventually combined imaging techniques, can be performed simultaneously to the appropriate therapeutic treatment.

Hyperthermia is a minimally invasive strategy based on inducing cancer cell death by local heating generation.[22] In the presence of an external alternating magnetic field, SPIONs, due to their magnetization losses, can locally increase the temperature by a few degrees up to 42-46°C. The produced temperature increment turned out to be sufficient for tumor cells to be killed by ablation.[23, 24]

1.3 Synthesis of SPIONs.

Several synthetic routes have been proposed for SPION synthesis.[2, 8, 25-27] Among them, co-precipitation of iron salts, microemulsion method, hydrothermal synthesis and thermal-decomposition of iron precursors are frequently encountered and will be presented here. Further synthetic approaches for the preparation of iron oxide nanoparticles can be found in the references.[2, 25]

The co-precipitation method represents a fast and simple approach for the production of SPIONs. It is based on the reaction of iron salts under alkaline conditions, with pH preferentially ranging from 9 to 14. SPIONs are obtained as a solid precipitate from the aqueous solution. SPION shape and size can be controlled by properly tuning the reaction temperature, the pH, the ionic strength and the composition of the iron salts. The great advantage of this synthetic route is that it can be suitably extended for the large-scale production of SPIONs. However, the prepared SPIONs usually present a broad size distribution.

In the microemulsion method, water-in-oil reverse micelles are employed to produce SPIONs with a narrow size distribution. Like the co-precipitation method, this approach is based on the precipitation of SPIONs from a solution of iron salt, but the reverse micelles act as templates during the nanoparticle synthesis with the precipitation reaction occurring inside the aqueous micelle core. SPION size is determined by the micelle core-size. By changing the surfactant and consequently the micelle radius, SPIONs with tunable size can be obtained. Even if the microemulsion method indeed leads to a good size control, this method is considered as non-biocompatible for the toxicity usually associated to the surfactants.

The hydrothermal synthesis involves iron salt reactions occurring in aqueous solution at high temperature (130-250°C) and pressure (0.3-4 MPa). This kind of reaction is usually performed in sealed containers or in an autoclave because of the required temperature and pressure conditions.

The thermal-decomposition methods require easily available synthesis set-up and produce SPIONs with tunable size and narrow size distribution. The decomposition of an iron oxide precursor in a

high-boiling solvent is exploited to prepare Fe_3O_4 nanoparticles with size < 20 nm. In the heat-up approach (Figure 1.3.1), originally proposed by Heyon *et al.*[28], iron pentacarbonyl ($FeCO_5$) is mixed with a surfactant, such as oleic acid, in octyl ether at 100°C. Subsequently, the temperature is raised to 320°C, corresponding to the boiling point of the solvent. According to the proposed mechanism, $FeCO_5$ initially reacts to form the iron-oleate complex, which acts as the monomer for the formation of Fe_3O_4 nanocrystals.[8]

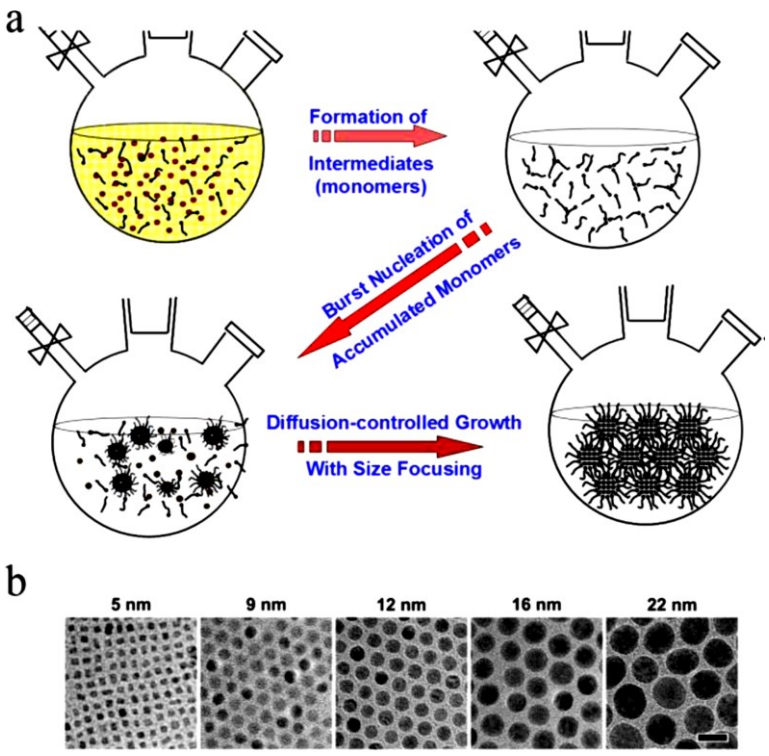

Figure 1.3.1: *(a) Schematic illustration of the "heat-up" method for the synthesis of uniformly sized iron oxide nanoparticles. (b) TEM images of iron oxide nanoparticles synthesized by the "heat-up" method.[8]*

The thermal-decomposition approach proposed by Sun *et al*[29] can be used to obtain Fe_3O_4 nanoparticles with 4 nm, 6 nm and 8 nm radius. 4 nm Fe_3O_4 nanoparticles are obtained through the high-temperature decomposition of the iron oxide precursor, iron acetylacetonate ($Fe(acac)_3$), in the presence of a long-chain alcohol. In particular, the proposed protocol simply requires the appropriate amount of $Fe(acac)_3$ to be mixed with the 1,2-hexadecanedyol and the surfactants, oleic acid and oleylamine (Figure 1.3.2). The solvent proposed for the reaction is phenyl ether and the temperature reaction is 200°C, in the first step (30 min), and subsequently 265°C, in the second step (further 30 min). 1,2 –hexadecanediol acts as a mild reducing agent, while oleic acid and oleylamine molecules are added to bind the surface of the nanoparticles, thus controlling their growth. Indeed, as a result of the published experimental data, the use of oleic acid and oleylamine mixture produces Fe_3O_4 nanoparticles with a higher yield than pure oleic acid.[30] A slightly modifying synthetic protocol

allows Fe_3O_4 nanoparticles with larger size to be synthesize, without increasing their size distribution. 6 nm Fe_3O_4 nanoparticles are produced from the same reagents previously listed, but benzyl ether is used instead of phenyl ether in order to increase the reaction temperature. Furthermore, 8 nm Fe_3O_4 nanoparticles can be prepared according to the same protocol, by using previously synthesized 6nm-Fe_3O_4 nanoparticles as seeds.

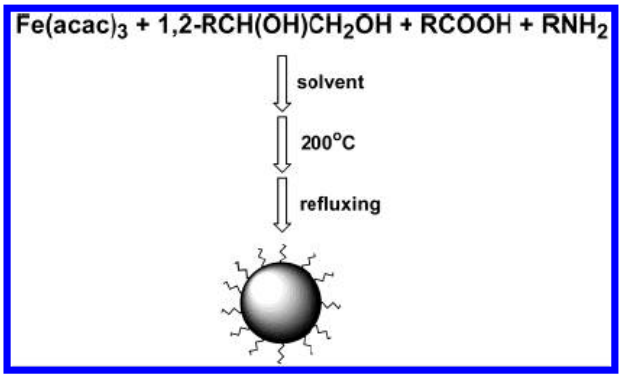

Figure 1.3.2: *Reaction scheme for the thermal decomposition of Fe_3(acac).[30]*

The thermal-decomposition methods are simple synthetic approaches for the production of SPIONs with high yields, tunable size and narrow size distribution. Low cost reactants, such as $Fe(acac)_3$, are employed, leading to a synthetic method suitable for the production of large amounts of SPIONs.

1.4 SPIONs functionalization strategies.

Surface modification of SPIONs, through the formation of an organic or inorganic shell is a frequently encountered approach to obtain stable suspensions of nanoparticles suitable for different applications.[2, 8, 14, 26, 31] SPIONs prepared through the co-precipitation and the hydrothermal methods degrade with time. They are progressively affected by monodispersity loss, due to aggregation, and eventually undergo a susceptibility decrease ascribable to oxidation processes.[2] Thus, post-synthesis surface modifications are necessary to improve SPION stability. In addition, surface modifications can make the SPIONs stable in aqueous suspensions as is mandatory in biomedicine. On the other hand, the thermal-decomposition methods, which already include an *in situ* SPION surface modification and produce nanoparticles directly coated with a stabilizing organic shell, also require a functionalization after the synthesis. As a matter of fact, the stabilizing agents, usually represented by long-chain surfactants, bind SPION surface orienting themselves with the non-

polar acyl chain pointing outward the SPION core. Hence, the SPIONs prepared through thermal decomposition are stable in non-polar solvent but need further surface modifications in order became stable in aqueous media.[26]

Besides the requirement of a water-stable SPION suspension, any biomedical application also wants the SPIONs to be biocompatible. Among the inorganic nanoparticles, SPIONs are the only ones approved for clinical use.[32] Nevertheless, it has often been observed that if SPIONs are not suitably functionalized, their circulation time in living organisms might not be sufficient for them to explicate their activity as MRI contrast agents or carriers for active molecules such as drugs.[33] Several different coatings were proposed to improve *in vivo* performances of SPIONs. As examples from the literature, SPION surface was coated with proteins, such as albumin[34] or hemoglobin[35], surfactants[36] and oligonucleotides[37]. Suitably designed thermoresponsive polymers[38, 39], dextran[40], chitosan[33] and polyethylene glycol (PEG)[41, 42] are also commonly encountered. Furthermore, both doxorubicin[43, 44] and cisplatin[45, 46] have been successfully bound to nanoparticles for the antitumoral therapy. The functionalization strategies adopted in the cited experiments can be divided in two main categories: ligand-exchanged approach and nanoparticle encapsulation into amphiphilic structures. Both these categories denote post-synthesis surface modifications. What follows describes the functionalization of SPIONs in the particular case of the thermal-decomposition method of synthesis.

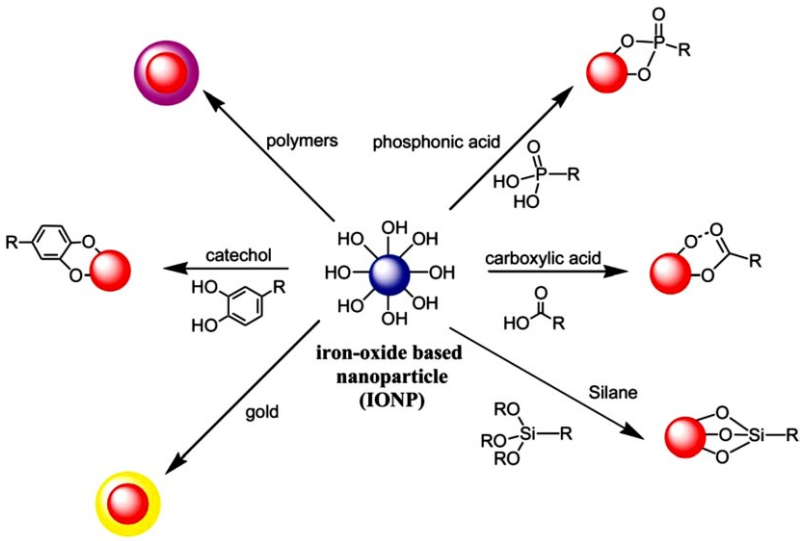

Figure 1.4.1: *Different strategies for the protection/stabilization of IONP (Iron Oxide NanoParticles).[31]*

The ligand-exchange approach requires the selection of an appropriate functionalizing molecule. This molecule must have high affinity for the iron oxide surface, and be able to substitute the preexisting coating. Thus, hydrophobic SPIONs can be converted to water-soluble functionalized SPIONs by choosing a hydrophilic molecule. This approach can produce a stable organic layer, strongly bound

to the nanoparticle surface. Examples are hydrophilic ligands with anchoring groups such as dopamine, carboxylic acids, phosphines and amines, all of which have good affinity for iron oxide surfaces (Figure 1.4.1).[47] In general, the ligand-exchange approach needs a purification step to remove the organic molecules originally binding the SPION surface from the suspension.

The encapsulation of SPIONs into amphiphilic structures is a strategy that keeps the stabilizing layer on the nanoparticles surface and exploits it to introduce a second amphiphilic layer through hydrophobic interaction. The amphiphilic coating can be achieved through redispersion of the precipitated hydrophobic SPIONs with an aqueous solution containing the functionalizing agents. As an alternative, the same functionalization strategy can be enacted at the interface between water and an organic solvent.[47]

The attractive advantage of SPION functionalization through hydrophobic interaction is that different molecules can be easily attached on the SPION surface without any substantial molecular modifications or variations in the functionalization protocol[48]. SPION functionalization through hydrophobic interaction is a suitable approach to combine different functionalities on the same SPION. This is useful to prepare contrast agents for imaging techniques or drug carriers. In the literature on this topic worth citing is the case of PEG molecules modified with phospholipids[8]. PEG-functionalized SPIONs have been approved by the United States Food and Drug Administration (FDA) for diagnostic application.[8] However, recently zwitterionic-surfactant functionalized SPIONs, obtained either *via* ligands exchange or hydrophobic interaction, have been proposed as a valuable alternative to PEG-functionalized SPIONs[49-53]. As reported by Groult *et al.*, zwitterionic-surfactant functionalized SPIONs, obtained by decorating the SPION surface through hydrophobic interaction with a bi-tailed phosphatidylcholine, exhibit a long-circulation time and stability in a wide pH-*range*[49]. Muro *et al*. and Estephan *et al.* have also reported great advantages of zwitterionic-surfactant functionalized SPIONs with respect to PEG-functionalized SPIONs, the former being more stable at high salt concentration and less prone to adsorb proteins[51, 53]. Depending on the zwitterionic-surfactant used for SPIONs functionalization, SPION clustering might occur.

1.5 Imaging techniques and functionalized SPIONs.

MRI is a diagnostic technique with excellent anatomic detail, enhanced soft tissue contrast and high spatial resolution. MRI is based on the same physical principle of Nuclear Magnetic Resonance (NMR) spectroscopy. In the presence of an external magnetic field, a transition between different nuclear spin states can be induced by irradiation with a radiofrequency radiation. During the

relaxation, the original nuclear spin state can be restored through emission of a secondary radiofrequency radiation. Cross-sectional MR images of the tissues are built form the analysis of the weak radiofrequency emitted by the protons of the water molecules during the relaxation. Because of the variable water content, different tissues can be distinguished within an MR image. In principle, the spatial resolution and the image sensitivity can be improved by increasing the external magnetic field, since the noise associated to the detected signal is directly proportional to it. However, for clinical applications the typical magnetic field values are limited to1.5 and 3 T.

Nuclei in the excited spin state can relax through two different processes named longitudinal and transversal relaxations. The longitudinal relaxation, with characteristic time T_1 and relaxation rate R_1 ($R_1=1/T_1$), is also known as spin-lattice relaxation and involves the recover from zero to the initial value of the longitudinal spin magnetization. On the other hand, the transversal relaxation with the characteristic time T_2 and relaxation rate R_2 ($R_2=1/T_2$), also known as spin-spin relaxation, is ascribed to the decay of the transverse magnetization from the excited state value to its starting value. In general, the relaxation rates associated to the two different relaxation processes are the rates for the magnetization to be recovered to its initial state through emission of a radiofrequency wave. When the T_1 is short, the longitudinal magnetization is rapidly recovered and, as a result, the tissue appears bright in T_1-weighted MR image. If the T_2 value is short, the corresponding tissue will appear dark in the T_2-weighted MR image because of the fast loss of transverse magnetization. The parameters T_2^* and R_2^* are also associated to the transverse magnetization decay if local magnetic field inhomogeneity affecting spin-spin relaxation are taken into account.[9]

The main limit of MRI is the low sensitivity. In particular, if the investigated tissue has not an appropriate proton density, its associated contrast within a MR image might not be sufficient the diagnostic purposes. With aim of overcoming this limitation and improving the effective application of MRI for clinical use, contrast agents were developed. A contrast agent is a substance affecting proton relaxation, so as to modify the tissue appearance within the MR-image. T_1-contrast agents (positive contrast agent) increase R_1 and produce a brightening in the MR image; T_2-contrast agents (negative contrast) shorten R_2, and produce a darkening in the MR image.

The efficiency of a substance as MRI contrast agent is quantified by the relaxivity coefficient r_i defined in equation 1.5.1, where i can be 1 or 2 according if the longitudinal or transversal relaxation is under investigation. R_i is the observed relaxation rate, T_{i0} is the characteristic relaxation time without the contrast agent and C is its concentration.

$$R_i = \frac{1}{T_{i0}} + r_i C \tag{1.5.1}$$

Even if a substance is proposed as T_1 or T_2 contrast agent, the ratio r_1/r_2 must be additionally evaluated since the spin-spin relaxation can decrease the signal associated to the longitudinal relaxation.
Typically, T_1-contrast agents are paramagnetic ions suitably included in an organic scaffold, which is needed to increase the both its biocompatibility and its stability *in vivo*. In principle, SPIONs can also be used as T_1 contrast agents, although the strong interaction between the spins of the water protons and local field of the nanoparticles prevents their use for the obtainment of T_1-weighted MR images. On the other hand, SPIONs present all the required properties for been T_2-contrast agents.[9]
Besides the exploitation of the intrinsic magnetic properties of SPIONs for MRI, suitable surface modifications can be used to prepare multimodal imaging contrast agents. Multimodal imaging involves the simultaneous collection of images resulting from different combined techniques.

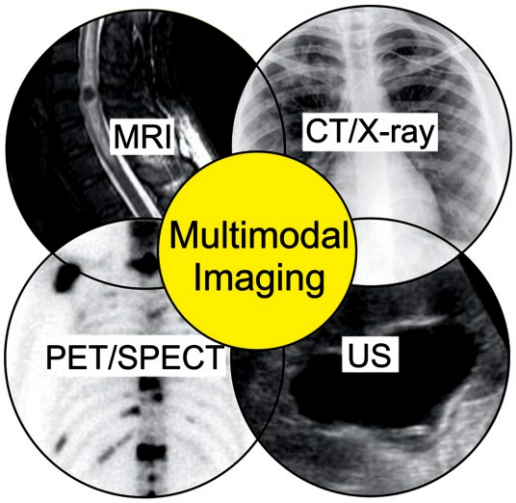

Figure 1.5.1: *Scheme of multimodal imaging approach.[20]*

Imaging techniques such as Computed Tomography (CT) or Positron Emission Tomography (PET) and Single-Photon Emission Computed Tomography (SPECT), require the preliminary injection of an active substance. This substance is responsible for the emission of the signal, which is subsequently detected and elaborated in the form of tissue images. In the case of PET, the active substance is a radionuclide, a radioactive isotopes responsible for positron emission. Typical radionuclides used for diagnostic applications are ^{68}Ga, ^{67}Ga, ^{64}Cu, ^{86}Y, ^{89}Zr, ^{44}Sc, ^{18}F and ^{124}I.[9, 54] For a suitable application of the radionuclides, they must be sequestered from aqueous solution using chelating ligands. This prevents toxic side-effects and hydrolysis processes that will affect the efficient delivery of the radionuclides in the target area. Ligands proposed for PET application are macrocyclic molecules, since they requires minimal physical manipulation during metal ion coordination. The rigid structure of a macrocyclic chelator exhibits a pre-organized binding site for the metal ion,

thereby decreasing the entropic loss upon its coordination.[54] Furthermore, bifunctional chelators can be conjugated to nanocarriers such as inorganic nanoparticles.

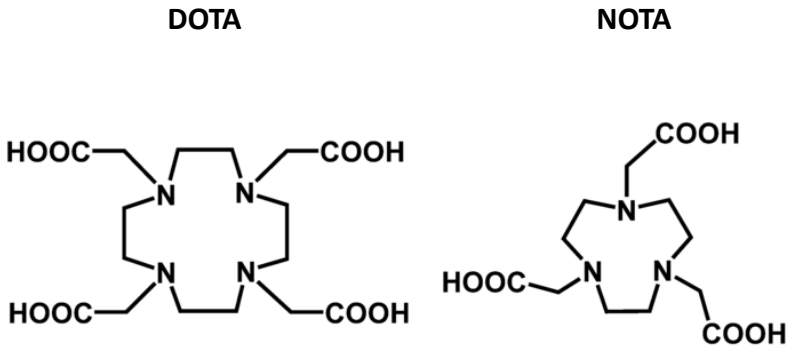

Figure 1.5.2: *Structure of DOTA and NOTA chelators.*

1, 4,7,10-tetraazacyclododecane-1,4,7,10-tetraacetic acid (DOTA) and (1,4,7-triazanonane-1,4,7-tryl)triacetic acid (NOTA) are reported as efficient chelators of ^{68}Ga.[55] Indeed, ^{68}Ga has a favorable positron emission (1880Kev) for PET imaging and a short half-life (68 min). Ga^{3+} being a hard metal ion (pK_a 2.6) with strong affinity for amines and oxygen donor group, and can be efficiently bounded by DOTA and NOTA in aqueous media. In both cases, the nitrogen atoms present in the macrocycles and the carboxylic groups participate to the gallium coordination. However, NOTA was reported as able to form more stable complexes with Ga(III) than DOTA with a fast coordination reaction carried out at room temperature and under mild conditions.[9]

Several examples of NOTA-based ligands for PET imaging are reported in the literature[56, 57], among which also conjugation with SPIONs was produced.[58-61] The great advantage of the NOTA-ligands for the functionalization SPIONs is the possibility to combine PET and MRI techniques. SPIONs functionalized with NOTA can be simultaneously detected through the two imaging techniques, and the resulting images will have complementary information. PET is characterized by high sensitivity and it is able to detect signals with radionuclide concentration down to the pico-molar level, but presents low spatial resolution. On the other hand, MRI is characterized by high spatial resolution but has a low sensitivity. The combined PET/MRI approach is becoming a very powerful technique for diagnostic applications.[9, 20] Consequently, the need of suitably designed nanoparticles that act simultaneously as MRI contrast agents and radionuclides carriers, is growing.

1.6 Interaction between functionalized SPIONs and biological relevant systems.

The safe application of nanotechnology devices in biomedicine requires fundamental understanding of their behavior in a living organism. The high surface energy, associated to every inorganic nanoparticle, produces the absorption of biomolecules when they come in contact with biological fluids. Among the biomolecules involved in this process, great attention has been payed to the formation of the protein corona.[62-64]

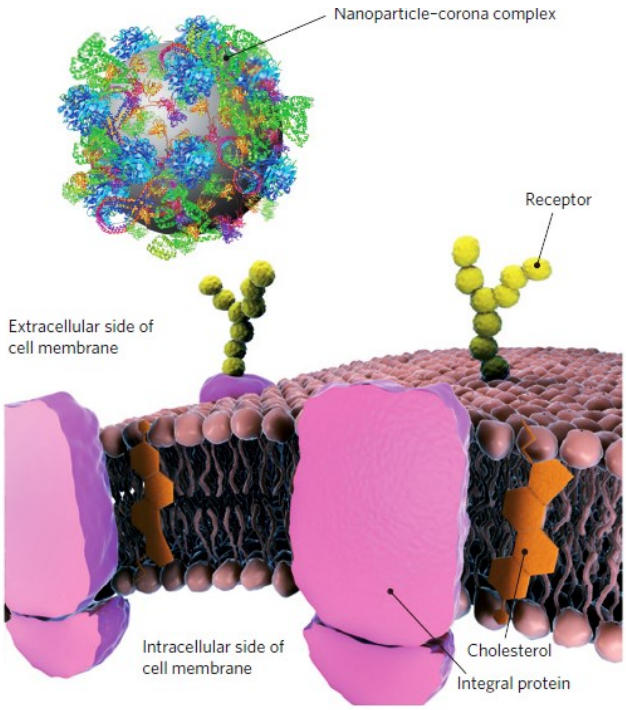

Figure 1.6.1: *The nanoparticle–corona complex in a biological environment. a, It is the nanoparticle–corona complex, rather than the bare nanoparticle, that interacts with biological machinery, here with a cell membrane receptor.[62]*

Several serum proteins were found to be able to cover the nanoparticle surface, leading to the formation of a corona around the nanoparticle, which is believed to be responsible for the interactions with a biological system. Even if large protein absorption were observed for the bare inorganic nanoparticles (without any coating layer or with a coating composed by small molecules, such as citrate ions), association of biomolecules still might occur even in the case of suitably functionalized nanoparticles.[62] The cellular membrane is another relevant biological component considered as a potential target for inorganic nanoparticles.[65]

During the last years, a large number of published reports was focused on the characterization of the interaction between nanoparticles and model cellular membranes with experimental and theoretical

approaches.[66-75] The plasma membrane participates in several cellular processes, first of all in controlling the trafficking of substances across the cells, which is fundamental for the cell life.[67, 76] Thus, when considering the exploitation of nanoparticle-based systems as platforms for drug delivery or diagnostic applications, the interaction of nanoparticles and the plasma membrane has a pivotal role in their *in vivo* activity.[77-80]

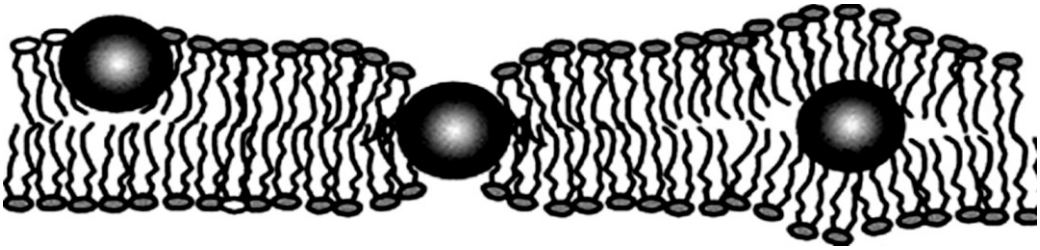

Figure 1.6.2: *Sketches of possible nanoparticle/bilayer interactions.[69]*

Different lipid bilayers were proposed as models for the cellular membrane.[81-84]Clearly the cellular plasma membrane is a very complex system, for which composition varies significantly from the different organisms. Usually, the mammalian plasma membrane is the one of interest. Even with this restriction, the diversity in the plasma membrane composition with respect to the organ tissues, is significant.[76] Moreover, the presence of a larger number of molecular components, such as phospholipids, sphingolipids, cholesterol and proteins, makes the plasma membrane quite difficult to mimic in detail. However, mimicking the plasma membrane lipid portion, which provides the barrier function, can be used to give key information on membrane interactions with potentially penetrating particles and molecules. In particular, the supported lipid bilayers are a common choice in the characterization of the interaction between membranes and extracellular systems.[85] They can be characterized through a large variety of techniques, such as electron and atomic force microscopy, X-ray and neutron reflectometry, ellipsometry and quartz crystal microbalance with dissipation monitoring (QCM-D); they have been largely exploited in the case of the interaction with potential drugs, peptides involved in target pathologies, and nanoparticles suitable for diagnostics and drug delivery.[78, 79, 82, 83]

The physical properties of the inorganic nanoparticles, such as the size, the surface charge or the hydrophobicity have emerged as the determining variables in the fate of the interaction between lipid bilayers and inorganic nanoparticles.[86] Indeed, several studies have been carried out using gold nanoparticles of different size and charge as model systems. In a few other cases, also the characterization of the interaction between lipid bilayers and metal oxide, metal sulfide, or metal selenides nanoparticles was pursued.[87-89]

Chapter 2 - *Preparation and Characterization of Functionalized SPIONs: Experimental Section*

SPIONs can be prepared through the thermal decomposition method, which ensures good size control during the growth of the nanoparticles. SPIONs are obtained with a hydrophobic coating, composed of oleic acid and oleylamine, which makes them stable in non-polar media. The synthesized SPIONs were subsequently functionalized with a recently developed functionalization strategy. Both functionalized and non-functionalized SPIONs were characterized combining scattering, microscopy and spectroscopy techniques. In this chapter, the adopted synthetic protocol is described together with as the functionalization strategy. The main features of the experimental set-up used to collect the physico-chemical characterization data are as well reported. The theoretical principles of the used techniques can be found in the appendices.

2.1 Synthesis of SPIONs through thermal-decomposition.

2.1.1 Materials.

Iron(III) acetylacetonate ($Fe(acac)_3$, 99%), 1,2-hexadecanediol ($C_{14}H_{29}CH(OH)CH_2(OH)$, 90%), oleylamine (OAM, $C_9H_{18}=C_9H_{17}NH_2$, 70%), oleic acid (OA, $C_9H_{18}=C_8H_{15}$-COOH, 99%), diphenyl ether ($C_{12}H_{10}O$, 99%), ethanol (C_2H_6O, ≥98%) and cyclohexane (C_6H_{12}, ≥99.9%) were purchased from Sigma Aldrich and used as received.

2.1.2 Synthetic protocol.

SPIONs were synthesized through a slightly modified version of the thermal-decomposition method introduced by *Sun et al[29, 30]*. 0.355 g of iron(III) acetylacetonate, 1.29 g of 1,2-hexadecanediol, 1.0 ml of oleylamine, 1.0 ml of oleic acid and 10 ml of diphenyl ether were mixed together in a three-neck flask (Figure 2.1.1, panel a). The solution was heated at 200 °C under argon atmosphere and vigorous stirring, and kept at this temperature for 2 h.

SPIONs are produced from the decomposition at high temperature (above 180°C) of the iron oxide precursor $Fe(acac)_3$. The decomposition of the iron salt is carried out in a high-boiling solvent, such

as diphenyl ether, and in the presence of 1,2-hexadecanediol. The diol acts as a reducing agent converting the iron(III) salts in the Fe_3O_4 oxide, which contains both Fe(II) and Fe (III). Oleic acid and oleyalmine are added as stabilizing agents to obtain SPIONs with a narrow size distribution. Indeed, both oleic acid and oleylamine molecules are able to bind SPION surface. By choosing the appropriate concentration of stabilizing agents, the growth of the SPIONs can be controlled and, at the same time, their aggregation is prevented.

At the end of the synthesis, the suspension was treated with ~ 10 ml of ethanol and centrifuged at 7000 rpm for 20 min in order to remove the undesired components. SPIONs, are produced as a solid precipitate, have been then redispersed in cyclohexane (Figure, 2.1.1. panel b).

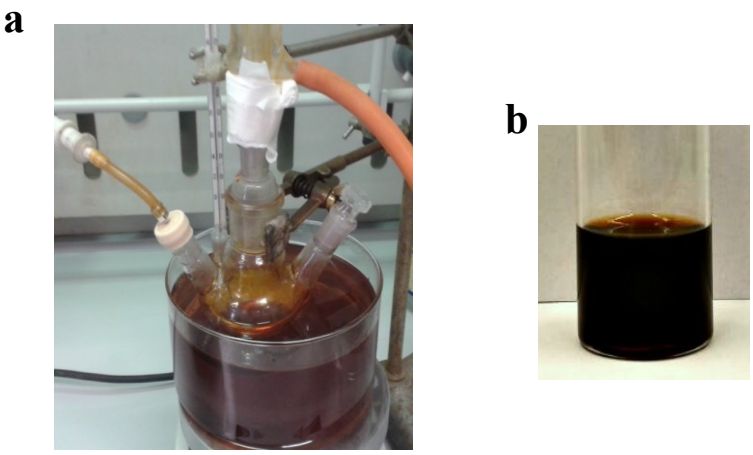

Figure 2.1.1: *Pictures of the used synthesis setup during SPIONs preparation (panel a) and of the obtained SPION cyclohexane suspension (panel b).*

The iron concentration in the synthesis product was evaluated through Inductively Coupled Plasma Mass Spectrometry (ICP-MS) analysis, performed by the research group of prof. Marco Trifuoggi (Dipartimento di Scienze Chimiche, Università degli Studi di Napoli "Federico II").

2.2 SPIONs functionalization.

2.2.1 Materials.

Cetyltrimethyl ammonium bromide (CTAB $CH_3(CH_2)_{15}N(Br)(CH_3)_3 \geq 99\%$) and deuterated water ($D_2O$ 99.9%D) were purchased from Sigma Aldrich.

1-stearoyl-2-hydroxy-3glicerno-sn-phosphocholine (18LPC $C_{26}H_{54}NO_7P$, >99%) and 1-palmitoyl-2-hydroxy-*sn*-glycero-3-phosphocholine (16LPC, $C_{24}H_{50}NO_7P$, >99%) were purchased from AvantiPolar Lipids Inc.

2.2.2 Functionalization protocol.

The thermal decomposition method leads to a stable suspension of SPIONs in non-polar solvents because of their coating of oleic acid and oleylamine. An appropriate functionalization procedure is mandatory for any application of SPIONs, which requires them as an equally stable suspension in water. In addition, a functionalization strategy that avoids further purification of the synthesis product should be preferred. Indeed each purification step eventually added to a protocol is responsible for losses of the synthesis product and reduces the yields of functionalized SPIONs. In order to satisfy all these queries, and above all to handle an extremely versatile functionalization strategy, the here described protocol was developed.

By exploiting the hydrophobic tails of oleic acid and oleylamine decorating the surface of the nanoparticles, a second layer of amphiphilic molecules was deposited on it (Figure 2.2.1). Functionalized SPIONs are composed by an inorganic core covered by two layers of organic molecules. The second layer is responsible for the stability in water media and can lodge, in principle, additional amphiphilic molecules with specific properties.

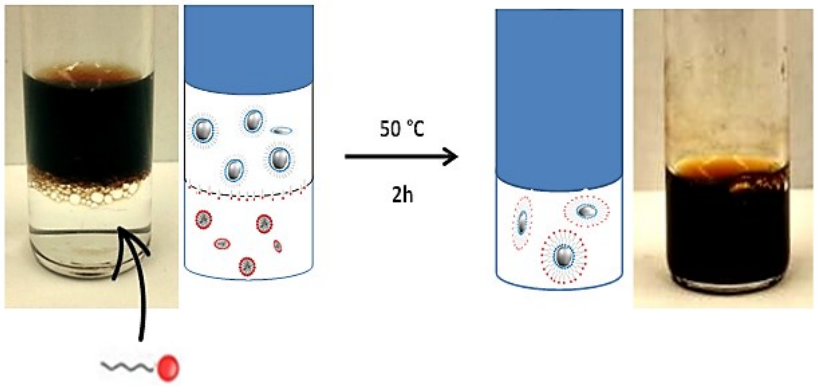

Figure 2.2.1**:** *Schematic representation of SPIONs functionalization through hydrophobic interaction.*

In details, the suspension in cyclohexane of SPIONs was stratified over the aqueous solution containing the desired amphiphilic molecules. The used concentration of surfactant was established in order to achieve the complete coverage of the surface of the SPIONs by the amphiphilic molecules, which corresponds to a SPIONs/surfactant molar ratio of 1:1000. The sonication of the biphasic system in a thermostat bath at 50 °C for about 2 h promoted the cyclohexane evaporation and the transfer into the aqueous phase of the SPIONs decorated with the additional layer of the amphiphilic molecules. In the present case, functionalized SPIONs were prepared using different amphiphilic molecules, as discussed in the following chapters. In particular, two zwitterionic

lysophosphatidylcholines, 16LPC and 18LPC, and the cationic surfactant CTAB, were used and the effect of the structure of the surfactants on SPION clustering was investigated (Chapter 3).
The functionalization protocol can be adapted to any molecule with amphiphilic structure, and it is suitable a large variety of SPION applications. Furthermore, it only requires that the surface of the nanoparticles nanoparticle to expose an apolar layer. Since several inorganic nanoparticle synthetic protocols include the use of long chain stabilizing agents, the proposed strategy can be adopted to functionalize nanoparticles constituted of different metals or metal oxides. Another relevant advantage is that the functionalization procedure is a one-step protocol, which does not require further purification.

2.3 Characterization of the magnetic properties of SPIONs.

The superparamagnetism of the iron oxide nanoparticles is the pivotal property for any the applications of SPIONs. Thus, the actual obtainment of effective SPIONs must be verified. Electron Paramagnetic Resonance (EPR) spectra and magnetization hysteresis loops recorded with a magnetometer were collected to investigate the magnetic properties of the synthesized iron oxide nanoparticles.
EPR spectra were recorded with a 9 GHz Bruker Elexys E-500 spectrometer (Bruker, Rheinstetten, Germany). Capillaries containing 200 μl of the sample were placed in a standard 4 mm quartz sample tube containing light silicone oil for thermal stability. The temperature of the sample was regulated at 25 °C and maintained constant during the measurement by blowing thermostated nitrogen gas through a quartz Dewar. The instrumental settings were as follows: sweep width, 6000 G; resolution, 1024 points; modulation frequency, 100 kHz; modulation amplitude, 1.0 G; time constant, 20.5 ms, incident power, 6.4 mW, Gain 60 dB. 64 scans were accumulated to improve the signal-to-noise ratio.
Magnetization hysteresis loops were recorded at Istituto Materiali per Elettronica e Magnetismo (IMEM) (Consiglio Nazionale delle Ricerche (CNR), Parma, Italy) with an Alternating Gradient Force Magnetometer (Model 2900, Princenton Measurements Corporation) and a SQUID magnetometer (Mod. XMPS-XL, Quantum Design). In particular, the temperature dependence of the magnetization was recorded using the procedure of Zero-field-cooling (ZFC) and Field Cooling (FC). The ZFC measurements were carried out by cooling the sample in zero magnetic field from room temperature to 10 K. Then a small magnetic field of 100 Oe was applied and the magnetization was measured while the temperature was raised up to room temperature. For the FC measurement the sample was cooled again to 10 K, this time under a magnetic field, and as for the ZFC measurement,

the magnetization data were collected as function of the temperature. All the magnetic moments were normalized to the magnetization *per* dried sample mass.

2.4 Structural characterization of SPIONs.

Both functionalized and non-functionalized SPIONs (the synthesis product) were characterized combing different scattering techniques. Wide Angle X-ray Scattering (WAXS) diffraction pattern was recorded to identify the iron oxide core composition. Dynamic Light Scattering (DLS), Small Angle Neutron Scattering (SANS) and Small Angle X-ray Scattering (SAXS) experiments were performed to define the shape, the size and the size distribution of SPIONs.

WAXS diffraction profiles were collected in collaboration with prof. Odda Ruiz De Ballesteros (Dipartimento di Scienze Chimiche, Università degli Studi di Napoli "Federico II") WAXS spectrum was collected with Ni-filtered Cu Kα radiation (λ = 1.5418 Å) by using an automatic Philips diffractometer. The profiles were recorded performing a step scan of the diffraction angle 2θ in the range 20 - 70° with a step size of 2θ equal to 0.1 ° and a time per step of 14.3 s. The Pulse Height Detector (PHD) level values were set to 35 and 80% for the lower and upper level, respectively, to reduce the background intensity due to the fluorescence of the samples. From the analysis of the peaks exhibited by the collected diffraction pattern, the actual preparation of SPIONs was verified by means of their crystalline structure.

DLS measurements were performed with a home-made instrument composed by a Photocor compact goniometer, a SMD 6000 Laser Quantum 50 mW light source operating at 532.5 nm, a photomultiplier (PMT-120-OP/B) and a correlator (Flex02-01D) from *Correlator.com*. All measurements were performed at (25.00 ± 0.05) °C with the temperature controlled by means of a thermostat bath. The diffusion coefficient (*D*) was performed using a variation of CONTIN algorithm incorporated in Precision Deconvolve software [90]. For spheres diffusing in a continuum medium at infinite dilution, in the approximation of spherical objects, the diffusion coefficient is related to the hydrodynamic radius, through the Stokes–Einstein equation (see Appendix C). The hydrodynamic radius (R_h) was calculated with the appropriate viscosity value: for the suspension in cyclohexane or water of SPIONs the used viscosity was respectively 1.02 and 0.89 cP.

The diffusion coefficient indicated in the Tables of the following chapters is averaged over at least three independent measurements performed with scattering angle corresponding to 90°. This value of D is used to calculate the hydrodynamic radius (R_h) of the scattering particles by applying the Stokes-Einstein equation. In the case of the suspension of SPIONs in cyclohexane, DLS measurements were carried out in the range of the scattering angle of 120°-60°. As reported in Appendix C the plot of Γ

vs. q^2, where $\Gamma = D \cdot q^2$, with the scattering vector q, is indicative of the monodispersity of the investigated suspension (see Appendix C).

SANS measurements were carried out in two different European facilities located in Germany and UK. In order to perform SANS measurements, functionalized SPION suspension in D_2O were prepared. D_2O was used to obtain a sufficiently high contrast between the scattering rising from the nanoparticles and the solvent (see Appendix A).

SANS experiments were performed at 25 °C with the Loq instrument located at ISIS Science and Technology Facilities Council, in Chilton (UK). The instrument is characterized by a fixed two-dimensional detector positioned at 4 metres from the sample, which can detect the positions and times of arrival of the scattered neutrons. This configuration allowed collecting data in a range of the modulus of the scattering vector $q = 4\pi/\lambda \sin(\theta/2)$ between 0.008 $Å^{-1}$ and 0.221 $Å^{-1}$, with θ being the scattering angle. The investigated systems were contained in a closed quartz cell, in order to prevent the solvent evaporation. The raw data were then corrected for the background (*bkg*) and empty cell scattering.

SANS measurements were also carried out at 25 °C with the KWS2 diffractometer operated by Julich Centre for Neutron Science at the FRMII source located at the Heinz Meier Leibtnitz Centre, Garching (Germany). Neutrons with a wavelength of 5 Å and $\Delta\lambda/\lambda \leq 0.2$ were used. A two-dimensional array detector at three different wavelength (W)/collimation (C)/sample-to-detector(D) distance combinations ($W_{5Å}C_{8m}D_{2m}$, $W_{5Å}C_{8m}D_{8m}$ and $W_{5Å}C_{20m}D_{20m}$), measured neutrons scattered from the samples. These configurations allowed collecting data in a range of the modulus of the scattering vector q between 0.002 $Å^{-1}$ and 0.3 $Å^{-1}$.

SAXS experiments at 25 °C were performed at the beam line I22 of Diamond Light Source located at the Rutherford Appleton Laboratories in Chilton, UK. The instrumentation associated with this beam line ensures high flux and brilliance, as well as high resolution and minimum beam divergence. The beam line operated at energy corresponding to 12.8 keV and a wavelength of 1 Å, while the detector was positioned at a distance of 6 m from the sample. This configuration allowed collecting data in the q range corresponding to 0.007-0.240 $Å^{-1}$, which resulted to be appropriate in order to have information on the structure of SPIONs. The raw data were then corrected for the background. The correction for the detector, the radial average and the transformation to absolute scattering cross sections $d\Sigma/d\Omega$ were made by using collagen as standard.

Both SANS and SAXS data analysis was performed using SasView software available on the web (*http://www.sasview.org/*). SasView is an opensource software developed by an international collaboration of European facilities for the analysis of small angle scattering data.

The software offers a large selection of model functions for the interpretation of Small Angle Scattering (SAS) data. As discussed in Appendix A, the measured intensity is proportional to the product of the form factor (*P(q)*) and the Structure factor (*S(q)*). The appropriate expression of P(q) and S(q) can be selected from the library contained within the software. In addition, for polydispersed systems, different size distribution can be used to weight both the form factor and the structure factor. In the case of the analyzed samples, the concentration of nanoparticles was sufficiently low for the structure factor to be negligible. A Schulz distribution of the structural parameters of the SPIONs, such as their radius, was used during the fitting of the collected experimental data. For a general variable x the Schulz distribution[91] is given by

$$f(x) = \frac{1}{Norm}(z+1)^{(z+1)}\left(\frac{x}{x_{mean}}\right)\frac{\exp\left[-(z+1)\frac{x}{x_{mean}}\right]}{x_{mean}\Gamma(z+1)} \tag{2.4.1}$$

where x_{mean} is the mean, *Norm* is a normalization factor, determined during the numerical calculation, and z is the width of the distribution., z is related to the polydispersity p by equation 2.4.2.

$$z = \frac{(1-p^2)}{p^2} \tag{2.4.2}$$

The polydispersity is defined in equation 2.4.3, where σ is the standard deviation.

$$p = \frac{\sigma}{x_{mean}} \tag{2.4.3}$$

Basic principle of the scattering theory applied to light, neutron and X-ray scattering can be found in Appendix A and C.

Transmission Electron Microscopy (TEM) and cryogenic Transmission Electron Microscopy (cryo-TEM) images were also collected to further characterize the structure of SPIONs. In particular, cryo-TEM measurements were performed at the Heinz Meier Leibnitz Source, Garching Forschungszentrum facility. A Multi A 300 mesh cupper grid coated with holey carbon film (Quantifoil Micro Tools GmbH) was dipped into the samples and then placed in the chamber of a cryo-plunge (EMGP Leica GmbH) maintained at 25 °C and 80% relative humidity. The excess liquid was removed by blotting with filter paper. The sample was cryo-fixed by rapid immersion into liquid ethane between -170 and -180 °C in the cryo-plunge. The specimen was inserted into a cryo-transfer holder (HTTC 914, Gatan, Munich, Germany) and transferred to a JEM 2200 FS EFTEM instrument (JEOL, Tokyo, Japan). Examinations were carried out at temperatures around -180°C.

The transmission electron microscope was operated at an acceleration voltage of 200 kV. Zero-loss filtered images were taken under reduced dose conditions (<21 000 e-/nm2). All images were recorded digitally by a bottom-mounted 16 bit CCD camera system (FastScan F214, TVIPS, Munich, Germany).

2.5. Interaction between functionalized SPIONs and lipid bilayer.

2.5.1 Materials.

1-palmitoyl-2-oleoyl-*sn*-glycero-3-phosphocholine (POPC, $C_{42}H_{82}NO_8P$, >99%), 1-palmitoyl-2-oleoyl-*sn*-glycero-3-phospho-(1'-*rac*-glycerol) (POPG, $C_{40}H_{76}O_{10}P$ >99%) were purchased from AvantiPolar Lipids Inc. Cholesterol (CHOL, $C_{27}H_{46}O$, ≥99%) and deuterated water (D_2O 99.9%D) were purchased from Sigma Aldrich

2.5.1 Characterization Techniques.

Neutron Reflectometry (NR) and Quartz Crystal Microbalance with Dissipation monitoring (QCM-D) techniques were combined to characterize lipid bilayers that mimic the lipid portion of the plasma cellular membrane and their interaction with the functionalized SPIONs.

Neutron reflectivity measurements were performed at 25°C on the D17[92] and the SuperADAM [93, 94] reflectometers at the Institut Laue Langevin (ILL, Grenoble). The D17 reflectometer operates in the time of flight mode and the data were collected using neutrons with wavelengths, λ, in the range of 2-20 Å at two incoming angles typically of 0.8° and 3.2°. The resulted *q*-range covered was of $8 \cdot 10^{-3}$ Å^{-1} < *q* < 0.2 Å^{-1}.

The SuperADAM reflectometer was used in the monochromatic mode at the fixed wavelength of 5.183 Å and the q-range of 0 Å^{-1} < q < 0.2 Å^{-1} was explored. The raw data was treated with the SuperADAM Sared program. Data were converted in an absolute-reflectivity scale by normalizing to the direct beam at the same slit setting and then dividing by the monitor counts. In this way, the fluctuations in the neutron flux were taken into account and the data were corrected for points measured for different lengths of time. Slits were chosen to vary with the incident angle in such a way as to provide a constant illumination of the sample. Since SuperADAM, similarly to D17, is equipped with a position sensitive detector, on both instruments the background was measured simultaneously and was accounted for by using the average value from the regions of interest on both

sides of the specularly reflected beam. Measurements were performed in different aqueous contrasts to increase the resolution in data analysis and the reliability of the model used to describe the data.

The solid-liquid flow cells were attached to an HPCL pump to flush the solvents through the cells for solvent exchange. The pump was set at a 2 ml/min speed and connected via switch to D_2O and H_2O reservoirs for the injection of pure D_2O, Silicon Matched Water (SMW), a 32% D_2O-68% H_2O mixture, and pure H_2O.

Before the introduction of the sample in the NR cell, the silicon blocks were characterized in terms of their native silicon oxide layer and of their surface roughness in three solvent contrast D_2O, H_2O and SMW.[95] NR data were collected on lipid bilayers with different composition: POPC/POPG (90/10 w/w), POPC/POPG/CHOL (70/10/20 w/w/w) and POPC/POPG/CHOL (60/10/30 w/w/w). Data collection was performed using the three different contrasts (D_2O, H_2O and SMW) and repeated upon functionalized SPIONs injection.

The analysis of the reflectivity curves was performed using the AuroreNR software[96]. The software is based on the use of the Parratt formalism [97], thus the reflectivity curves were treated as arising from a stack of parallel layers with a different scattering length density and a different thickness depending on the composition. The interface roughness was also taken into account in the models and it was represented by an error function. In order to have unambiguous interpretation of the sample structure reflectivity curves collected in three different contrasts (D_2O, SMW and H_2O) were simultaneously fitted (global analysis).

The results obtained from NR characterization of the lipid bilayers in the presence and in the absence of the functionalized SPIONs were validated by performing also Quartz Crystal Microbalance with Dissipation Monitoring (QCM-D) experiments. QCM-D data were collected with Q-sense E4 instrument (Q-sense, Gothenburg, SE) available at the Partnership for Soft Condensed Matter (PSCM) laboratory at the Institut Laue Langevin (ILL) in Grenoble. The instrument is equipped with four flow liquid cells of 0.5 ml internal volume. A coated quartz sensor, with active surface of ~1 cm^2, SiO_2 layer of ~ 100 nm and with fundamental resonance frequency 4.95MHz, is mounted horizontally in each cell. The quartz supports were properly cleaned through bath sonication in ethanol and water (15 min each) and subsequently through UV-ozone cleaning before collection of the measurements.

During the experiments, real time variations of support oscillating frequency (ΔF_n) with respect to the calibration value are measured for different overtones indicated as F_n, with n representing the overtone number (n= 3, 5, 7, 9, 11, 13), and the corresponding dissipation coefficients (D) were evaluated for all the overtones. [98]

It has been reported that for a rigid film evenly distributed on the sensor surface and with a thickness much smaller than that of the sensor, the recorded frequency shifts, normalized for the overtone number, can be simply related to the adsorbed mass (Δm) through the Sauerbrey equation:

$$\frac{\Delta f_n}{n} = -\frac{1}{C}\Delta m \qquad (2.5.1)$$

where C is the mass sensitivity constant corresponding to 17.7ng·cm^2·Hz^{-1} for the sensors used in this experiment:[99] The experiments were performed at 25 °C with the cells connected to a peristaltic pump (flow rate 0.2 ml/min). As in the case of NR measurements, data collected on the supported lipid bilayers were compared with the one obtained after functionalized SPIONs injection.

.

Chapter 3 - *Physico-chemical Characterization of SPIONs*

The thermal decomposition method represents a solid protocol for the synthesis of SPIONs with narrow size distribution. Nevertheless, a detailed investigation of the composition and the structure of the synthesized SPIONs was carried out in order to verify the effective obtainment of iron oxide nanoparticles with the desired properties. In particular, WAXS diffraction patter, EPR spectrum and magnetization hysteresis loops were collected to identify the synthesis product as indeed composed of superparamagnetic Fe_3O_4 nanoparticles. DLS, SAXS and TEM were combined to characterize the size, the shape and the size distribution of the synthesized SPIONs.
scattering experiments were performed aiming at defining SPION shape, size and size distribution. On the other hand, synthesized SPIONs, were also characterized in terms of their composition and magnetic properties, thus demonstrating the effective obtainment of superparamagnetic Fe_3O_4 iron oxide nanoparticles.

3.1 Composition and magnetic properties of non-functionalized SPIONs.

As discussed in Chapter 1, ferromagnetic or ferrimagnetic nanoparticles below a certain critical size (which is about 20 nm for iron oxide Fe_3O_4) are structured as a single domain structure; hence a single giant magnetic moment, composed of all the individual atomic magnetic moments, can be associated to each nanoparticle.[6] Above the blocking temperature, if no external magnetic field is applied the net magnetic moment associated to all the nanoparticles is zero. If an external field is applied, the nanoparticles behave like a paramagnetic material aligning their magnetic moments along the direction of the external field. In contrast to a classical paramagnetic material, the ferromagnetic or ferrimagnetic single-domain nanoparticles exhibit a much larger susceptibility and are named superparamagnetic nanoparticles.[7]
The application of SPIONs as MRI contrast agents relies on their ability to affect the relaxation of the water protons when an external magnetic field is applied. Contrast agents shorten the transversal relaxation time T_2 and consequently produce a darkening in the MR image. One can see that the superparamagnetic property of the iron oxide nanoparticles is crucial for their application as MRI contrast agents.

Among the iron oxides, magnetite exhibit best performances in SPIONs. [22] Thus, WAXS diffraction pattern was collected for the synthesized nanoparticles in order to verify the obtainment of the nanoparticles composed by the appropriate iron oxide.

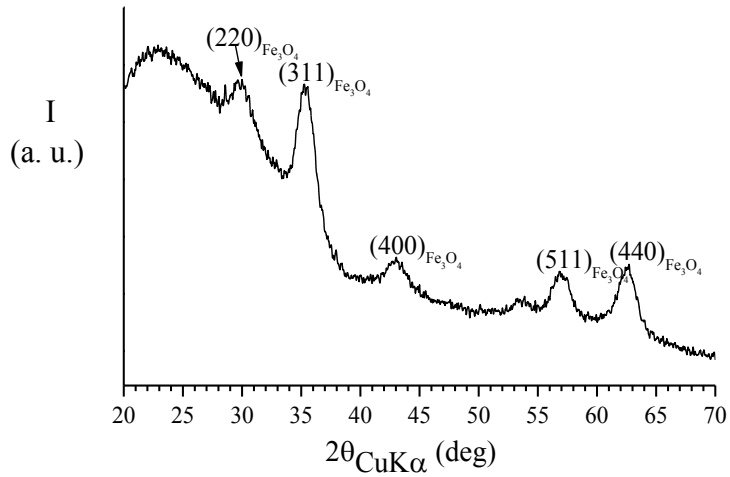

Figure 3.1.1: *WAXS profile collected for synthesized SPIONs dried on a quartz support. The Miller indices of Fe_3O_4 are indicated in the graph.*

The diffraction profile of the dried nanoparticles showed strong peak at 2θ = 35.4° and less intense peaks at 2θ = 30, 43.1, 57 and 62.6° (Figure 3.1.1). The observed peaks were identified as corresponding to the 311, 220, 400, 511 and 440 reflections, respectively, of the crystalline structure of Fe_3O_4 iron oxide.[100] Thus, the collected WAXS spectrum suggested that the synthesized nanoparticles indeed exhibited the crystalline structure typical of Fe_3O_4.

Table 3.1.1: *Diffraction angles (2θ), Bragg distances (d), relative intensities (I) and Miller indices (hkl) of the diffraction peaks observed in the diffraction profile of Figure 3.2.1.*

Non-functionalized SPIONs			
$2\theta_{CuK\alpha}$ (deg)	***d (Å)***	***I***	***hkl***
30.0	2.97	30	220
35.4	2.53	100	311
43.1	2.10	20	400
57.0	1.62	30	511
62.6	1.84	40	440

The characterization of the synthesized SPIONs involved also the investigation of their magnetic properties. EPR is a sensitive technique suitable for the characterization of paramagnetic materials, such as those containing free radicals. Furthermore, as reported in the literature, SPIONs are characterized by a strong EPR signal for applied magnetic field value in the range of 2500-4500 G.[101]

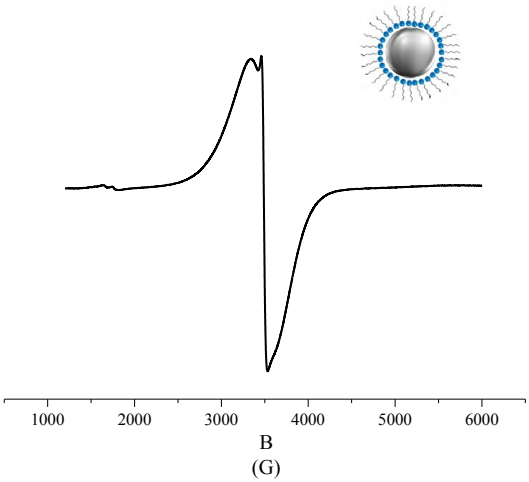

Figure 3.1.2: *EPR spectra for SPION suspension with Fe concentration 0.02 mg/ml.*

In order to collect the EPR spectrum an appropriate volume of the diluted SPION suspension in cyclohexane was sealed into a capillary. Dilution of the initially obtained suspension was necessary to attenuate the strong nanoparticle signal. As reported in Figure 3.1.2, the recorded EPR spectrum is characterized by the expected broad signal centered at 3500 G, which is typical of superparamagnetic Fe_3O_4 nanoparticles.[101]

The magnetic properties of the synthesized SPIONs were further investigated by recording the M *vs* H hysteresis loop at room temperature and by measuring the blocking temperature of the SPIONs with a SQUID magnetometer, in collaboration with Dr. César de Julián Fernández (Istituto dei Materiali per l'Elettronica ed il Magnetismo (IMEM), Consiglio Nazionale delle Ricerche (CNR), Parma, Italy). The room-temperature hysteresis curve (Figure 3.1.3, panel a) instead of a loop exhibited the S-shape typical of superparamagnetic nanoparticles with a magnetization saturation (M_s) value of 15 emu/g. As mentioned in Chapter 2, the magnetization saturation was calculated normalizing the experimental result by the dried mass of the analysed sample.

Since M_s of bulk magnetite is 80 emu/g, the obtained value in case of the SPIONs suggested the presence of about 17% w/w of magnetite in the sample. The remaining 83% w/w of the sample is composed by non-magnetic material i.e. organic molecules present on the SPION surface. Roughly the same result was obtained from calculating the percentage of iron oxide in the solid material from

the iron concentration of 3.4 mg/ml, analysed by means of ICP-MS. This calculation indicated that all the iron oxide contained in the cyclohexane suspension was in the form of magnetite Fe_3O_4. The temperature dependence of the magnetization was measured, using the ZFC - FC methodology (Figure 3.2.3, panel b), to investigate superparamagnetic behaviour of the SPIONs. The transition from low-temperature blocking behaviour to high temperature superparamagnetic behaviour[102] occurs in a narrow temperature range with the average blocking temperature (T_B) of 30 K, corresponding to the maximum of the ZFC magnetization.

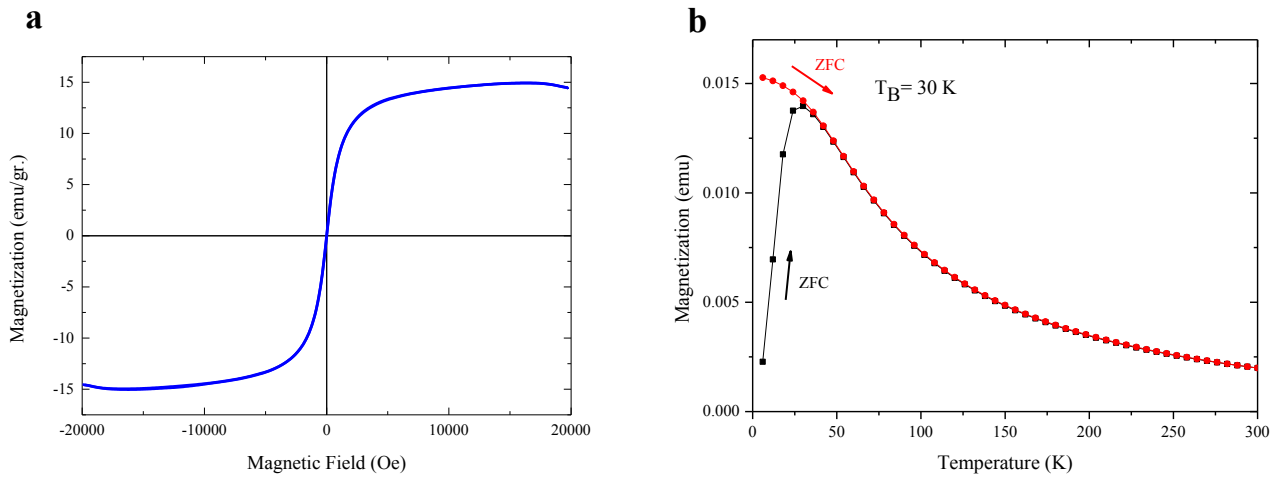

Figure 3.1.3: *Hysteresis loops for dried SPIONs (panel a) and evaluation of the blocking temperature using ZFC-FC methodology (panel b).*

Altogether, the characterization confirmed that the synthesized product according to the protocol reported in Chapter 2 was indeed composed of SPIONs.

3.2 Structural characterization of the synthesized SPIONs.

The synthesized SPIONs were coated by an oleic acid and oleylamine layer, which makes them stable in apolar solvents, such as cyclohexane. The hydrodynamic radius of the SPIONs in the cyclohexane suspension was evaluated by means of DLS measurements, as discussed in Chapter 2.

Reported in Figure 3.2.1, panel a, is the hydrodynamic radius distribution corresponding to one of the performed DLS measurements at scattering angle 90°. A single and narrow distribution of nanoparticles was observed. The monodispersity of the system was further validated by collecting data at different scattering angles. In particular, as discussed in Appendix C, a modispersed suspension of scattering particles is characterized by a linear dependence of Γ on q^2, with $\Gamma = D \cdot q^2$.

D is the diffusion coefficient of the scattering particles and *q* is the scattering vector. The mean diffusion coefficient reported in Table 3.2.1 was evaluated from the slope of the Γ vs q^2 plot.

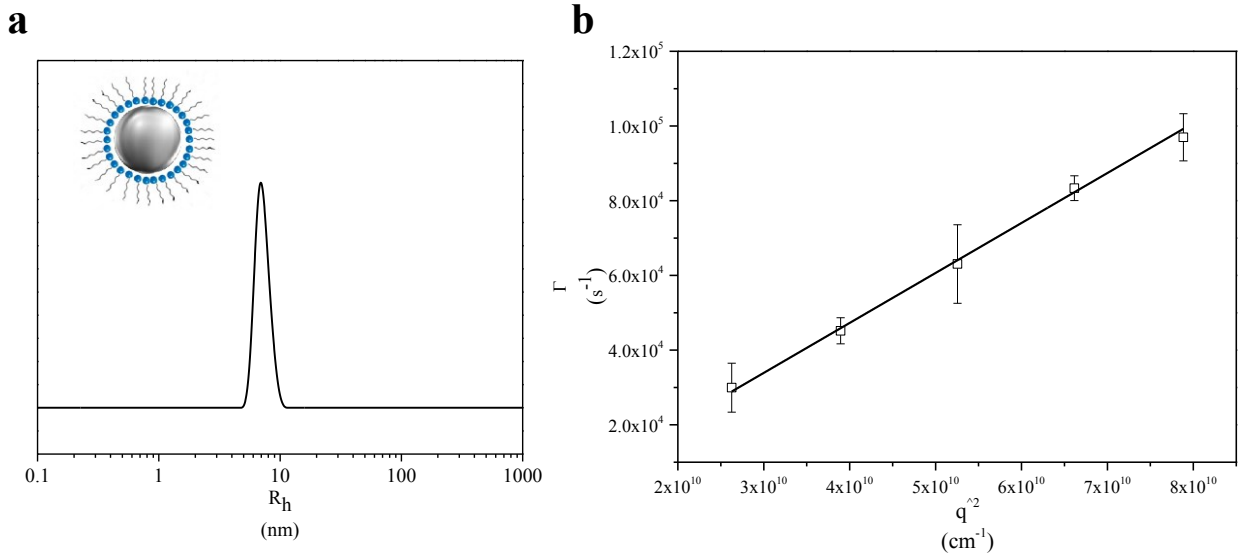

Figure 3.2.1: *Hydrodynamic radius distribution obtained from DLS measurements at scattering angle corresponding to 90° (panel a) and Γ vs q^2 data together with the corresponding linear fit.*

The hydrodynamic radius (R_h) of the synthesized SPIONs was calculated from the Stokes-Einstein equation (equation C.13), and is about 6 nm. The estimated R_h takes into account the oleic acid and oleylamine shell, coating the iron oxide core, as well as the solvation shells, which are diffusing with the SPIONs. Thus, the adopted synthetic protocol led to the actual obtainment of monodispersed nanoparticles.

In order to complete the information derived from DLS measurements, and to further characterize the SPION size and shape, Small Angle X-rays Scattering (SAXS) data were collected.

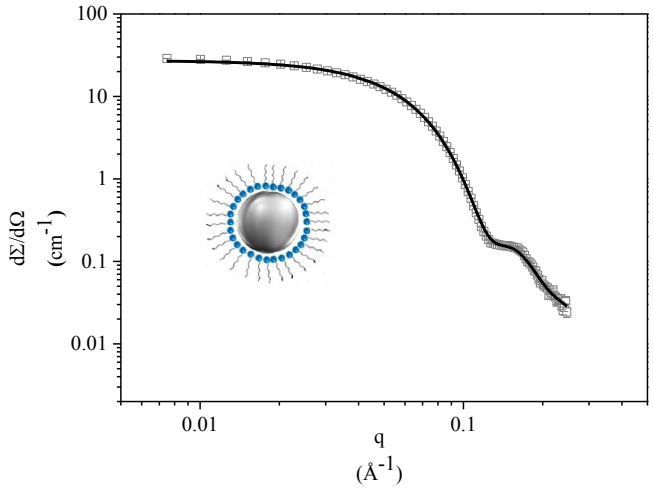

Figure 3.2.2: *SAXS experimental data together with the corresponding fitting curve for SPION suspension in cyclohexane*

The scattered intensity that is recorded during a small angle scattering experiment depends on the difference between the scattering density (ρ) of the particles and the one of solvent (Appendix A).
The X-ray scattering length densities of the different components that were present within the sample are: $\rho_{Fe_3O_4}^{X-ray} = 4.1 \cdot 10^{-5}\text{Å}^{-2}$, $\rho_{oleic\ acid}^{X-ray} = 8.5 \cdot 10^{-6}\text{Å}^{-2}$, $\rho_{oleylamine}^{X-ray} = 7.8 \cdot 10^{-6}\text{Å}^{-2}$ and $\rho_{cyclohexane}^{X-ray} = 7.5 \cdot 10^{-6}\text{Å}^{-2}$. Since the scattering length density of the oleic acid and oleylamine layer is very close to the scattering length density of the solvent (cyclohexane), X-rays are a suitable tool to probe only the inorganic core of the SPIONs.
As mentioned in Chapter 2, the scattered intensity is proportional to the form factor *P(q)*. In the present case, the spherical form factor (reported in equation 3.2.1) was used, where r_{core} and ρ_{core} are the radius and the scattering length density of the inorganic core of the SPIONs. In addition, a Schulz distribution (equation 2.4.1) of r_{core} was included in the model to evaluate the polydispersity of the SPION inorganic core.

$$P(q) = \frac{1}{V^2}\left[3V_C \left(\rho_{Fe_3O_4} - \rho_{cyclohexane} \right) \frac{\left(sin\left(qr_{\text{core}}\right) - qr\, cos\left(qr_{\text{core}}\right)\right)}{\left(qr_{\text{core}}\right)^3} \right]^2 \qquad (3.2.1)$$

As shown in Figure 3.2.2, a very good agreement was achieved between the fitting curve and the experimental data. SAXS data led to the characterization of the inorganic core of the synthesized SPIONs as presenting a spherical shape and a radius of about 3 nm (Table 3.2.1).

Table 3.2.1: *Structural parameters obtained from DLS and SAXS data analysis collected for non-functionalized SPIONs suspension in cyclohexane.*

Synthesized SPIONs			
D·10^6 (cm^{2}s^{-1})	**R_h (nm)**	**r_{core} (nm)**	**p_{core}**
1.34 ± 0.04	6 ± 1	3.3 ± 0.4	0.19 ± 0.01

The correct interpretation of the scattering data was verified by recording TEM images. In particular, a proper amount of the SPION cyclohexane suspension was dried onto a copper grid and subsequently examined with the microscope. Inspection of the image in Figure 3.2.3 confirms that the SPION can indeed be geometrically considered as a sphere with size comparable to the value estimated from the other experimental techniques.

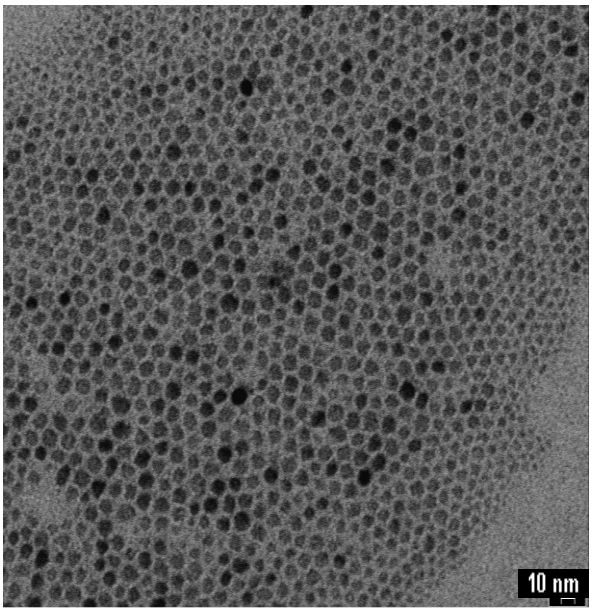

Figure 3.2.3: *TEM image of SPIONs cyclohexane suspension dried on a copper grid.*

Chapter 4 - *Characterization of Functionalized SPIONs: the Effect of the Surfactant*

Stable aqueous suspensions of SPIONs were obtained by adopting the functionalization strategy presented in Chapter 2. In particular, different surfactants were initially tested in order to identify the best conditions for the production of stable functionalized SPIONs. The developed functionalization procedure, being based on the hydrophobic interaction between two layers of amphiphilic molecules, is affected by the aggregation properties of the molecules chosen for the functionalization step. On the other hand, it is well known that the structure of the hydrophobic and hydrophilic portions of an amphiphilic molecule determines its behavior toward aggregation. Thus, we chose three surfactants differing for the hydrophobic and hydrophilic regions and prepared three suspensions of functionalized SPIONs. These suspensions were characterized through DLS and SANS measurements and the effect of the surfactant structure on the SPION coating efficiency was evaluated.

4.1 Surfactant-functionalized SPIONs.

Suitably functionalized SPIONs have been proposed as effective MRI contrast agents and potential nanocarries for targeted drug delivery and multimodal imaging. These applications require functionalized SPIONs to be stable in water media and exhibit a high level of biocompatibility. In order to introduce novel functionalized SPIONs, competitive with the ones already presented in the literature, we exploited the hydrophobic interaction to decorate the oleic acid and oleylamine layer with a second amphiphilic layer composed by lysophosphatidylcholine molecules. Recent studies pointed at the SPIONs functionalized with zwitterionic surfactant as valid alternative for their long-circulation time and stability in biological media with respect to the PEG-functionalized SPIONs already approved by FDA. [19]

SPIONs were functionalized with mono-tailed lysophosphatidylcholines, since their structure can be easily interdigitated among the hydrophobic tails of the inner oleic acid and oleylamine layer. 18LPC and 16LPC lysophosphatidylcholines were used to relate the length of the hydrophobic portion to the effectiveness of SPION coating. However, as already mentioned, the aggregation behavior of an

amphiphilic molecule depends on the structure of both the hydrophobic tail and the hydrophilic head. To test the effect of the polar head structure also the cationic surfactant CTAB was used to prepare functionalized SPIONs. CTAB molecule exhibits the same acyl chain as 16LPC, but present a positively charged hydrophilic head (Figure 4.1.1).

By comparing the structural characterization carried out on the SPIONs functionalized with the three different surfactants, the clustering tendency was systematically studied as a function of the hydrophobic and hydrophilic surfactant structure. Indeed, if the surfactant used during SPION functionalization does not efficiently cover SPION surface, the nanoparticles tend to aggregate within the suspension thus minimizing their surface energy.

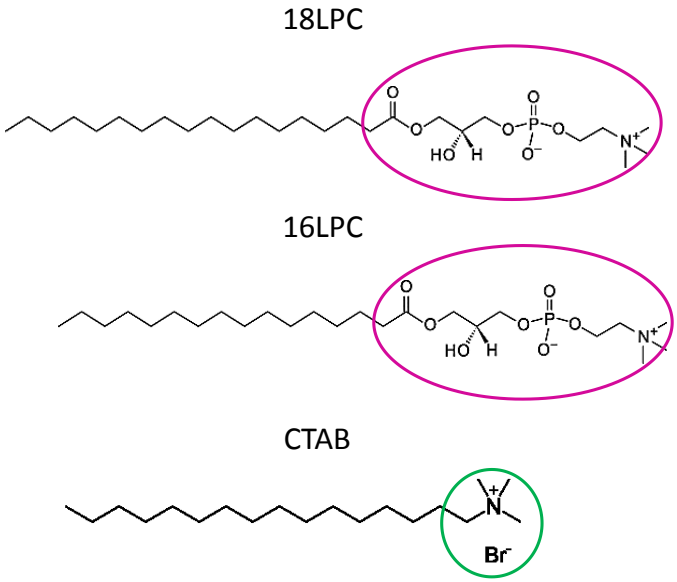

Figure 4.1.1: *Schematic representation of 18LPC, 16LPC and CTAB structures. The polar regions of the molecules are highlighted.*

According to our recently proposed protocol (Chapter 2), 18LPC, 16LPC, and CTAB were dissolved in D_2O and three surfactant solutions were prepared at $4 \cdot 10^{-3}$ m concentration. D_2O solutions were needed for SANS experiments (see Appendix A), however the same samples were also analyzed by means of DLS measurements. 1 ml of SPIONs suspension in cyclohexane with iron concentration 2 mg/ml, was stratified on the surfactant solution in order to prepare functionalized SPIONs. This procedure leads directly to the obtainment of 18LPC-functionalized SPIONs, 16LPC-functionalized SPIONs and CTAB-functionalized SPIONs, named hereafter respectively as 18LPC/SPIONs, 16LPC/SPIONs and CTAB/SPIONs.

4.2 Characterization of SPIONs functionalized with lysophosphatidylcholines.

Functionalized SPIONs are composed of an inorganic inner core and an organic outer shell. Thus, in order to characterize their structure, it is crucial to choose a technique sensitive to the different components. For this purpose, neutrons represent the perfect probe, since both the iron oxide core and the organic shell can be detected, and, in particular, the organic molecules coating the SPIONs exhibit a good contrast on the background of the solvent.

In Figure 4.2.1 (panel a) SANS experimental data collected for the 18LPC/SPION suspension are reported together with a fitting curve. The suspension was considered as a polydispersed distribution of spherical particles exhibiting core-shell structure. As discussed in Chapter 3 for the SAXS data analysis, the scattered intensity was considered as proportional to a form factor that in the present case is reported in equation 4.2.1. This core-shell form factor ($P_{core\text{-}shell}(q)$) was weighted by a Schulz distribution of the radius of the inorganic core (r_{core}) and the organic shell thickness (r_{shell}) of the SPIONs. In this way, the polydispersity on both r_{core} and r_{shell} was evaluated (they are indicated in Table 4.2.1 as p_{core} and p_{shell})

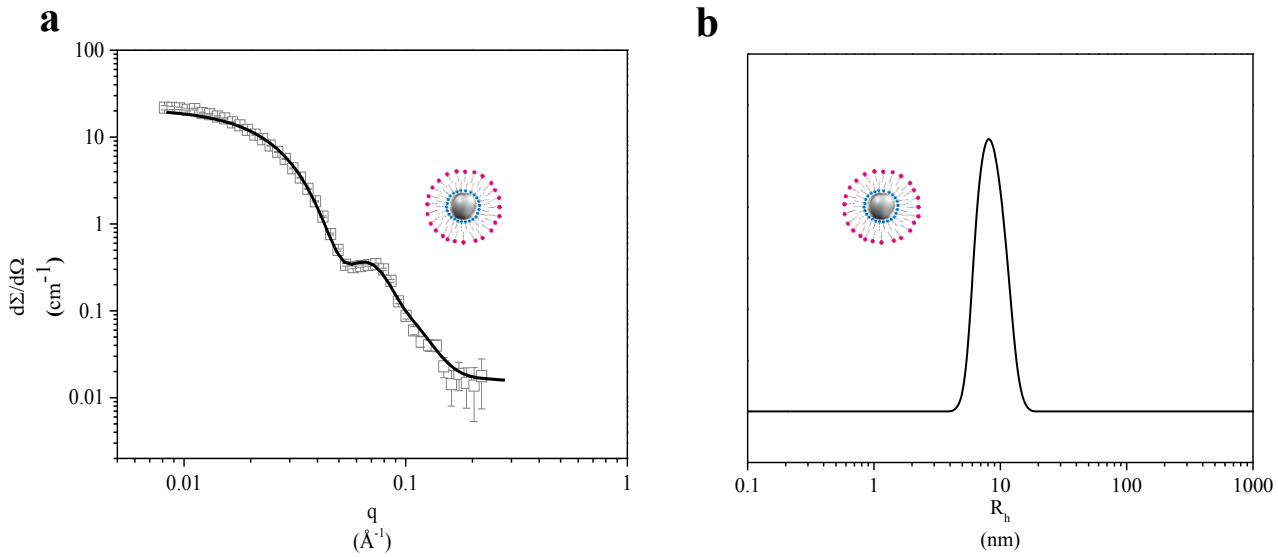

Figure 4.2.1: *SANS experimental data together with the fitting curve (panel a) and hydrodynamic radius distribution obtained from DLS measurements (panel b) for the same 18LPC/SPION suspension in D_2O.*

$$P_{core\text{-}shell}(q)=\frac{1}{V^2}\left[3V_{core}\left(\rho_{core}-\rho_{shell}\right)\frac{\left[sin\left(qr_{core}\right)-qr_{core}cos\left(qr_{core}\right)\right]}{\left(qr_{core}\right)^3}+3V_{shell}\left(\rho_{shell}-\rho_{D_2O}\right)\frac{\left[sin\left(qr_{shell}\right)-qr_{shell}cos\left(qr_{shell}\right)\right]}{\left(qr_{shell}\right)^3}\right]^2 \quad (4.2.1)$$

The scattering length density of the inorganic core (ρ_{core}) and the organic shell (ρ_{shell}) were calculated according to their composition and molecular volume as: $\rho_{Fe_3O_4}^{neutron} = 6.9 \cdot 10^{-6}\text{Å}^{-2}$(core),

$\rho_{oleic\ acid}^{neutron} = 7.8 \cdot 10^{-8}\text{Å}^{-2}$ (inner layer), $\rho_{oleylamine}^{neutron} = -1.7 \cdot 10^{-7}\text{Å}^{-2}$(inner layer), $\rho_{18LPC}^{neutron} = 2.6 \cdot 10^{-7}\text{Å}^{-2}$ (outer layer) and $\rho_{D_2O}^{neutron} = 6.3 \cdot 10^{-6}\text{Å}^{-2}$. [103]

The curve reported in figure 4.2.1, panel a was obtained from an optimal fitting of equation 4.2.1 weighted by the two Schulz distribution where r_{core}, r_{shell}, p_{shell} and p_{core} were considered as the parameters to be optimized

The structural parameters obtained from the analysis of the collected SANS data are in Table 4.2.1. The good match between the experimental data and the fitting curve confirmed that the 18LPC/SPIONs were indeed characterized by a core-shell structure. In particular, the inorganic core turned out to have a radius of about 3 nm, while the organic shell, composed by the two amphiphilic layers, the inner one of oleic acid and oleylamine and the outer one of 18LPC, a thickness of 4 nm.

.

Table 4.2.1: *Structural parameters obtained from SANS and DLS measurements for 18LPC/SPION and 16LPC/SPION suspensions.*

	18LPC/SPIONs	**16LPC/SPIONs**
r $_{core}$ (nm)	2.7 ± 0.2	2.5 ± 0.3
p $_{core}$	0.27± 0.02	0.29± 0.03
r $_{shell}$ (nm)	3.6± 0.1	3.7 ± 0.2
p $_{shell}$	0.19± 0.01	0.20± 0.01
% solvent	10±1	35±3
D·10^6(cm^{2}s^{-1})	0.234 ± 0.008	0.276 ± 0.014
R$_h$ (nm)	10 ± 1	9 ± 1
D$_{cluster}$·10^6 (cm^{2}s^{-1})	---	0.0482 ± 0.0055
R$_{h,cluster}$ (nm)	---	51 ± 6

We also estimated the solvent fraction in the outer organic shell as 0.10. This was calculated by considering the fitted ρ_{shell} as the sum of the organic shell scattering length density plus D_2O scattering length density weighted by their respective volume fraction.

The 18LPC/SPION suspension was also characterized by means of DLS to investigate the SPION aggregation state. As reported in Figure 4.2.1, panel b, the 18LPC/SPION suspension is indeed composed by a single population of particles with a mean hydrodynamic radius (R_h) of about 8 nm. The total radius of 18LPC/SPIONs, (2.7 ± 0.5) nm core radius plus (3.6 ± 0.1) nm shell thickness,

with the allowance of a solvation shell around it, is reasonable agreement with the hydrodynamic radius provided by DLS.

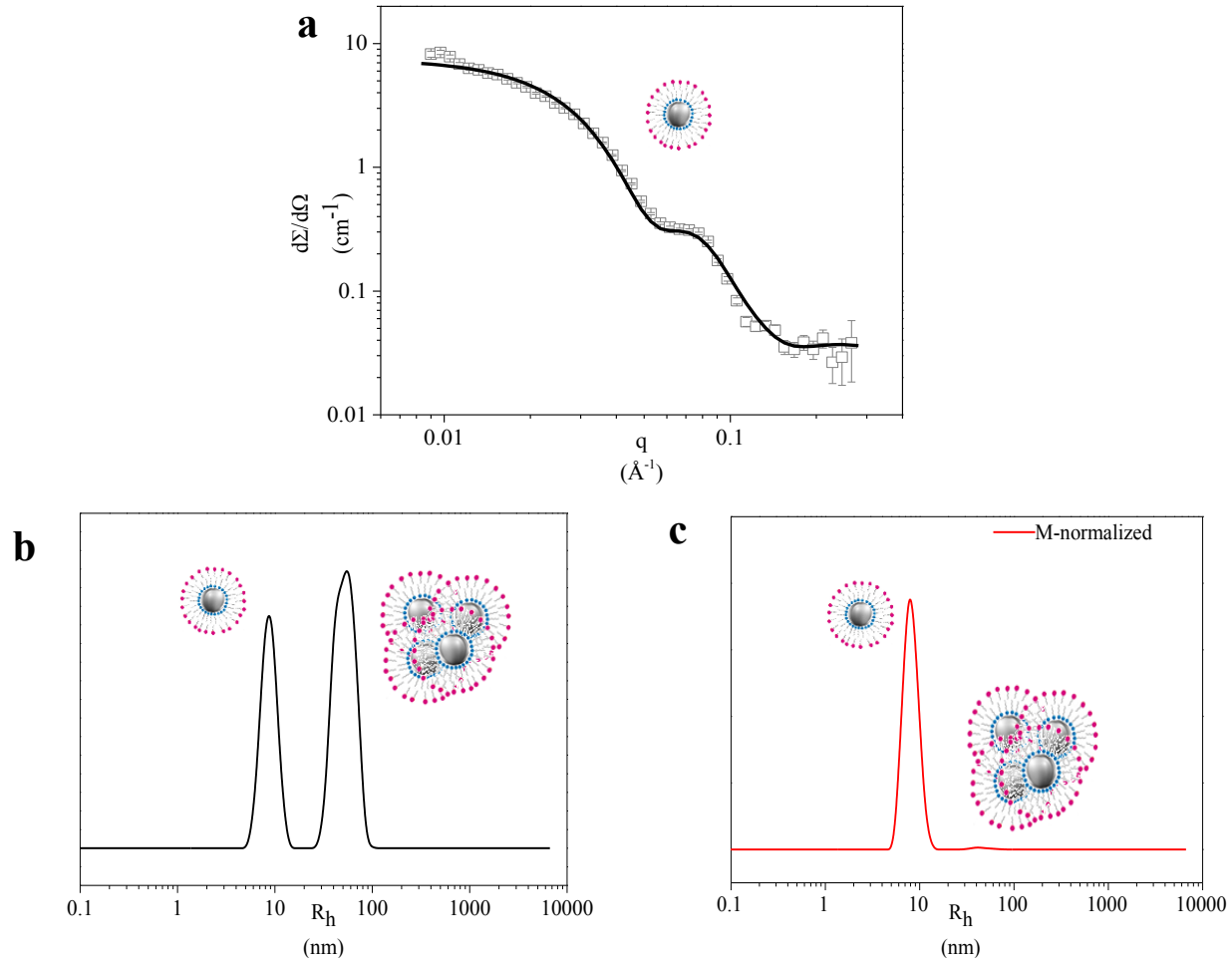

Figure 4.2.2: *SANS experimental data together with the fitting curve (panel a) and hydrodynamic radius distribution obtained from DLS measurements (panel b) for 16LPC/SPION suspension. In panel c the hydrodynamic radius distribution was normalized for the particle mass.*

The scattering of profile collected for 16LPC/SPION suspension (Figure 4.2.2, panel a) resembles the one observed for the 18LPC/SPION suspension. According to this observation, also for 16LPC/SPIONs the same spherical core-shell model was used to analyse the experimental data. Applying equation 4.2.1, weighted by the Schulz distribution, with $\rho_{16LPC}^{neutron} = 2.7 \cdot 10^{-7} Å^{-2}$, the parameters reported in Table 4.2.1 (second column) were optimized. 16LPC/SPIONs and 18LPC/SPIONs were prepared from the same SPION cyclohexane suspension, and thus, as expected, the structural parameters corresponding to the inorganic core radius were, within the errors, the same. The organic shell thickness resulted also to be, within the error, the same as for 18LPC/SPIONs. This result is reasonable since the 16LPC molecule differs from 18LPC one only for two CH_2 groups in the acyl chain, which means a few Å in terms of the hydrophobic tail length. Interestingly, the solvent

fraction in the organic shell resulted to be about 0.35, larger than the water amount present in the case of 18LPC/SPION. The higher solvent content in the outer shell suggests that in the functionalized SPION organic shell the 16LPC molecules are less closely packed than 18LPC ones.

The results obtained from SANS data analysis were compared with the DLS measurements. Figure 4.2.2, panel b, reports the intensity distribution of the hydrodynamic radius of the scattering particles. The 16LPC/SPION suspension did not only contained the isolated functionalized nanoparticles, but also a population of larger particles was detected with mean hydrodynamic radius of about 50 nm. This population was interpreted as SPION clusters. Owing to their large size and small concentration with respect to the isolated functionalized SPIONs, SPION clusters were not detected in the q-range explored during the SANS experiments, even if the increasing slope of the curve at small q values might suggest their presence.

The scattered intensity measured in the DLS experiments depends on both the mass squared and the concentration of the scattering objects. However, the distribution reported in Figure 4.2.2, panel b, can be converted into a concentration distribution by normalizing the scattering intensity considering that the particle mass (M) is proportional to its hydrodynamic radius cubed. The normalized intensity distribution of the hydrodynamic radius reported in Figure 4.2.2, panel c, shows that the actual contribution of the cluster is very low, corresponding to about 1% of the total scattered intensity.

4.3 Structural characterization of SPIONs functionalized with a cationic surfactant.

SANS and DLS were also combined for the characterization of the suspension of CTAB/SPIONs. Figure 4.3.1 (panel a) reports the SANS experimental data together with the fitting curve. The scattering length density of CTAB was calculated as $\rho_{CTAB}^{neutron} = -1.58 \cdot 10^{-7}\text{Å}^{-2}$.

The collected SANS data was significantly different in the low-q region from the one collected for the lysophosphatidylcholines-functionalized SPIONs. This difference was interpreted as produced by the presence of large SPION clusters, whose Guinier region (see Appendix A), sensitive to the particle size, was not detectable in the explored q-range. According to this interpretation, the model used to fit the experimental data was composed by the sum of two different form factors, accounting for the scattered intensity raised from the isolated functionalized SPIONs and the SPION clusters.

$$I(q) = \varphi_{core-shell} V_{sphere} P_{core-shell} + F(q) + bkg \tag{4.3.1}$$

with

$$P_{core\text{-}shell}(q)=\frac{1}{V^2}\left[\begin{array}{l} 3V_{core}\left(\rho_{core}-\rho_{shell}\right)\dfrac{\left[sin\left(qr_{core}\right)-qr_{core}cos\left(qr_{core}\right)\right]}{\left(qr_{core}\right)^3}+ \\ +3V_{shell}\left(\rho_{shell}-\rho_{D_2O}\right)\dfrac{\left[sin\left(qr_{shell}\right)-qr_{shell}cos\left(qr_{shell}\right)\right]}{\left(qr_{shell}\right)^3} \end{array}\right]^2 \quad (4.3.2)$$

$$F(q)=A(q)^{-m} \quad (4.3.3)$$

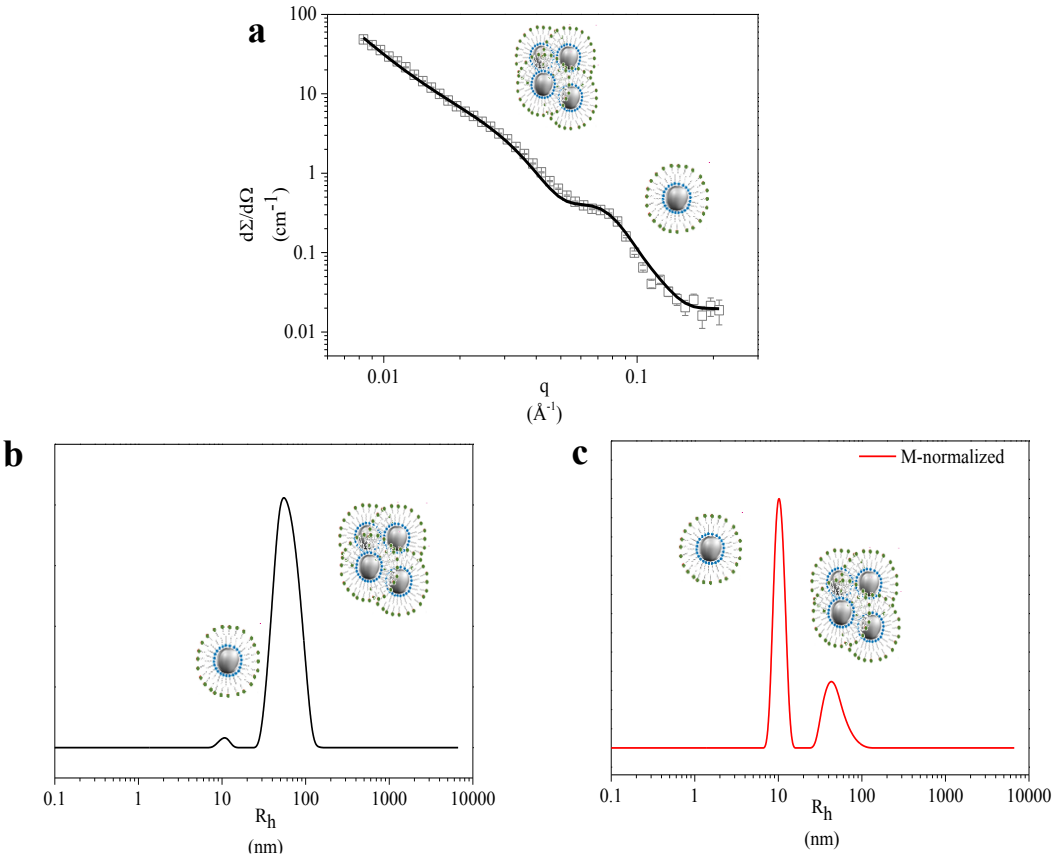

Figure 2.3.1: *SANS experimental data together with the fitting curve suspension (panel a) and hydrodynamic radius distribution obtained from DLS measurements (panel b) for CTAB/SPION suspension. In panel c the hydrodynamic radius distribution was normalized for the particle mass.*

The experimental data were interpreted according to equation 4.3.1. The scattered intensity was considered as the sum of a core-shell form factor ($P_{core\text{-}shell}(q)$), a power law ($F(q)$) and the background (bkg). $P_{core\text{-}shell}(q)$ was used to take into account the scattering raising from the isolated functionalized SPIONs as for 18LPC/SPIONs and 16LPC/SPIONs. $F(q)$ was added in the model to account for the scattered intensity produced by the clusters, where m is the exponent of the power law. Again, the Schultz distributions were included in the model to estimate the polydispersity on both the core radius and the shell thickness.

Table 4.3.1: *Structural parameters obtained from SANS and DLS measurements for CTAB/SPION suspension.*

CTAB/SPIONs				
r_{core} (nm)	p_{core}	r_{shell} (nm)	p_{shell}	% Solvent
2.4 ± 0.3	0.29± 0.04	3.9 ± 0.4	0.22± 0.02	55± 2
$D \cdot 10^6$ (cm^2s^{-1})	R_h (nm)	$D_{cluster} \cdot 10^6$ (cm^2s^{-1})	$R_{h,cluster}$(nm)	
0.215 ± 0.041	11 ± 2	0.0431 ± 0.0076	51 ± 1	

The structural parameter calculated for the isolated CTAB/SPIONs (Table 4.3.1) are in agreement with the ones obtained for the isolated 18LPC/SPIONs and 16LPC/SPIONs; hence, the surfactant does not sensibly affect the structure of the isolated functionalized SPIONs. Furthermore, the slope of the intensity increment at low-*q* values, produced by the clusters, was optimized, and it resulted to be about -3. This value confirms the mass-fractal structure of the SPION clusters. The significant contribution of the clusters to the scattered intensity in the SANS measurement, suggests that a larger amount of clusters is present within the suspension with respect to 16LPC/SPIONs.

DLS experiments were performed to characterize the cluster size in terms of their hydrodynamic radius ($R_{h,clusters}$). As showed in Figure 4.3.1, panel *c*, the two populations composing the CTAB/SPION suspension exhibit very similar hydrodynamic radius values with respect to the 16LPC/SPION suspension. Nevertheless, the contribution of the clusters to the scattered intensity is definitely higher, being ~30% (scattering particle number density).

4.4 The effect of surfactant structure on functionalized SPIONs.

The structure of the SPIONs functionalized with different amphiphilic molecules was characterized in detail, and the clustering tendency of the functionalized SPIONs was investigated. In particular, while 18LPC/SPIONs were obtained as a monodispersed aqueous suspension, in the case of both 16LPC and CTAB/SPIONs, cluster formation was observed with a larger amount of clusters in the CTAB/SPION suspension. The same SPIONs, surfactant concentration and operating conditions were adopted for SPION functionalization; thus the different behavior of the three systems is ascribable only to the different aggregation properties of the used surfactants.

SPION functionalization through hydrophobic interactions is a process strongly affected by the self-aggregation properties of the used surfactant. Indeed, the aggregation tendency of an amphiphilic molecule can be thermodynamically described as a difference of the standard chemical potentials, between the single surfactant molecules dispersed in the solution and those within the aggregate. This difference, which accounts for the number of molecules involved in the process, is the gain of Gibbs

free energy of the aggregate formation and is strictly related to a characteristic concentration, known as Critical Micelle Concentration (CMC). In the approximation of the phase model separation, the CMC corresponds to the specific concentration of surfactant above which it self-assembles into micelles.[104] At high CMC values, the aggregation free energy is small and, thus, the surfactants present a poor tendency to self-aggregate. On the other hand, at low CMC values, the aggregation free energy is large and consequently the aggregate formation is the thermodynamically favorite condition for the surfactant molecules.

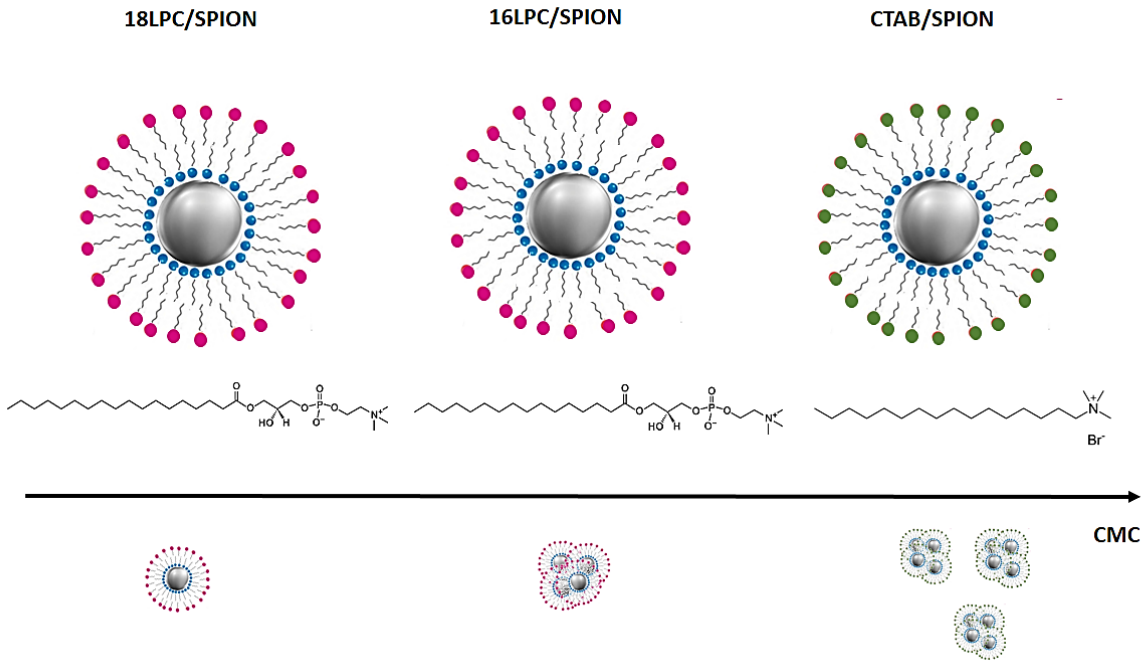

Figure 4.4.1: *Schematic representation of SPIONs and surfactant structures. The clustering tendency is represented as a function of the CMC values of the surfactants.*

18LPC and 16LPC are characterized by a CMC value corresponding to the range of $0.4\text{-}0.6\cdot10^{-6}$ M and $4.0\text{-}8.0\cdot10^{-6}$ M respectively (Figure 4.5.1).[105, 106] The different CMC value indicates that 18LPC molecules are less stable in the water solution and thus exhibit a larger aptitude to self-assemble with respect to 16LPC. This different behavior can be ascribed to the longer hydrophobic tail of 18LPC, since both 18LPC and 16LPC share the same polar head. On the other hand, CTAB is characterized by a CMC value in the range of $0.9\text{-}1.0\,10^{-3}$M, significantly higher than that of both 18LPC and 16LPC. CTAB CMC high value reflects the electrostatic repulsion among the cationic polar heads of the surfactants as the micelle settle down. Thus, the three surfactants used to prepare functionalized SPIONs are characterized by increasing CMC values, and thus decreasing aggregation tendency, in the following order 18LPC<16LPC<CTAB. The description of the aggregation process

for the surfactant solutions can be adopted for the SPION surface functionalization. Similarly, a coating free energy can be introduced as the difference of the standard chemical potentials between the surfactant molecules dispersed in the solution and the surfactant molecule in the SPION coating. A larger chemical potential associated to the surfactant molecules in the solution will correspond to a smaller coating free energy and thus to a less efficient coverage of SPION surface. Thus, the different aggregation behavior reflects the surfactant efficiency in coating the SPIONs and in their stabilization as isolated functionalized SPIONs or clusters. As a result, while 18LPC/SPIONs are stable in aqueous media as isolated functionalized nanoparticles, 16LPC/SPIONs and CTAB/SPIONs are characterized by an increasing amount of clusters, which reflects the increasing inefficiency of the surfactant molecules in coating the hydrophobic SPIONs.

In principle by choosing the appropriate molecules the size and the size distribution of the functionalized SPIONs can be tuned. Specifically, the physico-chemical characterization highlighted that surfactant CMC can be used as a reference parameter to rationally design functionalized SPIONs according the desired size. Indeed, the control of the size of the nanoparticles is a very important task, since their biodistribution is strongly driven by their dimensions.[8]

Chapter 5 - *18LPC/SPIONs as Effective MRI Contrast Agents*

The optimized functionalization strategy was demonstrated to be a successful approach for the preparation of stable aqueous suspensions of functionalized SPIONs. Furthermore, as discussed in Chapter 4, the aggregation properties of the amphiphilic molecules, used to functionalize SPIONs surface, have a strong impact on the self-organization of the functionalized SPIONs. Indeed, SPION clustering was observed in some of the investigated samples. In this Chapter are reported the results of the experiment that were carried out to explore an actual applicability of the functionalized SPIONs as MRI contrast agents. Specifically, *in vitro* as well as *in vivo* experiments were performed on the monodispersed suspension of 18LPC/SPIONs.

5.1 18LPC/SPIONs as MRI negative contrast agents: *in vitro* experiments.

Preliminary experiments were carried out in collaboration with Dr. Luca Menichetti (Consiglio Nazionale delle Ricerche, Pisa, Italy) to estimate the reduction of the transversal relaxation time (T_2) of the water protons induced by 18/LPC SPIONs. The 18LPC/SPIONs were initially tested in phantom systems at 1.5 and 3 T, which are the magnetic field values approved for clinical use. The phantoms consisted of a culture cell plate containing 18LPC/SPIONs in H_2O or 1% agar gel solution at different concentrations. These experiments were fundamental to assess 18LPC/SPIONs as able to simultaneously increase transverse relaxivity (r_2, $ml \cdot mg^{-1} s^{-1}$) and decrease longitudinal relaxivity (r_1, $ml \cdot mg^{-1} s^{-1}$) of the water protons (see Chapter 1). In general, high values of r_2/r_1 ratio indicate that the tested system as a sensitive MRI T_2-contrast agent.[107, 108]

The r_2/r_1 ratio was evaluated for phantoms containing 18LPC/SPIONs with iron concentration in the range of 0.0016-2.5 mg/ml. As a result, the r_2/r_1 ratio increased linearly with the concentration of 18LPC/SPIONs. In particular, the data collected for the suspension of 18LPC/SPIONs with iron concentration 1 mg/ml are reported in Table 5.1.1.

As expected, the iron oxide core of the SPIONs induced a larger effect on the transverse relaxation time (T_2) rather than longitudinal (T_1) relaxation time. The 18LPC/SPIONs showed higher r_2 values for 1% agar gel compared to H_2O solutions (both at 1.5 and 3 T). This demonstrated an increased contrast enhancement produced by 18LPC/SIPIONs when dissolved in agar gel rather than H_2O. This effect can be reasonably interpreted as due to the increased viscosity and decreased water diffusion

coefficient compared to H_2O solutions [109]. According to the tissue-like nature of the agar gel phantoms used, the obtained results suggested the potentiality of the tested system for biomedical exploitation. The r_2/r_1 ratios calculated for 1% agar gel solutions showed significantly higher values compared to other available commercial systems [110], and highlighted the efficacy of the tested SPIONs as negative contrast agents for MRI[111].

Table 5.1.1: *Values of r_2, r_1 and r_2/r_1 ratio obtained at 1.5 and 3 T for the 18LPC/SPIONs with iron concentration 1 mg/ml in H_2O and 1% agar gel solutions.*

	1.5 T		**3 T**	
	H_2O	**1% Agar gel**	**H_2O**	**1% Agar gel**
r_2 ($ml \cdot mg^{-1} s^{-1}$)	16.6 ± 0.2	39.7 ± 0.4	14.6± 0.1	38.4± 0.4
r_1 ($ml \cdot mg^{-1} s^{-1}$)	-	0.78 ± 0.08	-	0.33·± 0.04
r_2/r_1	-	51 ± 5	-	122 ± 10

5.2 18LPC/SPIONs biocompatibility.

Preliminary *in vitro* investigations are fundamental to verify the effective biocompatibility and to ensure the theoretical safety towards biological environment of 18LPC/SPIONs, thereby allowing for their potential *in vivo* use.

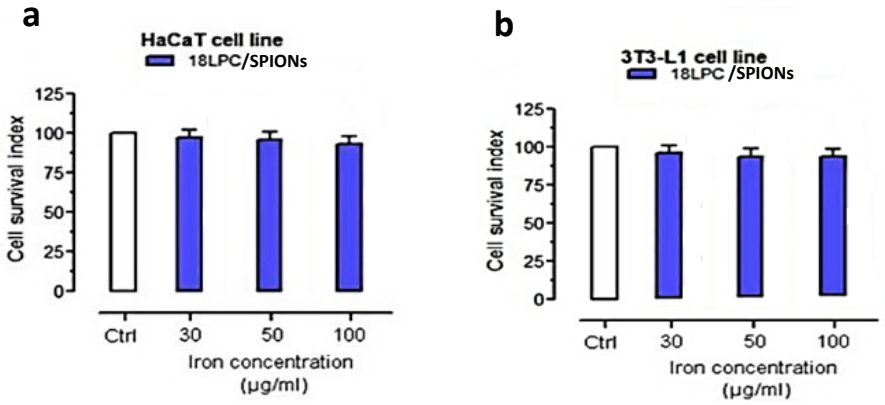

Figure 5.2.1: *Cell survival index, evaluated by the MTT assay and the live/dead cell ratio for human HaCaT keratinocytes (panel a) and murine 3T3-L1 fibroblasts (panel b) after 48 h of incubation with the indicated iron concentration (µg/ml) of 18LPC/SPIONs. Data are expressed as percentage of untreated control cells and are reported as mean of five independent experiments.*

In vitro bioscreens (see Appendix D), based on the estimation of a ‘‘cell survival index’’ which is derived concurrently from the evaluation of the cellular metabolic activity (MTT colorimetric assay) and the determination of live/dead cells ratio (TC20 automated cell counter). The bioscreens were performed by the research group of Prof. Carlo Irace (Dipartimento di Farmacia, Università di Napoli “Federico II”).

In Figure 5.2.1, the data collected for two different cultured cell lines upon 18LPC/SPIONs injection are reported. The cell survival index resulted in all the investigated cases higher than 80%, indicating that even at high iron concentration (100 mg/ml), no significant biological effects are associated to 18LPC/SPIONs. This outcome is an excellent starting point in the design of effective SPION-based MRI contrast agents.

5.3 18LPC/SPIONs as negative MRI contrast agents: *in vivo* experiments.

Once their biocompatibility was proved, 18LPC/SPIONs were injected in a small animal model (healthy rat) to test *in vivo* their pharmacokinetics and the extent of the negative contrast associated to the reduction of the transverse proton relaxation time (T_2). The *in vivo* tests (see Appendix D) were carried out by the research group of Dr. Luca Menichetti (CNR Institute of Clinical Physiology, Pisa). A larger effect on T_2 relaxation time was recorded in the liver of the animal (for both right and left side), which is consistent with 18LPC/SPIONs being mainly sequestered by the reticuloendothelial hepatic tissue (Kupffer cells).[112, 113] An increase of the transverse proton relaxation rate (R_2) value was already observed 10 minutes after 18LPC/SPIONs injection and reached a maximum after 60 minutes. This is in agreement with a progressive accumulation of the nanoparticles in the tissue for excretion (Figure 5.3.1). Conversely, we did not detect a significant variation of R_2 over time in other organs such as kidneys or heart. Thus, the map of the relaxation rate demonstrated an efficient effect *in vivo*, which is promising for future applications of 18LPC/SPIONs in diagnostics.

The progressive increase of the transverse relaxation rate (R_2) detected over time for a *Region Of Interest* (ROI) selected in the right hepatic lobe and confirmed that 18LPC/SPIONs are recognized by the reticuloendothelial system. The 18LPC/SPIONs produced a measurable reduction in the MR signals in the rat liver after injection, indicating their potential for use as T_2 MRI (negative) contrast agents.

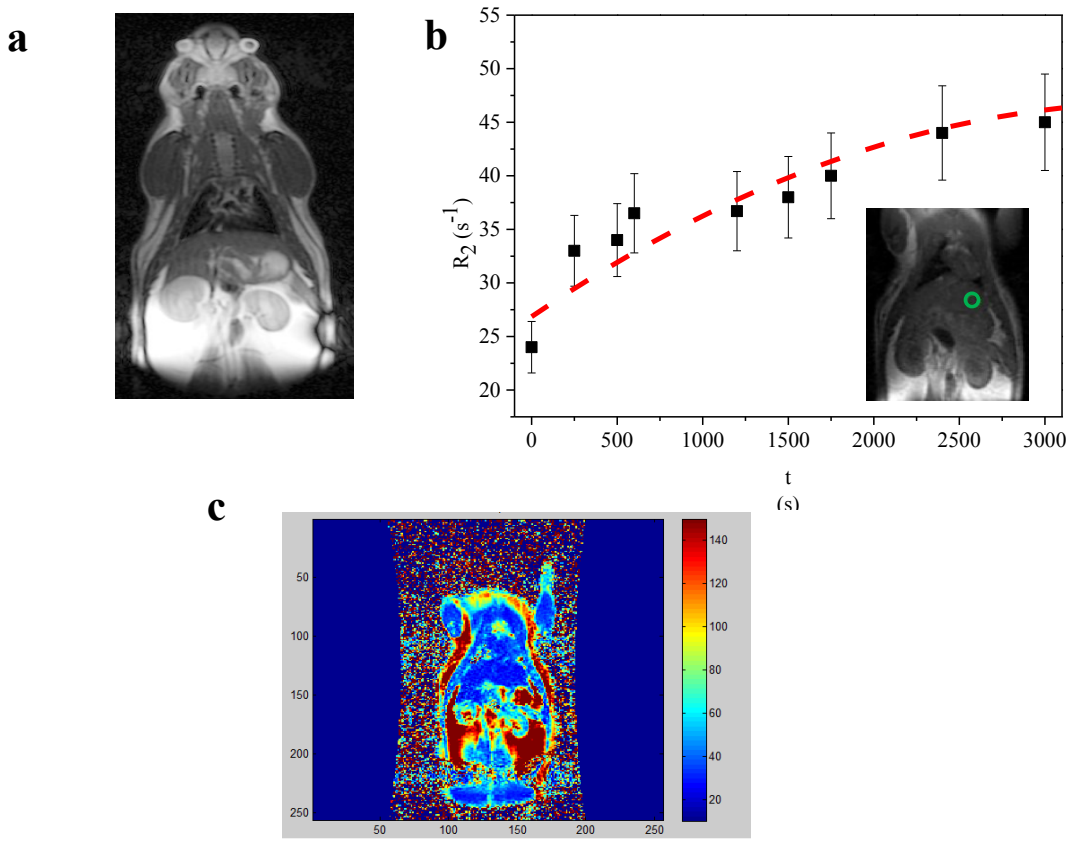

Figure 5.3.1 *T_2-weighted image of a coronal view of the animal (Wistar rat) before injection of the 18LPC/SPIONs (panel a) Transverse relaxation rate ($R_2=1/T_2$, s^{-1}) measured after bolus injection in the tail vein of 18LPC/SPIONs (iron concentration 0.017 mg/ml) in 0.9% NaCl solution (panel b). The corresponding ROI (see insert in panel b) was selected in the coronal plane covering the liver: mean±SE indicated by the gray intervals. Representative T_2-mapping MRI image of a coronal view after injection (t=3 min) of the 18LPC/SPIONs (panel c)*

Chapter 6 - *Interaction between Functionalized SPIONs and Lipid Bilayers*

The safe application of nanotechnology devices in biomedicine requires fundamental understanding on how they interact with the different components of biological systems. In this respect, the cellular membrane, the cell envelope, certainly represents an important target or barrier for nanosystems. A physic-chemical approach was established for the collection of relevant information about the behavior of the functionalized SPIONs in the presence of lipid membrane model systems. In particular, Neutron Reflectometry (NR) and Quartz Crystal Microbalance with Dissipation monitoring (QCM-D) techniques were combined. The interaction between 18LPC/SPIONs or CTAB/SPIONs and lipid bilayer that are mimic of eukaryotic cellular plasma membrane was investigated.

6.1 Functionalized SPIONs and lipid bilayers.

The use of supported lipid bilayers is a common choice for the characterization of the interaction between membranes and extracellular systems. [85] In the present case, lipid bilayers were prepared using the zwitterionic phospholipid, POPC, as major component, and a small fraction of the negatively charged POPG phospholipid was introduced in the bilayer to reproduce the slightly negative charge of the surface of the plasma membrane. In addition, lipid bilayers with an increasing cholesterol content were prepared. Cholesterol is an important component of the cellular membranes; it has the fundamental role of regulating their fluidity and packing, as well as of taking part to several processes necessary to the cell life.[114, 115] Recently, the potential role of cholesterol in the interaction between the cellular membrane and potential drugs has been pointed out.[77] The physiological abundance of cholesterol in the cellular membrane varies considerably depending upon the cell type. In general the cholesterol amount ranges between 20 and 50% w/w. [84, 115, 116] Thus, by exploring different cholesterol concentrations, corresponding to 20% and 30% of total lipid weight, the influence of different lipid bilayer fluidity levels on the interaction with the functionalized SPIONs was taken into account.

The interaction between functionalized SPIONs and the lipid bilayers was investigated through combined NR and QCM-D measurements according to the procedure described in Chapter 2. In

particular, 18LPC/SPIONs (z-potential corresponding to -2.2 ± 0.8 mV) and CTAB/SPIONs (z-potential corresponding to 44 ± 2 mV) were studied. The 18LPC/SPIONs were demonstrated to be a promising system for MRI application (Chapter 5). Inversely, the CTAB/SPIONs were chosen as non-biocompatible systems, since CTAB molecules are able to induce a strong membrane destabilization effect, ascribable to their positive charge.[117] The obtained results were complemented with Dynamic Light Scattering (DLS) measurements and Cryogenic Transmission Electron Microscopy (Cryo-TEM) images, through which the interaction between the functionalized SPIONs and lipid vesicles was characterized. Fundamental concepts of Neutron Reflectometry can be found in Appendix B.

6.2 Supported lipid bilayer characterization.

Neutron reflectivity measurements were performed with monocrystalline silicon blocks cut along the 111 direction (Sil'tronix Silicon Technologies) with 5x8 cm^2 area used as solid substrates for the lipid bilayers. Initially NR data were collected for the bare silicon blocks in order to characterize their surface in terms of the native silicon oxide thickness and roughness (Appendix B). In Figure 6.2.1, a representative set of measurements referring to one of the used silicon block is reported. As mentioned in Chapter 2, data corresponding to D_2O, H_2O and SMW were collected and simultaneously fitted according to a single layer model corresponding to the SiO_2 present on the block surface. As a result, all the silicon blocks used for the NR measurements were characterized by a SiO_2 layer with thickness in the range of 7-10 Å and a surface roughness of 2 Å.

Lipid bilayers were deposited on the silicon substrates through the vesicle fusion protocol.[78, 79, 118] For this purpose single unilamellar vesicles with the appropriate lipid composition and total lipid concentration of 0.5 mg/ml were prepared in D_2O phosphate buffer through the lipid film method[80]. The vesicles suspension was injected in the flow-cell for solid-liquid reflectometry and equilibrated with the surface of the silicon support for 30 min. Then pure D_2O was injected into the cell, leading to the rupture of the vesicles and formation of the desired planar lipid bilayers as confirmed by the measurements described below. As in the case of the bare silicon substrates, reflectivity data were collected in D_2O, H_2O and SMW and simultaneously fitted in order to characterize the structure of the lipid bilayers.

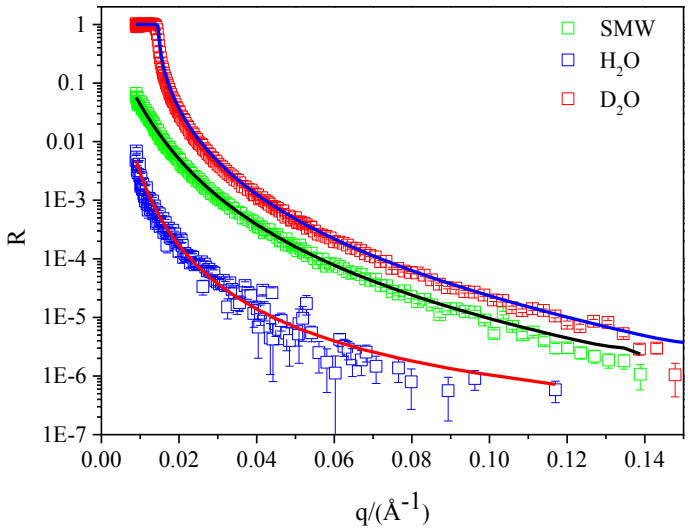

***Figure 6.2.1**: Neutron reflectivity experimental data together with the corresponding fitting curves for one of the used silicon block. The reported data refers to three different contrasts as indicated in the legend.*

In Figure 6.2.2 reflectivity data collected for the three prepared lipid bilayers (POPC/POPG (90/10 w/w), POPC/POPG/CHOL (70/10/20 w/w/w) and POPC/POPG/CHOL (60/10/30 w/w/w)) in D_2O, are reported together with the fitting curves. The experimental data collected for all the three lipid systems were modeled with a five-layer model. The first layer referred to the native silicon oxide and its structural parameters were kept fixed and equal to those obtained from the analysis of the bare surfaces. A second layer was ascribed to the thin water layer (3±1 Å thickness) that might be present between the lipid bilayer and the support. The remaining three layers referred to the lipid bilayers.

POPC and POPG molecules were considered as composed by two different regions with different scattering length density. Glycerol-phosphocholine and glycerol-phosphoglycerol, the headgroups respectively of POPC and POPG, is the polar portions of the phospholipid molecules, facing the support and the bulk aqueous solvent. The 1-palmitoyl-2-oleoyl acyl chains, present in both POPC and POPG, is the hydrophobic portion of the bilayer, which stays away from the aqueous solvent. In the case of the POPC/POPG (90/10 w/w) mixture, the scattering length density (ρ) of the different bilayer regions was calculated from the scattering length of POPC and POPG and the molecular volumes of the two phospholipids.[103]

For each region of the POPC/POPG bilayer the thickness, the solvent fraction and the roughness were evaluated from fitting the 5-layer model to the experimental data. In the case of the cholesterol containing lipid bilayers, the scattering length density of both the headgroups and the acyl chains was optimized in order to locate the cholesterol position within the bilayers. As starting value, the nominal amount of cholesterol as expected from preparation was used, under the hypothesis that it as completely embedded in the acyl chains of the phospholipids. The analysis of the neutron reflectivity

data confirmed that the prepared supported lipid bilayers were symmetric, with the same parameters values for the inner and the outer headgroup.[119]

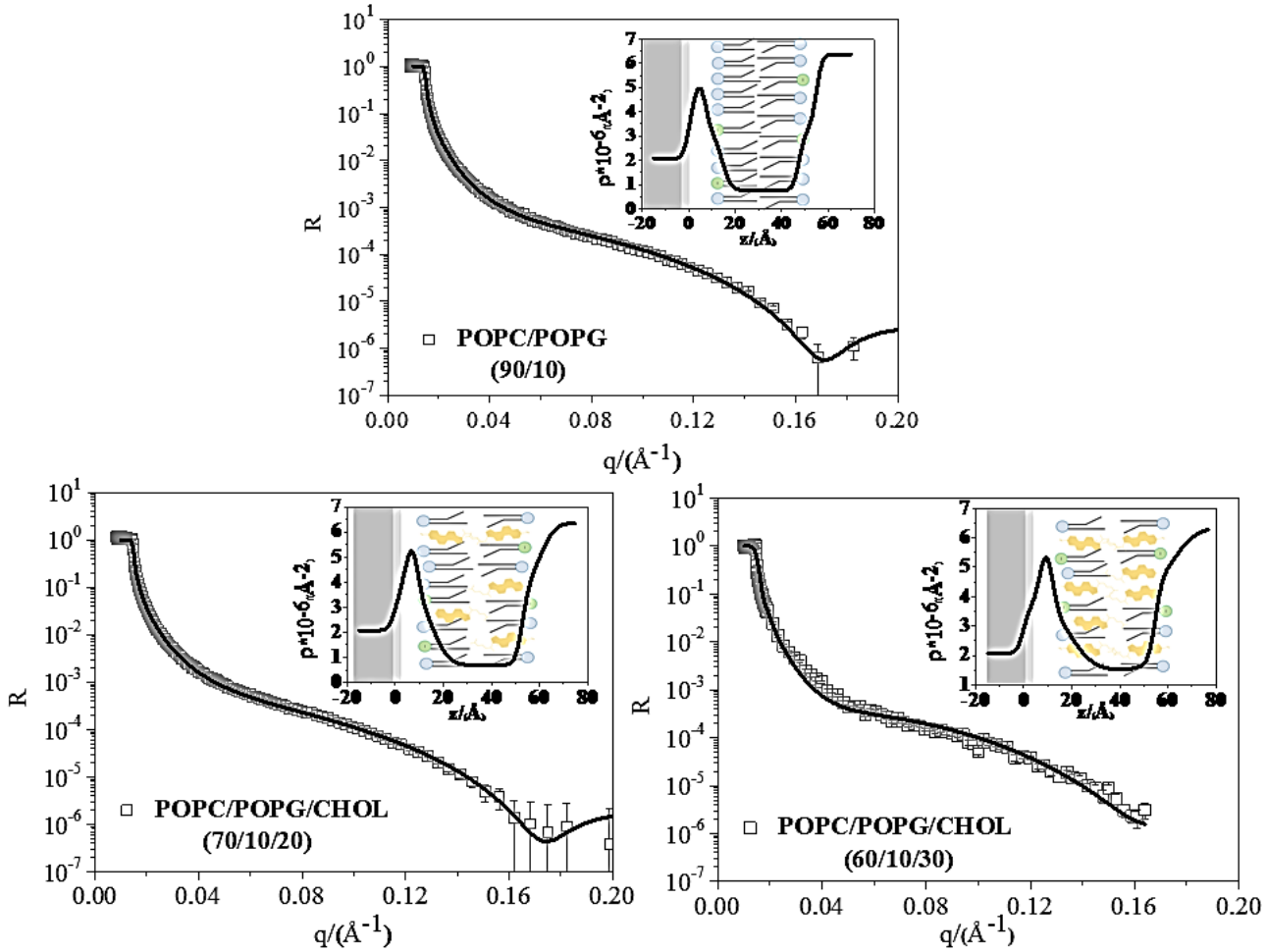

Figure6.2.2: *Neutron reflectivity experimental data collected in D_2O together with the corresponding fitting curve for the POPC/POPG (90/10 w/w), POPC/POPG/CHOL (70/10/20 w/w/w) and POPC/POPG/CHOL (60/10/30 w/w/w), as reported in the legend. In each graphs the obtained scattering length density profile, showing the structure of the supported lipid bilayers, is also reported.*

From the analysis of the neutron reflectivity data, the ρ-profile can be calculated. As discussed in Appendix B, the ρ-profile indicates how the sample composition varies along the direction perpendicular to the sample surface (z). As expected, the cholesterol has a significant influence on the structure of the bilayers, as shown in the ρ-profiles (Figure 6.2.2) and from the fitting parameters reported in Table 6.2.1. By considering the cholesterol as positioned within the hydrophobic region of the bilayers, the calculated ρ value according to the used cholesterol percentage corresponds to $-1.9 \cdot 10^{-7}$ Å^{-2} for POPC/POPG/CHOL (70/10/20) and $-1.4 \cdot 10^{-7}$ Å^{-2} for POPC/POPG/CHOL (60/10/30) as opposed to the nominal value of $-3 \cdot 10^{-7}$ Å^{-2} for pure aliphatic chains. However, the optimization of

the scattering length density corresponding to the acyl chain region as well as headgroups regions resulted in significantly different ρ values. Furthermore, the presence of an increasing amount of cholesterol led to an increase of the thickness and roughness of the bilayer and affected more the ρ of the tail region than that of the polar headgroup regions. These evidences are in agreement with the conclusion reported in the literature that locates the cholesterol mostly in the region of the hydrophobic tails with a small molecular portion containing the OH-group close to the polar headgroups.[114, 120]

In principle, the hydrophobic region of the acyl chains should avoid water penetration. Thus, the content of water in this region, estimated through the fitting procedure is an indicator of the effective coverage of the silicon block produced by the lipid bilayers. In the present case, according to the results reported in Table 6.2.1, we estimated the coverage degrees for the prepared lipid bilayers as in the range of 90-80% of the support surface.

The obtained bilayers were found to be perfectly stable even after several steps of flushing solvent, and thus they could be used for the characterization of the interaction with the functionalized SPIONs.

Table 6.2.1: *Optimized parameters for the characterized supported lipid bilayers.*

Bilayer composition	**Thickness (Å)**	**$\rho \cdot 10^{-6}$ ($Å^{-2}$)**	**Solvent fraction**	**Roughness (Å)**
POPC/POPG (90/10)				
Headgroups	7±1	1.85 *fixed*	0.3±0.1	5±1
Acyl chains	30±2	-0.29 *fixed*	0.1±0.1	2±1
POPC/POPG/CHOL (70/10/20)				
Headgroups	7±1	1.65±0.02	0.4±0.1	5±1
Acyl chains	35±2	-0.15±0.02	0.1±0.1	2±1
POPC/POPG/CHOL (60/10/30)				
Headgroups	7±1	1.65±0.02	0.5±0.1	7±1
Acyl chains	36±3	-0.11±0.02	0.2±0.1	2±1

6.3 Interaction between functionalized SPIONs and supported lipid bilayers.

1 ml of the suspensions functionalized SPIONs, with iron concentration of 2mg/ml, were injected in the cells containing the previously investigated lipid bilayers. The functionalized SPIONs in D_2O suspension was left in contact with the lipid bilayers for 30 min and then was flushed with aqueous solvent to remove the excess of SPIONs. The first set of reflectivity data was then collected. The measurement in D_2O was repeated after a further flushing step in order to verify that the solvent flushing was not affecting the interaction by means of mechanical shear. Since no differences were observed from the first collected curve, the sample was assumed to be stable. Data corresponding to the SMW and H_2O contrasts were recorded as well.

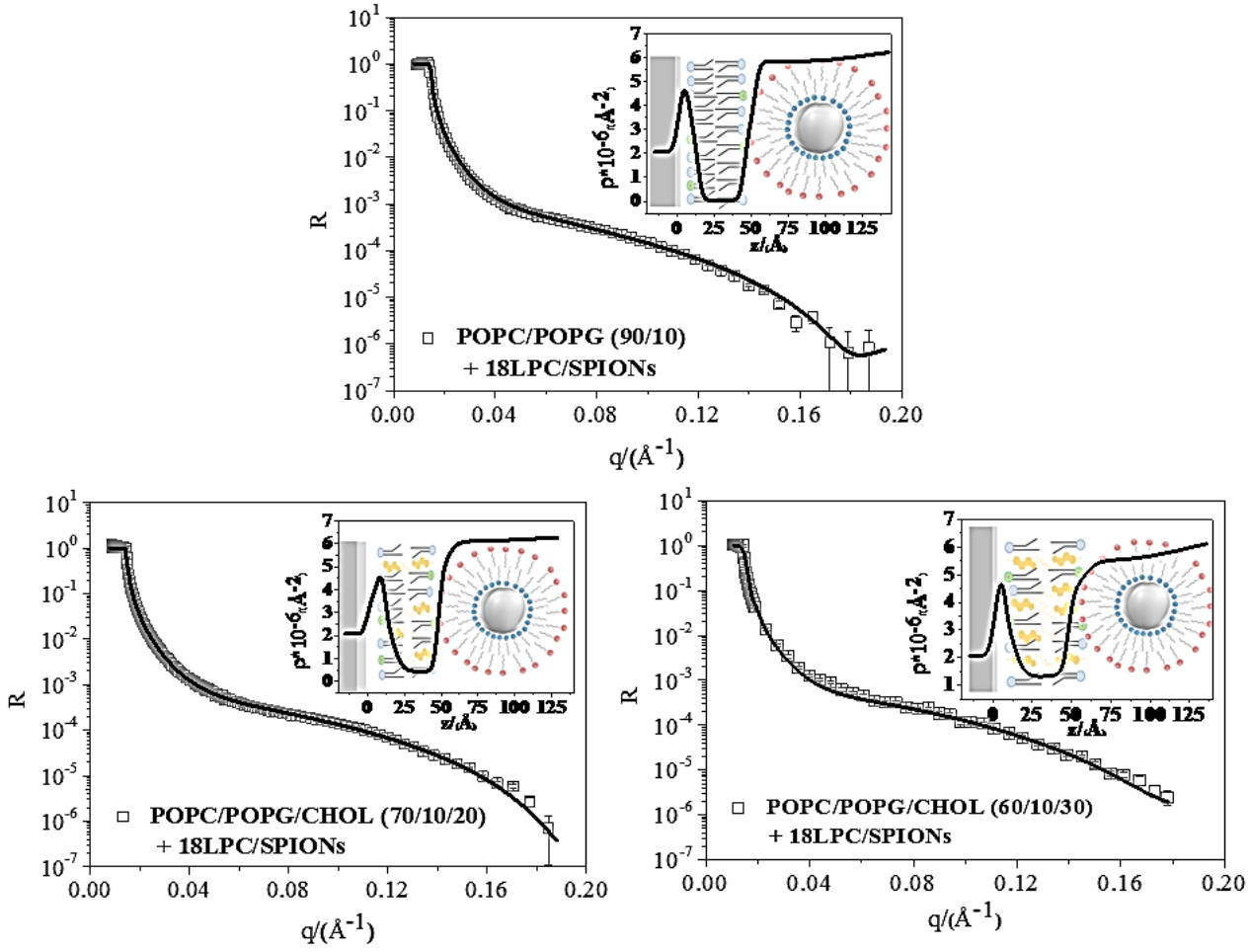

Figure 6.3.1: *Neutron reflectivity experimental data collected in D_2O together with the corresponding fitting curve for the POPC/POPG (90/10 w/w)+18LPC/SPIONs, POPC/POPG/CHOL (70/10/20 w/w/w)+18LPC/SPIONs and POPC/POPG/CHOL (60/10/30 w/w/w)+18LPC/SPIONs, as reported in the legend. In each graphs the obtained scattering length density profile, showing the structure of the supported lipid bilayers in the presence of the functionalized SPIONs is also reported.*

Owing to a large contrast between the D_2O solvent and the full-hydrogenated lipid bilayer, the experiments in heavy water are the most sensitive to the structural changes in the membrane and will

be discussed in details. However, as above mentioned, the fitted curve along with the results reported in Tables 6.3.1 and 6.3.3 were obtained by the simultaneous fitting of the experimental data in the different solvents.

Table 6.3.1: *Optimized parameters for the characterized supported lipid bilayers. The distinction between the inner headgroups (close to the silicon support) and outer headgroups (in contact with the functionalized SPIONs) was introduced to indicate that the two layers are no longer linked to have the same parameter values.*

Bilayer composition	**Thickness (Å)**	**$\rho \cdot 10^{-6}$ ($Å^{-2}$)**	**Solvent fraction**	**Roughness (Å)**
POPC/POPG (90/10) +18LPC/SPIONs				
Inner Headgroups	7±1	1.85±0.02	0.20±0.01	2±1
Acyl chains	31±1	-0.28±0.01	0.05±0.01	2±1
Outer Headgroups	7±1	1.85±0.02	0.45±0.02	5±2
18LPC/SPIONs	70±5	1.1±0.2	0.90±0.01	25±5
POPC/POPG/CHOL (70/10/20) +18LPC/SPIONs				
Inner Headgroups	7±1	1.60±0.02	0.32±0.02	5±1
Acyl chains	33±1	-0.15±0.1	0.09±0.01	2±1
Outer Headgroups	7±1	1.44±0.02	0.45±0.03	7±2
18LPC/SPIONs	65±5	1.1±0.2	0.90±0.01	25±5
POPC/POPG/CHOL (60/10/30) +18LPC/SPIONs				
Inner Headgroups	7±1	1.60±0.02	0.35±0.03	5±1
Acyl chains	35±2	-0.11±0.1	0.12±0.02	2±1
Outer Headgroups	7±1	1.40±0.02	0.55±0.04	10±2
18LPC/SPIONs	70±5	1.1±0.2	0.85±0.02	25±5

Neutron reflectivity experimental data collected upon 18LPC/SPIONs injection into the cells containing the lipid bilayers are reported in Figure 6.3.1. In order to build an appropriate model to interpret the experimental data, different possibilities were considered for spatial arrangement of the

nanoparticles in the presence of the lipid bilayers. As reported in the literature the interaction between nanoparticles and supported lipid membranes can lead to a superficial adsorption of the nanoparticles with a penetrating degree strictly dependent upon the nanoparticle surface. Inclusion of the nanoparticles into the bilayer, and even the partial or complete removal of lipids from the support (thus causing membrane disruption), were also reported. [67, 86] The occurrence of each of the previously listed events is mostly determined by the surface and the colloidal properties of the nanoparticles.[82] Indeed, charged nanoparticles, and in particular cationic ones, have strong impact on lipid membranes, frequently inducing their disruption.[70-72] Taking into account all this information, different models were built in order to identify the one mostly likely to explain the experimental data.

As a result, the best fitting model obtained, shown in Figure 6.3.1, indicated the adhesion of 18LPC/SPIONs on the surface of the bilayers for all the investigated lipid systems. The ρ-profiles calculated for the investigated systems are reported in Figure 6.3.1 superimposed to a schematic representation of the samples according to the fitted model.

The fitted model is composed by 6 layers corresponding to the five ones previously used to describe the lipid bilayers, plus an additional layer inserted above the outer headgroup region accounting for the attachment of 18LPC/SPIONs. As indicated by the parameters reported in Table 6.3.1, the 18LPC/SPIONs layer has a very high solvent content, which means that a small fraction of the injected SPIONs attach to the bilayer surface, while most of them are probably removed by the flushing solvent step. Because of the large water fraction, which indicated a low nanoparticle density on the bilayer surface, the 18LPC/SPIONs layer resulted to be non-uniform and very diffuse. The presence of the 18LPC/SPIONs in contact with the bilayer surface slightly affected the structural parameters of the lipid bilayers. Indeed, even in the case of the POPC/POPG (90/10 w/w) bilayer, which is more fluid than the one containing cholesterol [121], the total bilayer thickness was unaffected by the 18LPC/SPIONs adsorption. These results suggested a weak interaction between the 18LPC/SPIONs and the surfaces of the bilayers.

The model adopted for the interpretation of the neutron reflectivity data was validated through experiments with QCM-D. The advantage of this technique is that the neutron reflectivity experimental conditions can be accurately reproduced, with the additional quantification of the mass of the absorbed 18LPC/SPIONs. In the present case, POPC/POPG (90/10 w/w) and POPC/POPG/CHOL (60/10/30 w/w/w) vesicle suspensions in phosphate buffer, with total lipid concentration 0.5 mg/ml, were injected into the cells. After 5min equilibration, H_2O was flushed. Upon verifying the effective formation of a stable lipid bilayer (typical frequency shift corresponding to ~-25 Hz [122]), the 18LPC/SPION suspension was injected. The nanoparticles were left interact

with the bilayer for about 30 min, as done during the NR experiments, and then the excess was washed out by flushing H_2O. The frequency shift associated to the overtone n=5 were used for the quantification of the absorbed 18LPC/SPIONs according to equation 2.5.1.

The 18LPC/SPION suspensions with iron concentration 2 mg/ml and 0.2mg/ml were used during the QCM-D experiments. The first set of measurements including the suspension with iron concentration 2 mg/ml were used to support the interpretation of the neutron reflectivity data as well as to estimate the amount of absorbed functionalized SPIONs (Figure 6.3.2, panel a, b). On the other hand, measurements using the suspension with iron concentration 0.2 mg/ml were performed in order to investigate the effect of the functionalized SPIONs concentration on the interaction with the lipid bilayer.

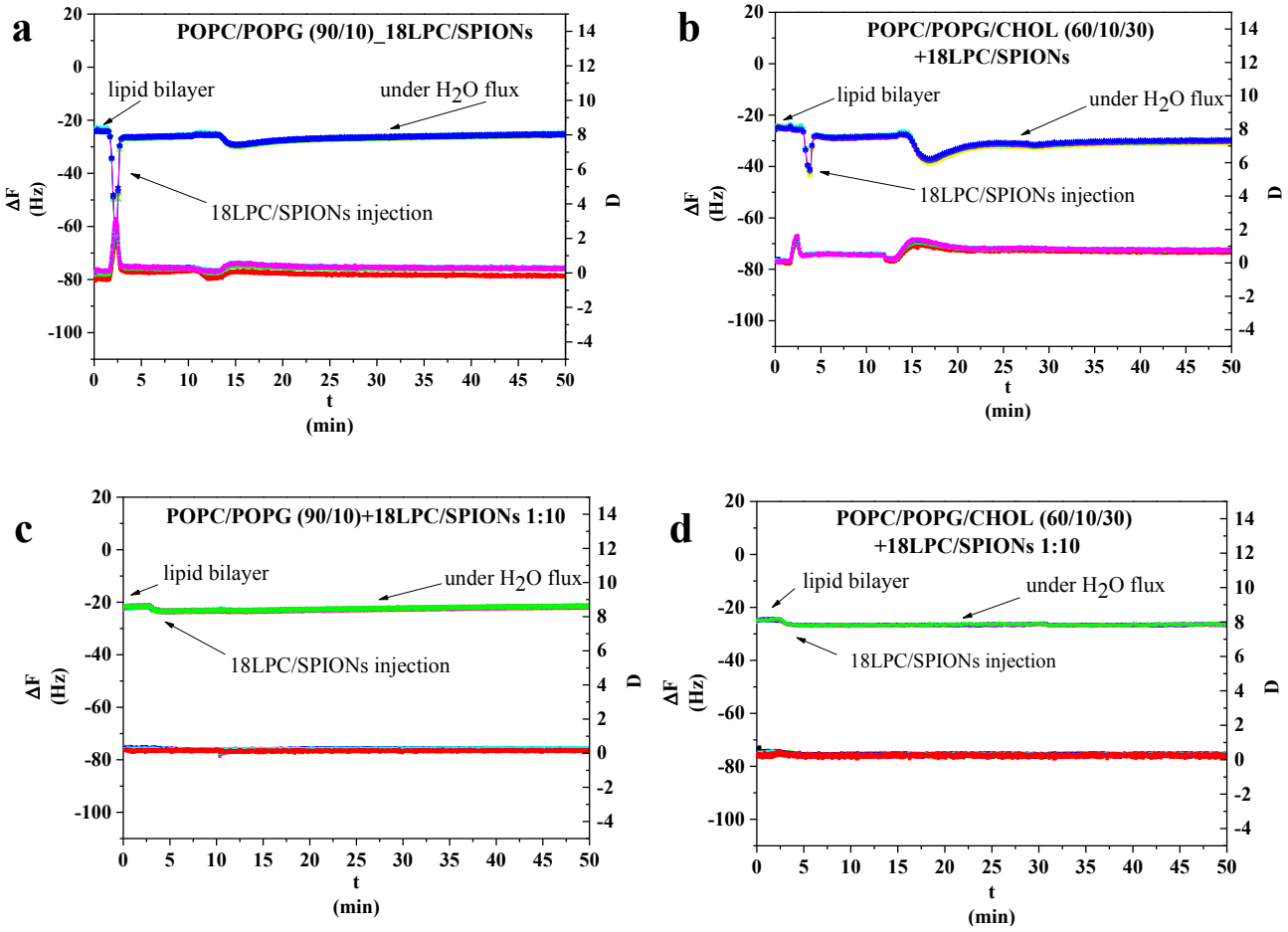

Figure 6.3.2: *Time-evolution of normalized frequency shift and dissipation factor curves obtained by QCM-D experiments for the POPC/POPG (90/10 w/w) and POPC/POPG/CHOL (60/10/30 w/w/w) before and after 18LPC/SPIONs with iron concentration corresponding to 2mg/ml and 0.2 mg/ml (18LPC/SPIONs 1:10) as reported in the legends. The upper curves represent always the normalized frequency shifts ($\Delta f_n/n$) while dissipation factors (ΔD_n) are always plotted in the lower part of the graphs. Transient peaks in the frequency shift and dissipation curves, induced by injection of media with different viscosity with respect to one already loaded into the chamber, were initially detected (panel a and b).*

In Figure 6.3.2 data collected for the lipid bilayers in the presence and in the absence of cholesterol, before and after 18LPC/SPIONs injection, are reported. Indeed, a significant decrease of $\Delta f_n/n$ was observed upon 18LPC/SPIONs injection for all the overtones. In all the performed experiments, the dissipation resulted to be about zero in most of the explored time interval and in particular in the region corresponding to the lipid bilayer and the lipid bilayer+18LPC/SPIONs under H_2O flux. This observation suggested that the lipid bilayers and the lipid bilayers in the presence of the functionalized SPIONs behaved as a supported rigid film. Therefore, equation 2.5.1 could be used to quantify the amount of absorbed 18LPC/SPIONs (Table 6.3.2) from the relative changes of the frequency shift values. For the POPC/POPG (90/10) bilayer, the mass increment ($\Delta\Delta m$) associated to the absorption of 18LPC/SPIONs was ~ 54.9 ng, which corresponds to about 4% of the initially injected nanoparticles. The amount of absorbed nanoparticles resulted to be influenced by the initial concentration of the nanoparticles. In fact, in the case of the POPC/POPG (90/10) bilayer exposed to a 10-fold diluted suspension 18LPC/SPIONs (Figure 6.3.2 panel c and d and Table 6.3.2) a smaller shift in frequency (~ -0.9 Hz) was observed, indicating a much lower adsorbed mass. Nevertheless, the percentage of adsorbed nanoparticles was found to be almost constant, within the experimental accuracy, with respect to the concentration of the injected solutions.

Table 6.3.2: *Mean normalized frequency shift (Δf) evaluated for both the lipid bilayer in the time range 2-3 min and the lipid bilayer after 18LPC/SPIONs injection under H_2O flux in the time range t=29-30min. The relative frequency shift ($\Delta\Delta f$) is reported together with the corresponding absorbed mass variation ($\Delta\Delta m$) calculated through equation 2 representing the absorbed 18LPC/SPIONs mass on the top of a lipid bilayer.*

Bilayer composition	**$\Delta f_{lipid\ bilayer}$ (Hz)**	**$\Delta f_{18LPC/SPIONs}$ (Hz)**	**$\Delta\Delta f$ (Hz)**	**$\Delta\Delta m$ (ng)**
POPC/POPG (90/10) +18LPC/SPIONs	-24.4±0.1	-27.7±0.1	3.1±0.2	55±3
POPC/POPG/CHOL (60/10/30) +18LPC/SPIONs	-25.5±0.1	-32.5±0.1	7.0±0.2	124±4
POPC/POPG (90/10) +18LPC/SPIONs 1:10	-24.4±0.2	-25.3±0.1	0.9±0.4	16±7
POPC/POPG/CHOL (60/10/30) +18LPC/SPIONs1:10	-25.4±0.3	-26.4±0.1	1.0±0.3	17±5

The amount of the adsorbed material depends on the composition of the target bilayer. In fact, upon addition of cholesterol into the bilayer (with composition 6/1/3 POPC/POPG/CHOL) the adsorbed mass of 18LPC/SPIONs resulted to be larger than the one observed for the cholesterol-free bilayer i.e. ~ 124 ng (~10% of the initially injected nanoparticles).

As in the previous case, a 10-fold dilution of the nanoparticle solution decreased the adsorbed mass while the percentage of adsorbed material, with respect to the used concentration of nanoparticles, remained almost constant.

The QCM-D experiments confirmed that the 18LPC/SPIONs did not remove, even partially, the lipid bilayers from the solid support. The observed relatively small shift in frequency as well as the absence of changes in the dissipation confirms the low coverage observed with NR. It should be noted that only a small fraction of the injected SPIONs available in the bulk solution adsorbs to the bilayers, suggesting low affinity to the surface. These results combined with those obtained by the analysis of NR data support the hypothesis of a system composed by the lipid bilayer with, on the top, an additional and very diffuse layer of functionalized SPIONs (Figure 6.3.3).

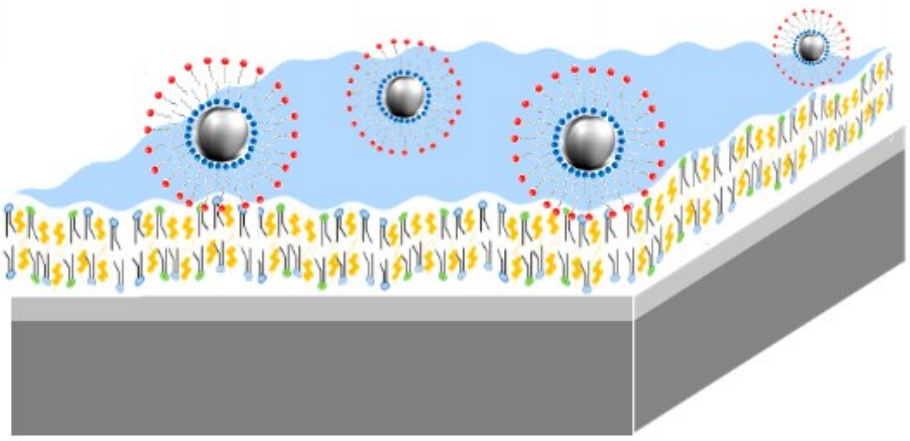

Figure 6.3.3: *Schematic representation based on NR and QCM-D results of the interaction between functionalized SPIONs and a lipid bilayer with 30%w/w cholesterol.*

In order to evaluate the effect of the surface charge of SPIONs, NR measurements were also performed exposing the lipid bilayers to CTAB/SPION suspension. The same protocol already described for 18LPC/SPIONs was applied. The system resulted to be perfectly stable after the removal of CTAB/SPIONs excess. By comparing the reflectivity curves reported in Figure 6.3.4 and in Figure 6.3.1, only small differences were observed upon addition of 18LPC/SPIONs or CTAB/SPIONs. According to this observation the model used to describe the interaction between the lipid bilayers and 18LPC/SPIONs was used also in the case of CTAB/SPIONs. As for 18LPC/SPIONs, a higher coverage of CTAB/SPIONs was found when the lipid bilayer contained the

largest amount of cholesterol. One plausible explanation is that this effect is related to the larger roughness of the bilayer surface induced by cholesterol. An optimal fit was obtained when the inner and the outer headgroup layers were not forced to have the same model parameters. Thus, the presence of the CTAB/SPIONs in contact with the lipid outer headgroups was confirmed by the reduction in its scattering length density. In contrast with respect to 18LPC/SPIONs, the CTAB/SPIONs caused a slight compression of POPC/POPG (90/10) bilayer, as indicated by the thickness reduction (Table 6.3.3). This effect resulted to be strongly influenced by the cholesterol content, since increasing the concentration of cholesterol in the lipid bilayer no significant change in the bilayer thickness was observed upon interaction with CTAB/SPIONs.

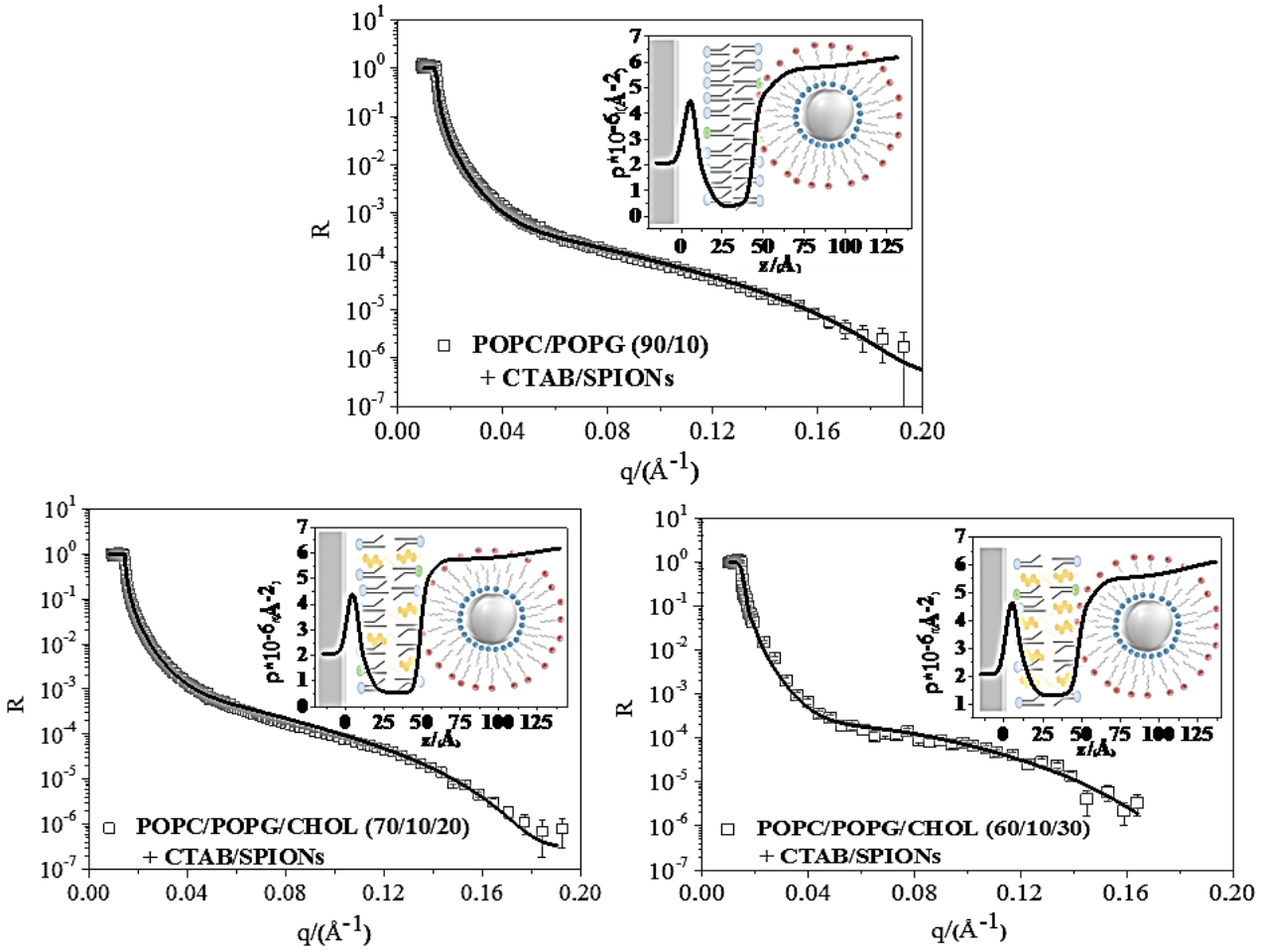

Figure 6.3.4: *Neutron reflectivity experimental data collected in D_2O together with the corresponding fitting curve for the POPC/POPG (90/10 w/w)+CTAB/SPIONs, POPC/POPG/CHOL (70/10/20 w/w/w)+CTAB/SPIONs and POPC/POPG/CHOL (60/10/30 w/w/w)+CTAB/SPIONs, as reported in the legend. In each graphs the obtained scattering length density profile, showing the structure of the supported lipid bilayers in the presence of the functionalized SPIONs is also reported.*

In conclusion, both 18LPC/SPIONs and CTAB/SPIONs are responsible for a weak superficial interaction with the lipid bilayers. Small differences were indeed observed between 18LPC/SPIONs

and CTAB/SPIONs with bilayer fluidity, determined by the cholesterol content, affecting the interaction. Indeed, for both 18LPC/SPIONs and CTAB/SPIONs a larger amount of nanoparticles was found on the bilayer surface of POPC/POPG/CHOL (60/10/30).

Table 6.3.3: *Optimized parameters for the characterized supported lipid bilayers. The distinction between the inner headgroups (close to silicon support) and outer headgroup (in contact with the functionalized SPIONs) was introduced to indicate that the two layers are no long linked to have the same parameter values.*

Bilayer composition	**Thickness (Å)**	**$\rho \cdot 10^{-6}$ ($Å^{-2}$)**	**Solvent fraction**	**Roughness (Å)**
POPC/POPG (90/10) +CTAB/SPIONs				
Inner Headgroups	7±1	1.85±0.02	0.22±0.01	2±1
Acyl chains	28±1	-0.28±0.01	0.10±0.01	2±1
Outer Headgroups	7±1	1.55±0.02	0.53±0.02	10±2
CTAB/SPIONs	65±5	0.3±0.1	0.90±0.01	25±5
POPC/POPG/CHOL (70/10/20) +CTAB/SPIONs				
Inner Headgroups	7±1	1.65±0.02	0.36±0.03	5±1
Acyl chains	32±2	-0.15±0.01	0.10±0.01	2±1
Outer Headgroups	7±1	1.44±0.02	0.50±0.02	10±2
CTAB/SPIONs	70±5	0.3±0.1	0.90±0.01	25±5
POPC/POPG/CHOL (60/10/30) +CTAB/SPIONs				
Inner Headgroups	7±1	1.65±0.02	0.40±0.02	5±1
Acyl chains	35±2	-0.11±0.01	0.13±0.03	2±1
Outer Headgroups	7±1	1.44±0.02	0.51±0.05	10±2
CTAB/SPIONs	70±5	0.3±0.1	0.80±0.02	25±5

On the other hand, the absorption of CTAB/SPIONs on the bilayers caused a thickness reduction, with a compression effect strongly dependent on the rigidity of the bilayer, thus POPC/POPG (90/10) resulted to be more affected than POPC/POPG/CHOL (60/10/30) by this compression. Nevertheless, the disruption of the lipid bilayer induced by functionalized SPIONs injection was never observed.

This consolidates the potentiality of the functionalized SPIONs as potential nanodevices for biomedical applications.

6.4 Interaction between 18LPC/SPIONs and lipid vesicles.

A further validation of the results obtained with supported lipid bilayers, which indicated the absence of a drastic effect of the functionalized SPIONs on the lipid membrane, was achieved by studying the interaction between 18LPC/SPIONs and lipid vesicles composed by POPC/POPG/CHOL (60/10/30 w/w/w). A vesicle suspension was prepared in the same way as for the neutron reflectivity experiments, and analyzed by means of DLS measurements in order to evaluate their hydrodynamic radius. As it is shown in Figure 6.4.1, a single population with mean hydrodynamic radius of 60±1 nm composes the vesicle suspension. 30 min after the addition of 18LPC/SPION suspension the DLS measurement was repeated.

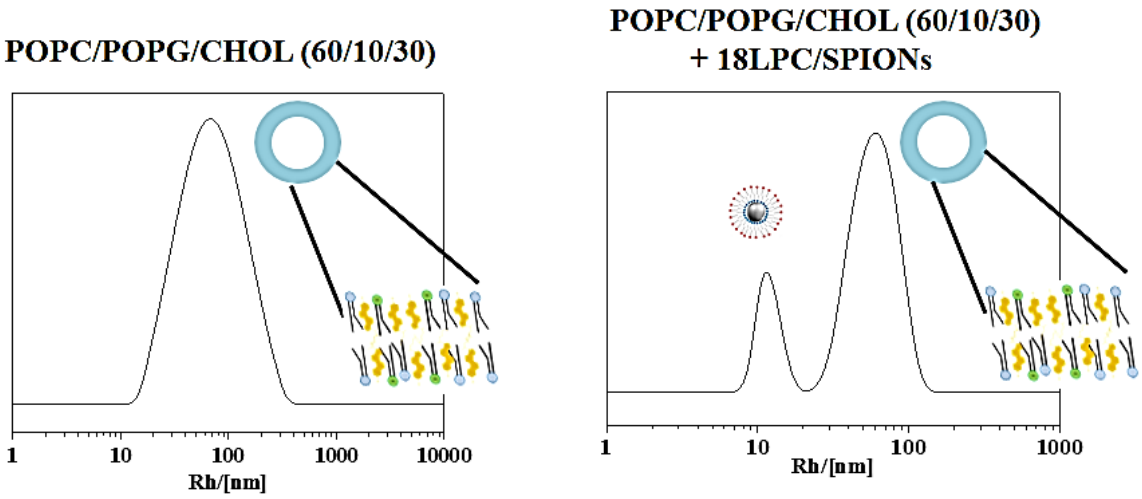

Figure 6.4.1: *Hydrodynamic radius distributions obtained from DLS measurements for the vesicle suspension (left) and the mixed suspension containing both 18LPC/SPIONs and lipids vesicles (right).*

Upon mixing with the 18LPC/SPIONs with the lipid vesicles, a second population appeared (see Figure 6.4.1, right) with mean hydrodynamic radius of 11±1 nm, which corresponds to the typical 18LPC/SPIONs size (Chapter 4). A population with mean hydrodynamic radius of 57±2 nm, comparable to the one initially observed, was also present. These results indicated that the mixed suspension of vesicles and 18LPC/SPIONs did not lead to a change of the size of the vesicle.

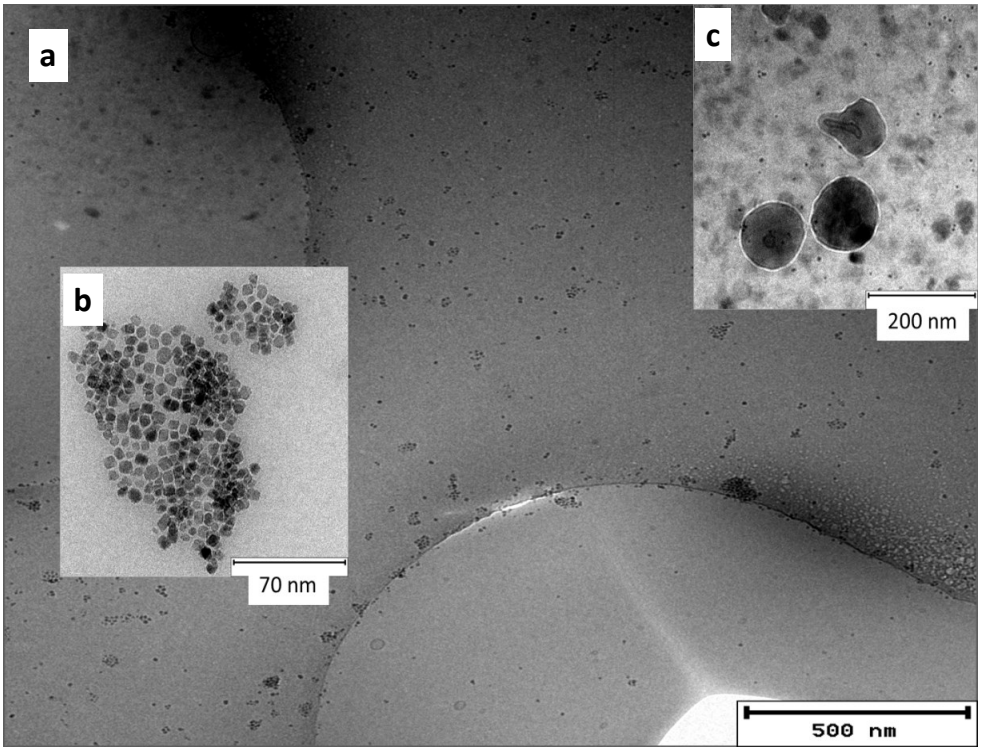

Figure 6.4.2: *Cryo-TEM images of the mixed suspension containing both 18LPC/SPIONs and lipid vesicles from POPC/POG/CHOL (60/10/30 w/w/w). The enlargements of the sample regions, where the 18LPC/SPIONs (panel b) and vesicles(panel c) are clearly observable, are superimposed to the overview image of the sample (panel a).*

DLS results were compared with Cryo-TEM images collected for the mixed suspension and reported in Figure 6.4.2. The presence of 18LPC/SPIONs is evident in the Cryo-TEM images due to their higher contrast with respect to the vesicles. The SPIONs detected in the images are characterized by a radius of about 3 nm, which corresponds to the Fe_3O_4 inorganic core, in agreement with the results on functionalized SPIONs reported in Chapter 3. Lipid vesicles are also detectable, as is more evident in the enlarged image, with a radius of about 50 nm.

Cryo-TEM images showed the presence in the mixed suspension of both 18LPC/SPIONs and lipid vesicles with sizes compatible with the hydrodynamic radius estimated by the DLS analysis. The two species appeared as separate entities with in the suspension and no trace of lipid bilayers as product of an eventual vesicle disruption is observed.

6.6 Exploring the behavior of functionalized SPIONs in the presence of lipid bilayers.

The interaction between nanoparticles and lipid bilayers can be an ambiguous research field, because of the several possible paths of interaction. By combining NR, QCM-D, DLS, and Cryo-TEM data, the interaction between CTAB or 18LPC-functionalized SPIONs and lipid bilayers with different

concentrations of cholesterol was characterized. The used bilayers presented lipid composition typical of mammalian plasma membranes and thus are suitable models to investigate the interaction with the functionalized SPIONs. Both 18LPC/SPIONs and CTAB/SPIONs interacted with the investigated lipid bilayers with a small amount of the initially injected functionalized SPIONs were found adsorbed on their surfaces. Specifically, 18LPC/SPIONs exhibited a weaker interaction with the lipid bilayer with respect to the CTAB/SPIONs. This difference was ascribed to the positive charge of the cationic surfactant used in the case of CTAB/SPIONs.

Interestingly, the interaction between the functionalized SPIONs and the lipid bilayer resulted to be dependent on the bilayer composition, i.e. a larger amount of absorbed nanoparticles was observed increasing cholesterol concentration. It is worth to note that even for the SPIONs functionalized with the cationic surfactant, disruption of the lipid bilayer was never observed. Hence, the strategy used to prepare the functionalized SPIONs is a promising route for the development of biocompatible systems, eventually suitable for both diagnostic and therapeutic purposes.

Chapter 7 - *Functionalized SPIONs for Theranostics and Multimodal Imaging*

The optimized functionalized protocol involves only one restriction: the selected molecules must present amphiphilic structure. This requirement is that the chosen molecule must present amphiphilic structure. With the aim of designing theranostic nanoparticles, SPIONs were functionalized with the amphiphilic ruthenium complex ToThyCholRu, recently demonstrated to be a promising antiproliferative drug. On the other hand, a NOTA-modified molecule, exhibiting amphiphilic structure, named NOTA-ol, was attached on the surface of the SPIONs. NOTA is a known chelator for ^{68}Ga, and thus NOTA-functionalized SPIONs can be dualmode contrast agents for combined MRI/PET imaging.

The development of multifunctional nanoparticles is extremely challenging. A first attempt of preparation and characterization of theranostic nanoparticles and multimodal imaging contrast agents is described here.

7.1 Design of theranostic nanoparticles.

The term “theranostics” was used for the first time in 1998 indicating “the ability to affect therapy or treatment of disease state”. [21] Theranostics, which is the combination of therapy and diagnosis, has become a relevant research field, since retarding cancer growth during the diagnostic procedure is a very attractive approach for the treatment of tumoral pathologies.

Recently, the amphiphilic ruthenium complex ToThyCholRu, designed by the research group where this Ph. D. project was carried out and synthesized by prof. Daniela Montesarchio (Dipartimento di Scienze Chimiche, Università degli Studi di Napoli “Federico II”), was highlighted as a potential ruthenium-based anticancer drug. As reported in Figure 7.1.1, ToThyCholRu present a large polar head including the octahedral ruthenium complex responsible for the anticarcer activity. Through the conjugation of the pyridine ligand with a nucleolipid molecule, the ruthenium complex was made amphiphilic. In particular, a cholesterol unit is the hydrophobic component of ToThyChlRu.

ToThyCholRu

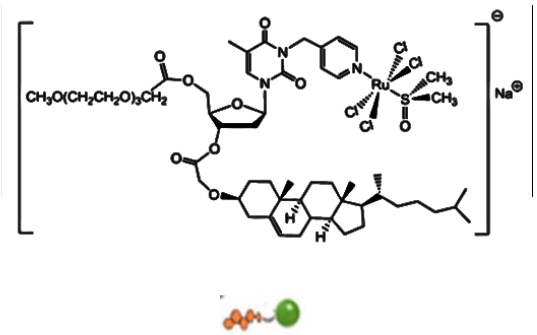

Figure 7.1.1: *Schematic representation of ToThyCholRu structure as indicated in the picture. The green-highlighted region indicates the polar portion of the molecule.*

Owing to its amphiphilic structure, ToThyCholRu can be easily incorporated into aggregates such as vesicles. Indeed, *in vitro* experiments have underlined liposomes as suitable nanocarries for ToThyCholRu with high cytotoxic activity towards cancer cell. [123-126]

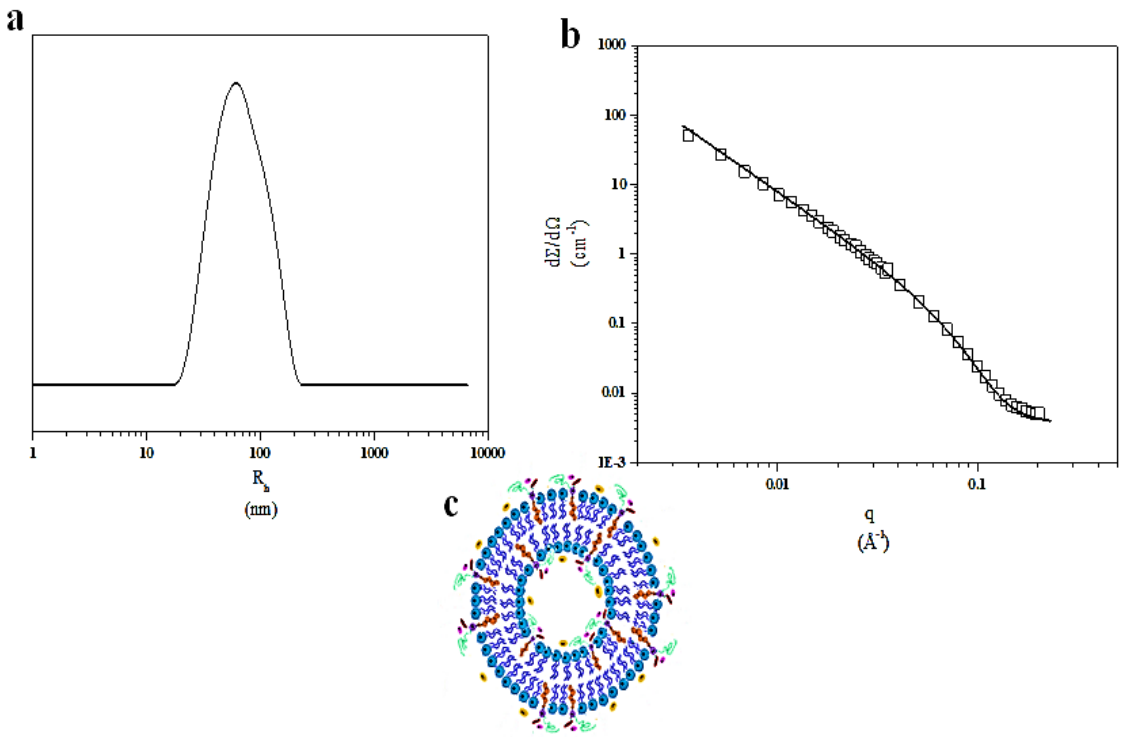

Figure 7.1.2: *Hydrodynamic radius distribution and SANS data collected for ToThyCholRu/DOTAP (30/70 mol/mol) liposome suspension (panel a and b respectively). Schematic representation of ToThyCholRu/DOTAP liposome (panel c). [123]*

In one of the recently published report, ToThyCholRu was suitably formulated with the biocompatible cationic surfactant 1,2-dioleoyl-3-trimethylammonium-propane (DOTAP) in order to prepare mixed vesicles. DLS and SANS measurements were combined to characterize the prepared

unilamellar vesicles that exhibited a mean hydrodynamic radius of 80 nm and a lamellar thickness of about 3 nm (Figure 7.1.2). The prepared vesicles loaded with ToThyCholRu showed promising antiturmoral activity toward several human cancer cell lines.[123]

ToThyCholRu, being an amphiphilic molecule and can be attached on the SPION surface through the functionalization approach presented in Chapter 2. ToThyCholRu-functionalized SPIONs are meant to combine the ToThyCholRu antitumoral activity, with the magnetic properties of the SPIONs inorganic core. Hence, ToThyCholRu-functionalized SPIONs can be detected through MRI and, at the same time, they can explicate anticancer activity, being potential theranostic nanoparticles.

7.2 Structural characterization of 18LPC-ToThyCholRu/SPIONs.

The mixture of ToThyCholRu and 18LPC, with molar ratio 10/90 and total concentration of $4 \cdot 10^{-3}$ m, was used to prepare functionalized SPIONs, named hereafter 18LPC-ToThyCholRu/SPIONs.

The DLS data collected on the suspension of 18LPC-ToThyCholRu/SPIONs exhibited the presence of two populations within the sample (Figure 7.2.1). By considering the average dimensions of the two populations (Table 7.2.1), it is reasonable to assume that the presence of ToThyCholRu has promoted the formation of small nanoparticle clusters with sizes less than 100 nm. As already discussed in Chapter 4, the intensity distribution can be converted in a concentration distribution by normalizing the scattered intensity in the approximation that $M \sim$. Thus, the relative amount of the two populations observed in the 18LPC-ToThyCholRu/SPION suspension was estimated. Indeed, the cluster population resulted to represent only the 10% of the total scattering particles.

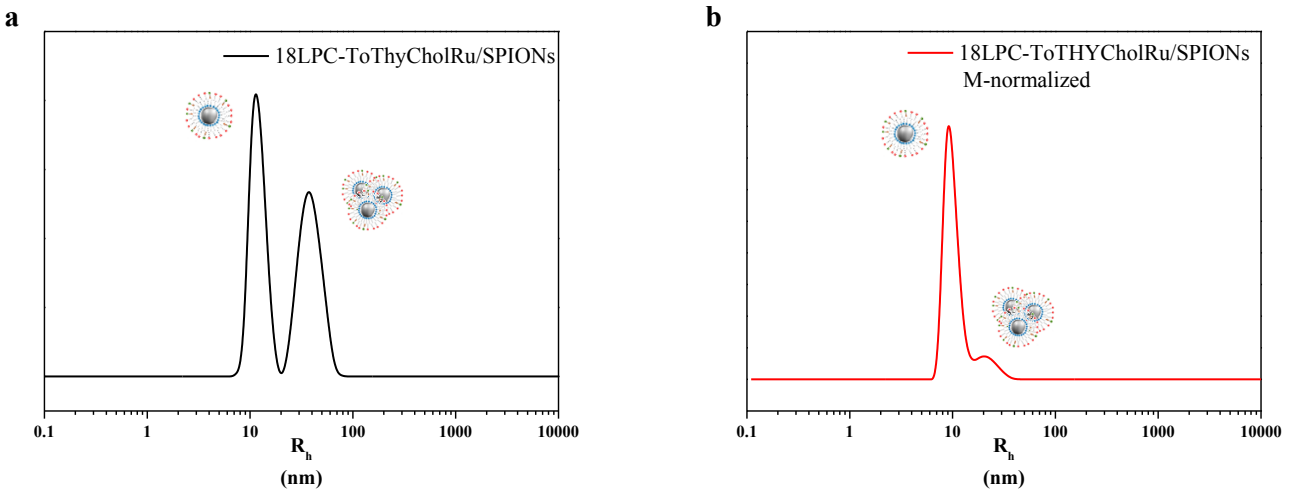

Figure 7.2.1: *Hydrodynamic radius distribution obtained from DLS measurements for 18LPC-ToThyCholRu/SPION suspension. In panel b the hydrodynamic radius distribution was normalized for the particle mass.*

Table 7.2.1: *Structural parameters obtained from DLS measurement for 18LPC-ToThyCholRu/SPION suspension.*

18LPC-ToThyCholRu/SPIONs			
$D \cdot 10^6$ (cm^2s^{-1})	**R_h (nm)**	**$D_{cluster} \cdot 10^6$ (cm^2s^{-1})**	**$R_{h\ cluster}$ (nm)**
0.215 ± 0.023	11 ± 1	0.0821 ± 0.0052	30 ± 3

The analysis of the SANS data (Figure 7.2.2) indicated that the core-shell form factor used for 18LPC/SPIONs was not sufficient, to fully reproduce the experimental data. This evidence suggested that, in agreement with DLS data, the suspension was not simply composed by the population of the isolated functionalized SPIONs.

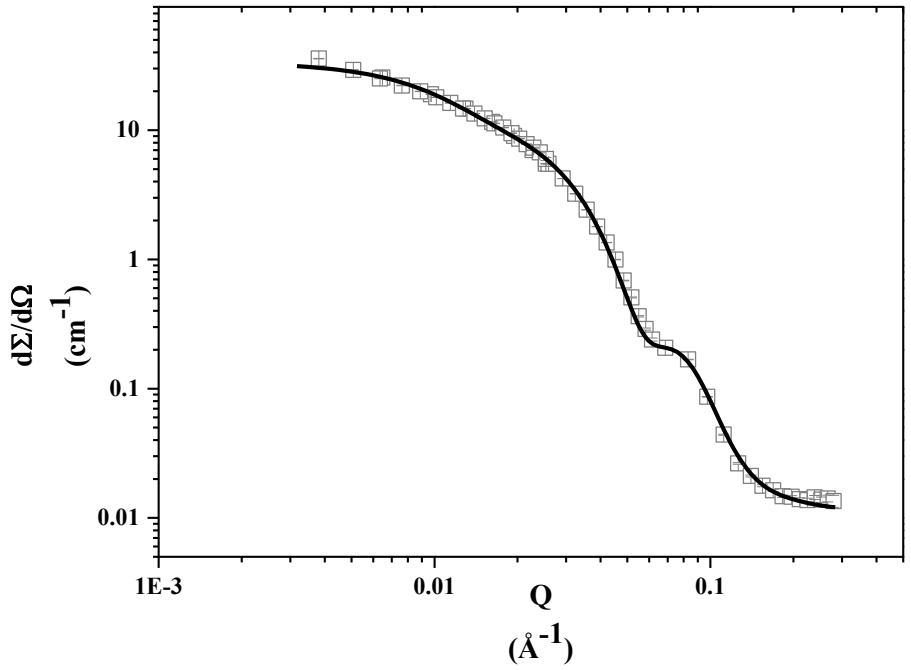

Figure 7.2.2: *SANS data collected for the 18LPC-ToThyCholRu/SPIONs together with the fitting curve.*

The structure of ToThyCholRu, reported in Figure 7.1.1 is very different from 18LPC. Indeed, it can be demonstrated, by calculations of the molecular volumes, that the polar head of ToThyCholRu (highlighted in green in Figure 7.1.1) is about four times larger than the polar head 18LPC. On the grounds of these structural differences, ToThyCholRu can be expected to be less efficient in coating the surface of the SPIONs with respect to 18LPC. There ensued the formation of clusters.

SANS data were analyzed according to equation 7.2.1. In this equation two form factors weighted by the volume fraction of the corresponding population were summed. The first one is the core-shell form factor ($P_{core\text{-}shell}(q)$) already introduced for the isolated functionalized SPIONs. The second term of equation 7.2.1 is a spherical form factor used to describe the cluster structure, where $r_{cluster}$ and $\rho_{cluster}$ are its associated scattering length density and radius[1]. Furthermore, equation 7.2.1 was weighted by a Schulz distribution of r_{core}, r_{shell} and $r_{cluster}$.

The following values of ρ were used to calculate single functionalized SPIONs and cluster scattering length density according to their composition: $\rho_{Fe_3O_4}^{neutron} = 6.9 \cdot 10^{-6}$Å^{-2}(core), $\rho_{oleic\ acid}^{neutron} = 7.8 \cdot 10^{-8}$Å^{-2} (inner layer), $\rho_{oleylamine}^{neutron} = -1.7 \cdot 10^{-7}$Å^{-2}(inner layer), $\rho_{18LPC}^{neutron} = 2.9 \cdot 10^{-7}$Å^{-2} (outer layer), $\rho_{ToThyCholRu}^{neutron} = 1.1 \cdot 10^{-6}$Å^{-2}(outer layer) and $\rho_{D_2O}^{neutron} = 6.3 \cdot 10^{-6}$Å^{-2}.

$$I(q)=\varphi_{core\text{-}shell}\ V_{core-shell}P_{core\text{-}shell}+\varphi_{cluster}V_{cluster}P_{cluster}+bkg \tag{7.2.1}$$

with

$$P_{core\text{-}shell}(q)=\frac{1}{V^2}\left[\begin{array}{l} 3V_{core}(\rho_{core}-\rho_{shell})\dfrac{\left[sin(qr_{core})-qr_{core}cos(qr_{core})\right]}{(qr_{core})^3}+ \\ +3V_{shell}(\rho_{shell}-\rho_{D_2O})\dfrac{\left[sin(qr_{shell})-qr_{shell}cos(qr_{shell})\right]}{(qr_{shell})^3} \end{array}\right]^2$$

and

$$P_{cluster}(q)=\frac{1}{V^2}\left[3V_{cluster}(\rho_{cluster}-\rho_{solv})\frac{\sin qr_{cluster}-qr_{cluster}\cos(qr_{cluster})}{qr_{cluster}}\right]^2$$

Table 7.2.1: *Structural parameters obtained from SANS measurement for 18LPC-ToThyCholRu/SPION suspension.*

18LPC-ToThyCholRu/SPIONs					
$\mathbf{r_{core}}$ **(nm)**	$\mathbf{p_{core}}$	$\mathbf{r_{shell}}$ **(nm)**	$\mathbf{p_{shell}}$	$\mathbf{r_{cluster}}$ **(nm)**	$\mathbf{p_{cluster}}$
2.7 ± 0.5	0.25 ± 0.01	3.7 ± 0.4	0.18 ± 0.02	20 ± 1	0.33 ± 0.02

[1] *In the case of the suspension of 18LPC-ToThyCholRu/SPIONs, the size and the shape of the clusters were accessible because the size was smaller and q-range was wider than in the case of CTAB/SPIONs (Chapter 4).*

The clusters present in the 18LPC-ToThyCholRu/SPION suspension can be considered spherical, as verified from the Cryo-TEM images (Figure 7.2.3), collected in collaboration with Dr. Marie-Sousai Appavou (Jülich Centre for Neutron Science, Garching Forschungszentrum, Germany).
The clusters are composed by the iron oxide cores and organic molecules, which presumably are exposed on the cluster surface and in the cluster core. Reasonably, the iron oxide cores, being coated by the oleic acid and oleylamine molecules, are stick together through hydrophobic interaction. According to this cluster structure, the inorganic core and an organic shell cannot be separately distinguished. Thus, each cluster was treated as a homogenous sphere, with a scattering length density calculated as the average of the scattering length densities of the individual components weighted by their volume fraction. The very good agreement obtained between the experimental data and the fitting curve(Figure 7.2.2), confirmed the interpretation of the 18LPC-ToThyCholRu /SPION suspension as composed by both isolated functionalized nanoparticles and small clusters.

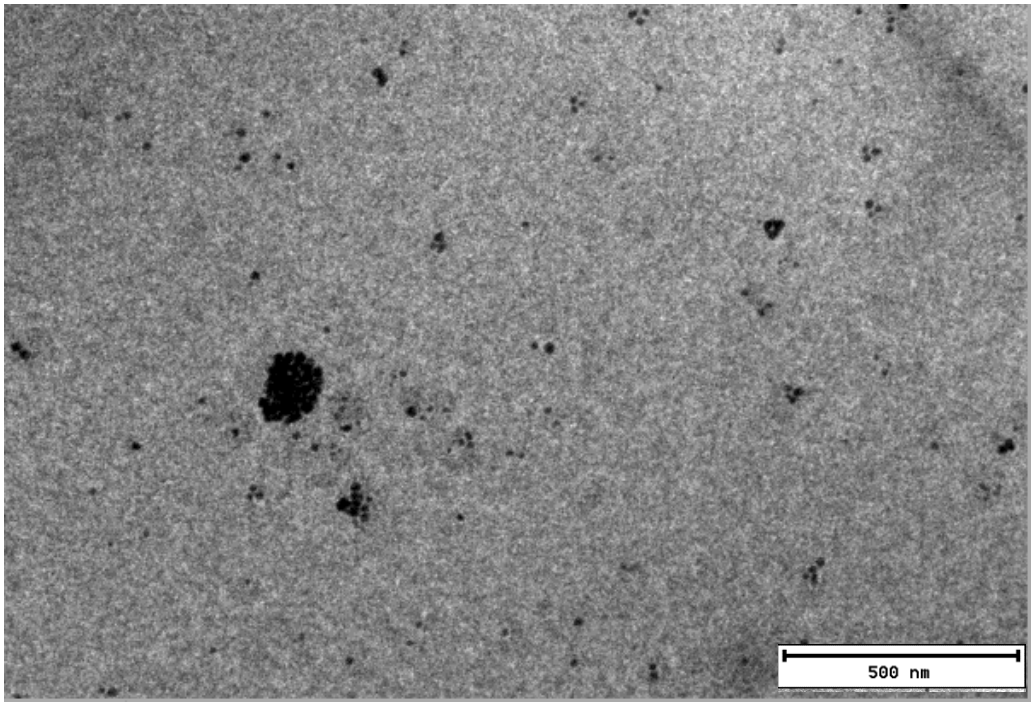

***Figure 7.2.3**: Cryo-TEM image identifying the spherical shape of the nanoparticle cluster.*

As discussed in Appendix A, in principle the appropriate equation to be used to analyse the neutron scattering data, should include not only the two form factors, accounting for isolated functionalized SPIONs and clusters, but also a structure factor arising from hard sphere interaction between the SPIONs composing the cluster. Each of these factors has to be multiplied by the corresponding volume fraction. Since the percentage of clusters with respect to the total number of particles present

in the suspension is very low (about 10%), the structure factor was neglected and the model only included the sum of the two form factors. The advantage of this simplification is that a smaller number of parameters has to be optimized during the fitting procedure.

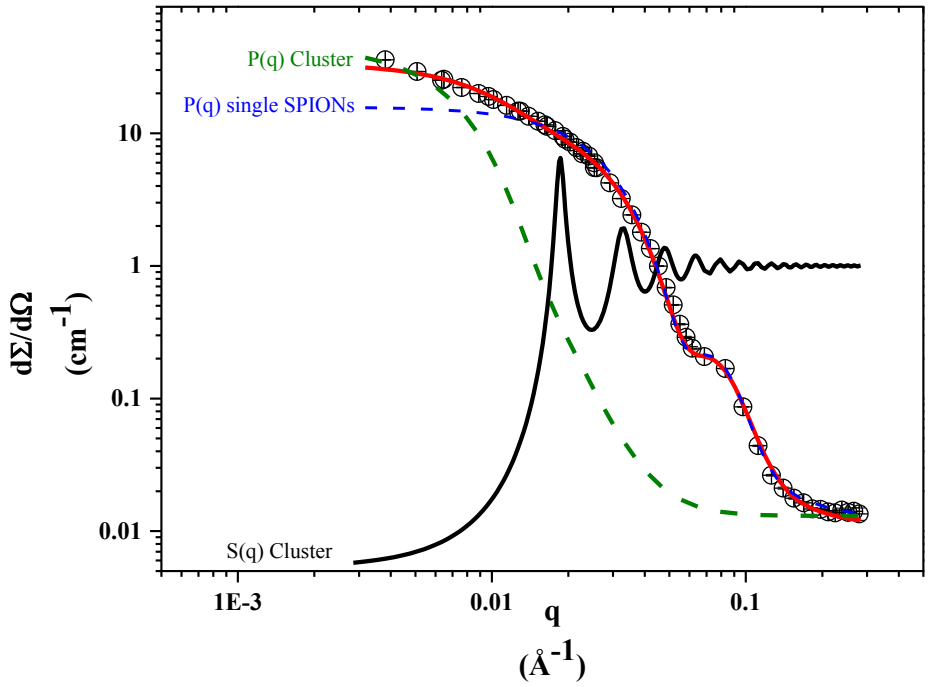

Figure 7.2.4: *SANS data collected for the 18LPC-ToThyCholRu/SPIONs together with the fitting curve (red) obtained by summing the cluster and the single SPIONs form factors. The cluster and single SPIONs form factor are also reported as separate curves (respectively dashed green and blu curves). The simulated structure factor for the SPIONs constituting the cluster is as well reported (black curve).*

In Figure 7.2.4 each of the separate contributions to the total scattered intensity were plotted together with the experimental data. Also plotted is, the structure factor calculated according to the size of the SPIONs with a high packing degree of the nanoparticles within the cluster (0.7 volume fraction), as suggested by the Cryo-TEM image. The structure factor predicts a correlation peak at q= 0.018 Å^{-1}, which clearly corresponds to a region where the cluster and the isolated SPION form factors give a stronger contribution to the scattered intensity. In order to make its features clearer, the structure factor reported in the graph was not multiplied by the volume fraction of the cluster within the suspension. In fact, if the cluster volume fraction is taken into account scattering intensity will become very low. Furthermore, if the nanoparticles in the cluster are somewhat disordered and/or their volume fraction is lower than assumed above, the peaks in *S(q)* drastically reduces. According to all these considerations, we concluded that the SANS data pattern was mostly governed by the cluster and isolated SPION form factors.

SANS data resulted to be extremely informative in the characterization of 18LPC-ToThyCholRu/SPIONs. Even if the amount of ToThyCholRu loaded on each SPIONs could not be determined, the optimization of scattering length density of the organic shell (ρ_{shell}) during the fitting of the experimental data, confirmed the presence of the ruthenium complex on the SPION surface. In fact, the value of $\rho_{organic\ shell}$ was about $9 \cdot 10^{-7}$ Å^{-2} for 18LPC/SPIONs and $2 \cdot 10^{-6}$ Å^{-2} for 18LPC-ToThyCholRu/SPIONs. The observed increment in ρ_{shell} is consistent with ToThyCholRu being present on SPION surface, since it has a larger scattering length density with respect to 18LPC.

7.3 In vitro bioscreenes of 18LPC-ToThyCholRu/SPIONs.

Bioscreens aimed at the evaluation of the cell survival index, performed by the research group of Prof. Carlo Irace (Dipartimento di Farmacia, Università di Napoli "Federico II", Naples, Italy), were parallel performed on 18LPC/SPIONs and 18LPC-ToThyCholRu/SPIONs (see also Appendix D). The presence of the amphiphilic ruthenium complex ToThyCholRu within the functionalized SPIONs formulation induced a significantly enhanced bioactivity; it provided a relevant concentration-dependent cytotoxic responses in the human cancer cells of different histological origin and endowed with high replicative potential *in vitro*. The obtained results are reported both in terms of concentration–effect bar graphs (Figure 7.3.1) and of IC_{50} values (Table 7.3.1). In the IC_{50} table, data concerning cisplatin (*c*DDP), known anticancer drug, are included for comparison, as a positive control for cytotoxic effects. As previously described, 18LPC-ToThyCholRu/SPION formulation contains only the 10% in moles of the active ruthenium complex with respect to the total lipid concentration. According to this nominal concentration, the results were normalized for the actual ruthenium complex amounts contained within the suspension (6, 10 and 20 μM, respectively). In terms of ToThyCholRu concentration, IC_{50} values are in the 10 to 20 μM range for human cancer cells, reflecting those recently reported for other amphiphilic ruthenium complexes included into liposomes with high antiproliferative activity *in vitro*.[123-127]

Subconfluent cultures cells were examined by phase-contrast light microscopy to support the relationship between cell viability and ruthenium-induced cytotoxicity. As shown in Figure 7.3.2, *in vitro* exposure to 18LPC/SPIONs did not cause substantial cytologic changes, whereas some morphological modifications of the cell monolayers clearly appeared after 18LPC-ToThyCholRu/SPIONs addition.

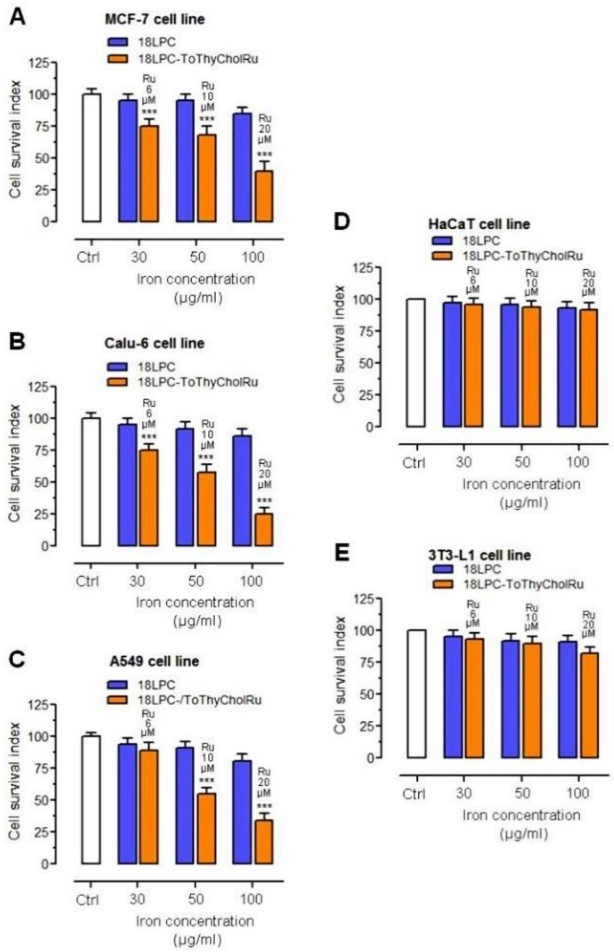

Figure 7.3.1: *Cell survival index, evaluated by the MTT assay and the live/dead cell ratio, for human breast adenocarcinoma MCF-7 cells (panel A), lung carcinoma Calu-6 (panel B) and A549 cells (panel C), and for human HaCaT keratinocytes (panel D) and murine 3T3-L1 fibroblasts (panel E) following 48 h of incubation with the indicated iron concentration (µg/ml) of 18LPC/SPIONs and of the ruthenium-containing 18LPC-ToThyCholRu/SPIONs, as indicated in the legend. In graphs, on bar tops the actual ruthenium amounts within functionalized 18LPC-ToThyCholRu/SPIONs are indicated. Data are expressed as percentage of untreated control cells and are reported as mean of five independent experiments.*

Table 7.3.1: *Comparison of the IC_{50} values (µM) relative to cisplatin (cDDP) and to the effective ruthenium concentration carried by 18LPC-ToThyCholRu/SPIONs in the indicated cell lines following 48 h of incubation.*

Cell lines	cDDP	18LPC-ToThyCholRu/ SPIONs
MCF-7	22 ± 4 µM	**17 ± 5 µM**
Calu-6	45 ± 5 µM	**12 ± 4 µM**
A549	36 ± 4 µM	**14 ± 5 µM**
HaCaT	272 ± 7 µM	**>100 µM**
3T3-L1	205 ± 6 µM	**>100 µM**

Microscopy images provided evidence that the reduction in cell viability is exclusively correlated to the presence of the active ruthenium complex and is thereby associated with well detectable dose-dependent cytotoxic effects.

18LPC/SPIONs were completely free of macroscopic biological effects on healthy cultured cells. On the other hand, 18LPC-ToThyCholRu/SPIONs showed relevant cytotoxicity selectively *versus* human cancer cells, thereby fully supporting their use as theranostic devices.

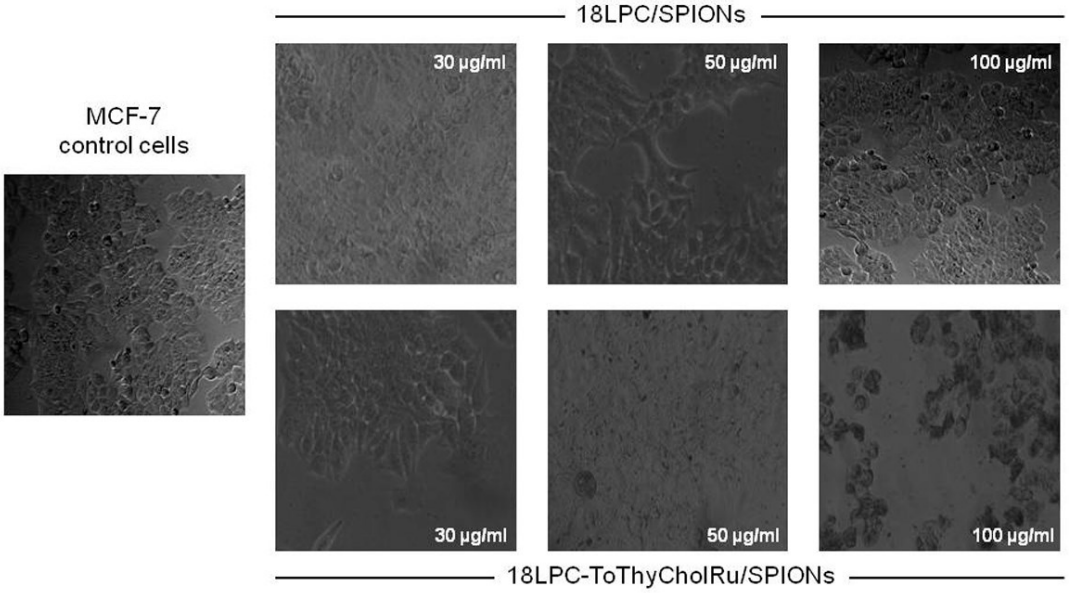

Figure 7.3.2: *Representative microphotographs at a 200 × magnification (20 × objective and a 10 × eyepiece) by phase-contrast light microscopy of MCF-7 cells lines untreated (control cells) or treated for 48 h with the indicated iron concentration of 18LPC/SPIONs (top line) and of 18LPC-ToThyCholRu/SPIONs (bottom line). For the latter, the corresponding ruthenium concentrations are 6, 10 and 20 µM, respectively. The shown images are representative of three independent experiments.*

7.4 Design of multimodal imaging contrast agents.

Multimodal imaging represents an innovative strategy in nanomedicine. It is based on the collection of images through the injection of nanodevices detectable by means of different diagnostic techniques. Among all, MRI/PET combined approach is a recently developed technique for the collection of images with high resolution and sensitivity.

As discussed in Chapter 1, PET is based on the conversion into an image of the radiation emitted by a radionuclide suitably administrated. The main advantage of this technique is its high sensitivity, i.e. nM concentration of radionuclides is sufficient for good quality data. However, PET is also known to be characterized by a very low spatial resolution. On the other hand, MRI has the advantage of

leading to anatomical information with a high resolution (< 0.1 cm), but it is also characterized by poor sensitivity. Thus, it is evident that PET and MRI are complementary techniques. [58]

Radionuclides for PET are usually administrated in form of a complex with a suitably designed chelator agents. Among the highly performing combination of radionuclides and chelators, ^{68}Ga complexed with NOTA was reported for its excellent *in vivo* stability. [54]

A modified NOTA molecule, named NOTA-ol, (Figure 7.4.1) was synthesized by the research group of prof. Daniela Montesarchio. NOTA-ol was obtained by conjugating the NOTA hexadentate chelator unit with an oleic acid molecule *via* amidic bond formation. NOTA-ol is characterized by an amphiphilic structure and, thus, present all the requirements for being anchored on the surface of the SPIONs.

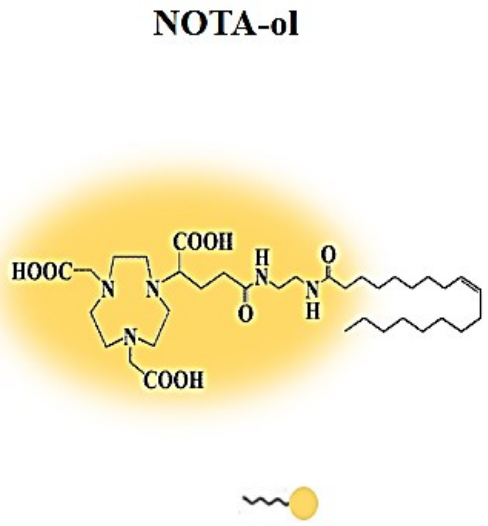

Figure 7.4.1: *Schematic representation of NOTA-ol structure as indicated in the picture. The yellow-highlighted region indicates the polar portion of the molecule.*

7.5 Structural characterization of 18LPC-[NOTA-ol]/SPIONs.

As for 18LPC-ToThyCholRu/SPIONs, the mixture of NOTA-ol and 18LPC, with molar ratio 10/90 and total concentration of $4 \cdot 10^{-3}$m, was used to prepare functionalized SPIONs, named hereafter 18LPC-[NOTA-ol]/SPIONs.

18LPC-[NOTA-ol]/SPION suspension was initially investigated by means of DLS measurements. The obtained hydrodynamic radius distribution is reported in Figure 7.5.1. A single broad population with mean hydrodynamic radius of about 20 nm was observed, larger than the typical size of the isolated functionalized SPIONs.

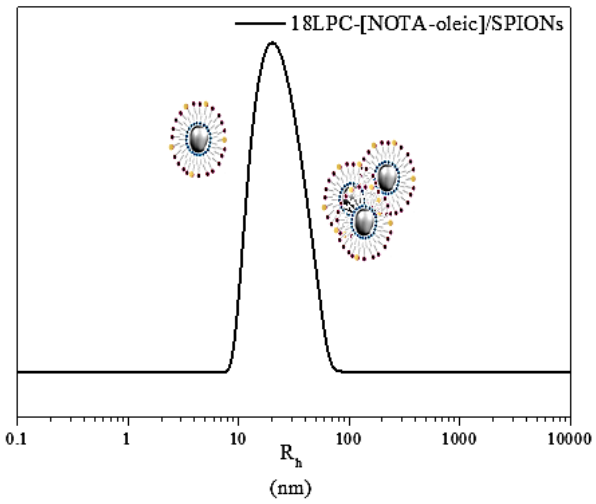

Figure 7.5.1: *Hydrodynamic radius distribution obtained for 18LPC-[NOTA-ol]/SPION suspension.*

Table 7.2.1: *Structural parameters obtained from DLS measurement for 18LPC-ToThyCholRu/SPION suspension.*

18LPC-[NOTA-ol]/SPIONs	
$D \cdot 10^6$ (cm^2s^{-1})	**R_h (nm)**
0.12 ± 0.01	11 ± 1

The interpretation of DLS data was supported by the analysis of SANS data. Indeed, as reported in Figure 7.5.2, a very good agreement with the experimental data was achieved with a fitting curve based on the same model used for 18LPC-ToThyCholRu/SPIONs with $\rho_{NOTA-ol}^{neutron} = 8.8 \cdot 10^{-7}\text{Å}^{-2}$. Thus, as reported in the equation 7.2.1 the scattered intensity was considered as the sum of the core-shell form factor and the spherical form factor, which respectively accounts for the isolated functionalized SPIONs and the clusters. The analysis of the SANS data was performed considering Schultz size distributions for the core radius and the shell thickness of the isolated functionalized SPIONs, as well as for the radius of clusters (equation 7.4.1).

As for ToThyCholRu, arguments based on steric hindrance associated with NOTA-ol polar region can be recalled in order to justify its less efficient SPIONs coating with respect to 18LPC. The optimized parameters estimated according to the adopted model for SANS data analysis are reported in Table 7.5.1.

By comparing the experimental data collected for the 18LPC-[NOTA-ol]/SPIONs with the one obtained for 18LPC-ToThyCholRu/SPIONs (Figure 7.2.2), it is evident a slightly different trend. This

difference has been ascribed to the higher size polydispersity of both the isolated functionalized SPIONs and clusters in 18LPC-[NOTA-ol]/SPION with respect to 18LPC-ToThyCholRu/SPION suspensions.

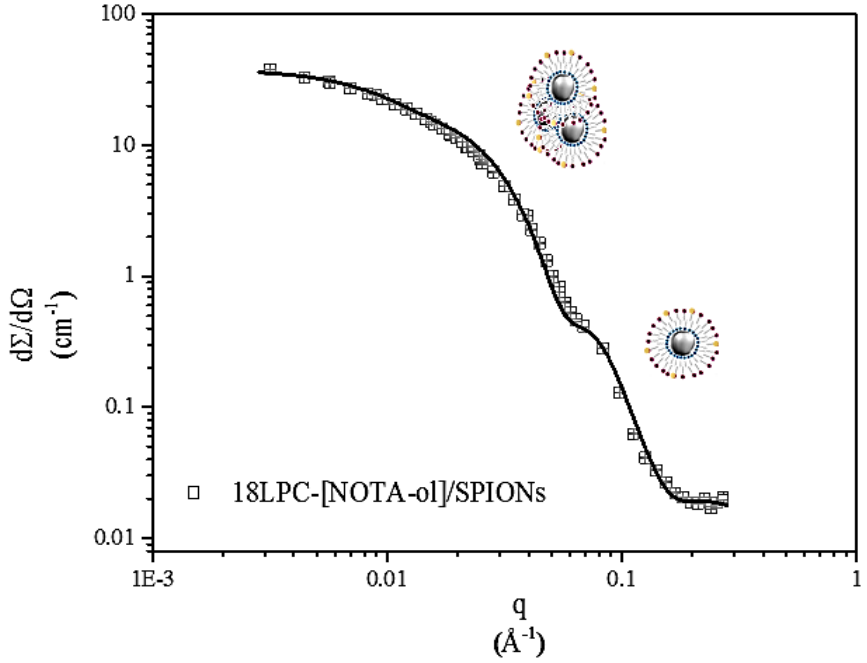

Figure 7.5.2: *SANS experimental data together with the corresponding fitting curve obtained for 18LPC-[NOTA-ol]/SPION suspension.*

Table 7.5.1: *Structural parameters obtained from SANS and DLS measurements for 18LPC-[NOTA-ol]/SPION suspension.*

18LPC-[NOTA-ol]/SPIONs					
r_{core} **(nm)**	p_{core}	r_{shell} **(nm)**	p_{shell}	$r_{cluster}$ **(nm)**	$p_{cluster}$
2.5 ± 0.5	0.41 ± 0.03	3.7 ± 0.1	0.34 ± 0.01	22 ± 2	0.55 ± 0.01

In the case of 18LPC-ToThyCholRu/SPION suspension the polydispersity indices were p_{core} = 0.25 ± 0.01, p_{shell} = 0.18 ± 0.02 and $p_{cluster}$ = 0.33 ± 0.02. On the other hand, in the case of 18LPC-[NOTA-ol]/SPIONs the polydispersity indices were p_{core} = 0.41 ± 0.03, p_{shell} = 0.34 ± 0.01 and $p_{cluster}$ = 0.55 ± 0.01.

The analysis SANS data indicated that in 18LPC-[NOTA-ol]/SPION suspension a large polydispersity is associated to the both the isolated functionalized SPIONs and the clusters. This result suggests that the systems cannot be described simply in terms of two populations in agreement with the collected DLS data. One possible hypothesis is that, SPIONs are organized within the suspension

in clusters with a broad size distribution. Nevertheless, further investigations are necessary to shed light on the structure of the suspension of 18LPC-[NOTA-ol]/SPION.

7.5 Developing Functionalized SPIONs for theranostics and multimodal imaging.

Recently great efforts of the scientific community were devoted to the development of nanodevices able to address different functionalities for diagnostic and therapeutic purposes. In this contest, the developed functionalization strategy was exploited to prepare different kind of functionalized SPIONs as prototypes of theranostic nanoparticles and multimodal imaging contrast agents.

The biocompatible coating provided by the 18LPC molecules was combined with the antiproliferative activity of ToThyCholRu in 18LPC-ToThyCholRu/SPIONs proposed as theranostic nanoparticles. The structural characterization carried out by means of DLS and SANS experiments confirmed that even if the formation of clusters was observed, ToThyCholRu and 18LPC were successfully introduced on the surface of the SPIONs. Because of the complex composition of the system, the validation of the presence of ToThyCholRu on the nanoparticle surface is an extremely relevant information. Furthermore, preliminary *in vitro* bioscreens demonstrated the potentiality of 18LPC-ToThyCholRu/SPIONs for cancer treatment.

On the other hand, 18LPC-[NOTA-ol]/SPIONs were designed as nanodevices for ^{68}Ga complexation aiming at their application for MRI/PET dualmode imaging. 18LPC-[NOTA-ol]/SPIONs were also characterized through the same combined DLS and SANS approach used for 18LPC-ToThyCholRu/SPIONs.

Even if a complete characterization of the proposed systems requires further investigations, we demonstrated the potentialities of the optimized functionalization strategy as indeed a suitable route to prepare not only functionalized SPIONs as MRI contrast agents, but also multifunctional nanoparticles. Thus, the collected data represent the grounds for the future development of promising theranostic and multimodal imaging nanoparticles.

Chapter 8 - *Conclusions*

8.1 A novel approach for the preparation of functionalized SPIONs

SuperParamagnetic Iron Oxide Nanoparticles (SPIONs) are characterized by peculiar magnetic properties that can be exploited in several technological fields. Among the proposed applications, SPIONs are effective contrast agents for Magnetic Resonance Imaging (MRI).

This Ph. D. project, SPIONs were synthesized through the thermal-decomposition method. Indeed, since the application of the iron oxide nanoparticles in biomedicine is strongly driven by their physical properties, it was mandatory to validate the synthesized nanoparticles as SPIONs.

Several techniques were combined to characterize the synthesized SPIONs and to verify their structure and composition.

The synthesized SPIONs can be dispersed only in non-polar solvents owing to the organic coating composed by oleic acid and olyelamine provided during the synthesis. Thus, a novel functionalization strategy based on hydrophobic interaction was developed and optimized to prepare stable aqueous suspensions of SPIONs with improved biocompatibility. The here introduced functionalization approach anchors a second amphiphilic layer on the organic coating of the synthesized SPIONs. The proposed strategy is of being a simple and one step approach, which can be easily extended to different kind of amphiphilic molecules and in principle also of inorganic nanoparticles.

8.2 Surfactant structure affect functionalized SPIONs size.

Different surfactants were used to prepare functionalized SPIONs, whose structure was deeply investigated through the combination of different scattering techniques. In particular, two lysophosphatidylcholines, 18LPC and 16LPC, as well as the cationic surfactant, CTAB, were chosen to decorate the surface of the SPIONs according to the optimized functionalization strategy. The three surfactants present different structure and consequently different aggregation properties. The Critical Micelle Concentration (CMC) was used as reference parameter to quantify how the structure of the surfactants affects their tendency to self-assemble.

The performed characterization highlighted that the self-aggregation properties of the surfactants have a strong impact on the efficiency in coating the surface of the SPIONs. In particular, the surfactant with the lowest CMC, 18LPC, was found to be the most efficient in guaranteeing an effective coating of the SPIONs, leading to a monodispersed aqueous suspension. On the other hand,

increasing the surfactant CMC by adopting 16LPC or CTAB, a larger amount of clusters was observed. Indeed, if the SPION surface is not suitably covered by the surfactant molecules, different nanoparticles tend to form aggregates, the clusters, in order to minimize the superficial energy. Interestingly, in the investigated system the formation of SPION clusters did not represent the first step of a precipitation process driven by uncontrolled nanoparticle aggregation. The clusters as well as the isolated functionalized SPIONs were stable in the aqueous suspensions.

The collected structural information constitute the grounds for the rational design of functionalized nanoparticles. As it is widely reported, the fate of the nanoparticles upon its administration to a living organism is influenced by their size. In this context, the performed physico-chemical characterization points at the optimized functionalization strategy as a suitable route to tune the size of the functionalized SPIONs by choosing the appropriate amphiphilic molecule.

Among the functionalized SPIONs, 18LPC/SPIONs represents a peculiar system being composed only by isolated functionalized SPIONs. Furthermore, it includes the biocompatible and reliable lysophosphatidylcholines molecules in the outer coating layer of the SPIONs. Hence, 18LPC/SPIONs have the potentialities to be suitably exploited for diagnostic purposes. Different kinds of experiments, *in vitro* and subsequently also *in vivo*, were carried out on 18LPC/SPIONs. The collected data indicated that the prepared functionalized SPIONs, were indeed able to affect the relaxation time of the water protons transversal being effective MRI negative contrast agents.

8.3 Interaction between functionalized SPIONs and lipid bilayers.

A continuously increasing number of inorganic and organic nanoparticles are proposed in the literature for biomedical applications. Even if several experiments concerning their biological activity are reported, only little information is available on the behavior of this kind of systems in a living organism. Clearly, the lack of information is due to the difficulty of investigating in details a complex system such as a living organism. However, in some cases it is possible to overcome this difficulty by choosing an appropriate model system.

Among the different biological components, the plasma cellular membrane certainly represents an important target for inorganic and organic nanoparticles. Thus, within this Ph. D. project a physico-chemical approach was established to investigate the interaction between lipid bilayers, mimicking the lipid portion of the plasma cellular membrane, and the functionalized SPIONs.

The obtained results can indeed be summarized as follows:

i) None of the tested functionalized SPIONs produced any substantial structural modification of the lipid bilayers ascribable to lipid removal or poration. Thus, it is

possible to conclude that the prepared functionalized SPIONs did not damage the investigated lipid bilayers.

ii) The SPIONs functionalized with both cationic and zwitterionic surfactant interacted with the lipid bilayers by means of superficial adsorption. In particular, the amount of stably adsorbed nanoparticles resulted to be strongly affected by the cholesterol content in the bilayers, i.e. a higher cholesterol concentration produced a larger amount of stably adsorbed SPIONs. We interpreted this evidence as ascribed to the structural properties exhibited by the lipid bilayers containing 30%w/w of cholesterol, i.e. high surface roughness.

iii) Some differences were observed in the case of 18LPC/SPIONs (zwitterionic surfactant-functionalized SPIONs) and CTAB/SPIONs (cationic surfactant-functionalized SPIONs). Even if in both cases a superficial interaction was observed, small variation of the structural parameters of the lipid bilayer were observed for CTAB/SPIONs. The presence of CTAB/SPIONs on bilayer surface produced a decrease of its thickness. On the other hand, no modifications of the bilayer structural parameters were observed in the case of 18LPC/SPIONs. This difference was ascribed to the positively charged surface of CTAB/SPIONs which induced a stronger interaction with the surface of the lipid bilayers.

8.4 Developing theranostic nanoparticles and multimodal imaging contrast agents.

On the grounds of the encouraging results obtained for SPIONs functionalized with zwitterionic surfactants, i.e 18LPC/SPIONs, the proposed functionalization strategy was used to prepare functionalized SPIONs for combined biomedical applications. SPIONs, besides the potential application of being MRI contrast agents, can represent nanocarriers for additional molecules with targeted functionalities. Specifically, the functionalization of SPIONs with potential drugs and probes for different imaging techniques has been recently reported. In the present case, we tested the functionalization strategy used to obtain 18LPC/SPIONs to prepare theranostic nanoparticles as well as dualmode PET/MRI contrast agents.

SPIONs were functionalized with the mixture of 18LPC and the amphiphilic ruthenium complex ToThyCholRu. The interest in this kind of nanoparticles is due to the antitumoral activity exhibited by ToThyCholRu, which makes 18LPC-ToThyCholRu/SPIONs potential theranostic nanoparticles. Indeed, ToThyCholRu was recently reported to be a promising antiproliferative drug, which was suitably included in liposomial aggregates and tested over different cancer cell lines. The preliminary

in vitro bioscreens highlighted 18LPC-ToThyCholRu/SPIONs as effective nanoparticle-based anticancer formulation.

SPIONs were also functionalized with the mixture composed by 18LPC and NOTA-ol, an amphiphilic chelating molecules for ^{68}Ga. NOTA is currently used for PET applications and, thus, 18LPC-[NOTA-ol]/SPIONs were designed as contrast agents for combined PET/MRI technique. The structural investigation of both 18LPC-ToThyCholRu/SPIONs and 18LPC/NOTA-ol/SPIONs confirmed that ToThyCholRu and NOTA-ol were effectively introduced on the surface of the SPIONs.

On the basis of the collected results, the optimized functionalization strategy was validated as indeed suitable for the preparation of multifunctional nanoparticles.

8.5 Final remarks and perspectives.

The here presented Ph. D. project was based on the challenging objective of exploiting the aggregation properties of the amphiphilic molecules and the solid knowledge on their self-assembly behavior, to prepare functionalized SPIONs for biomedical application as MRI contrast agents. The major features of the carried out work were the collection of fundamental information on SPIONs physico-chemical properties and the rational establishment of a strategy based on hydrophobic interaction suitable to stabilize the inorganic nanoparticles in water media.

The identification of a preparation protocol is partially a trial-and-error process, which leads to a deeper and deeper understanding the each attempt. Among the results of the present work, there was the actual development of a functionalization strategy and the rationalization of the collected results in a specific relation between the surfactant aggregation properties and the structural characteristics of the prepared functionalized SPIONs. In order to achieve these results, two different scientific worlds were interdigitated: the world of chemical synthesis and the world of physical chemistry.

In addition, a significant portion of this Ph. D. project was also devoted to enlarging the characterization of the prepared functionalized SPIONs by exploring their interaction with lipid bilayers mimicking of the plasma cellular membrane. The aim of this study was the achievement of an insight at the molecular level on their potential behavior toward biological systems.

On the grounds of the discussed results, the perspectives of the research project, of which this Ph. D. thesis is a part, are mainly distributed along two different directions. On one hand, the extension of the functionalization strategy to the effective preparation of functionalized SPIONs for theranostics or multimodal imaging (in particular, a further characterization of the here presented prototypes and also a redesign of both the potential antitumoral drug and the NOTA-modified molecule are possibly

required). On the other hand, the interaction of the functionalized SPIONs with other biological relevant systems, such as serum proteins, should be pursued in order to expand the information about potential *in vivo* behavior of SPIONs.

Appedix A - *Scattering Techniques*

A.1 Introduction.

The Scattering techniques are powerful tools to have information about the structure and the dynamics of matter on the microscopic level. The greatest advantage of these techniques is that they are non-invasive and possibly non-destructive.[1]

A scattering experiment can be described as a plane wave with a defined intensity, wavelength and direction, incoming on the sample. As a consequence of the interaction between the sample and the incident plane wave, a secondary spherical wave, also referred to as the scattered wave, is emitted. Under the condition of revealing the scattered wave at large distance from the sample, this latter can be described as well as a plane wave. The analysis of the scattered wave energy and intensity gives information respectively about the dynamics and the structure of the sample.

Equation A.1 is the most general equation related to a scattering experiment.

$$I \approx \frac{d\sigma}{d\Omega} = b^2 \tag{A.1}$$

The scattered intensity, I, is proportional to the differential scattering cross section ($\frac{d\sigma}{d\Omega}$), where Ω is the scattering solid angle. The differential scattering cross section can be regarded as the probability that the incident wave is scattered by the sample within a certain solid angle. This probability is proportional to a real number, which is the square of the scattering length (b). The scattering length is the parameter that quantifies the interaction between the incoming wave and the sample, and thus its value depends upon the nature of the wave and the composition of the sample.

Most of the scattering techniques are based on the use of visible light, X-rays and neutrons. Visible light and X-rays are both interacting with the electrons present within the sample. In particular, in the case of the X-rays, the incident wave is directly scattered from the electrons and b is dependent on both the atomic number and the atomic structure factor of the atoms composing the sample (a more detailed discussion of the atomic structure factor is reported in the following paragraph). On the other hand, the interaction between the visible light and the sample (also simply known as light scattering)

[1] *For radiations with high energy and intensity, limits in the exposition time must be taken into account in order to avoid sample damage in the case of biological systems.*

involves the generation of an oscillating induced dipole moment, which is the secondary source emitting the scattered wave and is proportional to the polarizability. Thus, in the case of light scattering, *b* is related to the polarizability of the sample. The differences between the light and the X-rays with respect to their interaction with matter can be mostly ascribed to their wavelengths. Indeed, while typical wavelengths of visible light are of hundreds of nm, typically used X-ray wavelengths correspond to a few Å. It is worth to note that, since the time-scale and length, on which the sample can be probed, during a scattering experiment, are determined by the energy of the incident wave, light scattering and X-ray scattering can be used to probe the dynamics and the structure of matter at very different levels.

Neutrons are no longer scattered by the electrons, but instead they interact with the nuclei. Thus, *b* will be determined by the nature of the nuclei that compose the sample, i.e. different isotopes of the same element will have different scattering length values. Even if the interaction with matter is completely different, neutrons and X-rays have very similar wavelengths. Neutron and X-ray scattering might represent complementary techniques to study the structure of the sample.

This Appendix is focused on the use of X-ray and neutron scattering to characterize the structure of the investigated sample. A brief treatment of the light scattering is reported in the Appendix C. A complete and detailed discussion of the scattering theory and its application can be found in the references [128, 129]. In order to present the scattering theory with a general approach, valid for X-rays neutrons and visible light, the sample will be considered as composed by an ensemble of scatterers. The scatterers will represent the sample components responsible for the interaction with the incoming wave. In case, of X-rays and visible light the scatterers are the electrons. In case of neutrons the scatterers are the nuclei.

A.2 Basics of scattering theory.

In this paragraph some of the basic concepts concerning scattering theory will be reported with a general formalism valid for light, X-ray and neutrons. Even if they have been developed as separate techniques, the fundamental equations of light, X-ray and neutron scattering are the same.

Two different scattering events can be distinguished if the direction and the energy of the scattered wave are simultaneously analyzed. The inelastic scattering occurs when the scattered wave has a different energy with respect to the incident one. On the other hand, during the elastic scattering no energy transfer between the incident wave and the sample is detected.

Limiting the discussion to the case of the elastic scattering, the angular dependence of the scattered intensity can be expressed in terms of the scattering vector q, indicated also as transferred momentum, and defined in equation A.2.

$$q = \frac{4\pi n}{\lambda}\sin\theta \qquad \text{(A.2)}$$

In equation A.2, n is refractive index of the sample. In case of X-rays and neutrons, the dependence of q on n can be neglected, since this latter is very close to the unit.

The expression of q can be easily derived from geometrical consideration about the scattering experiment (Figure A.1).

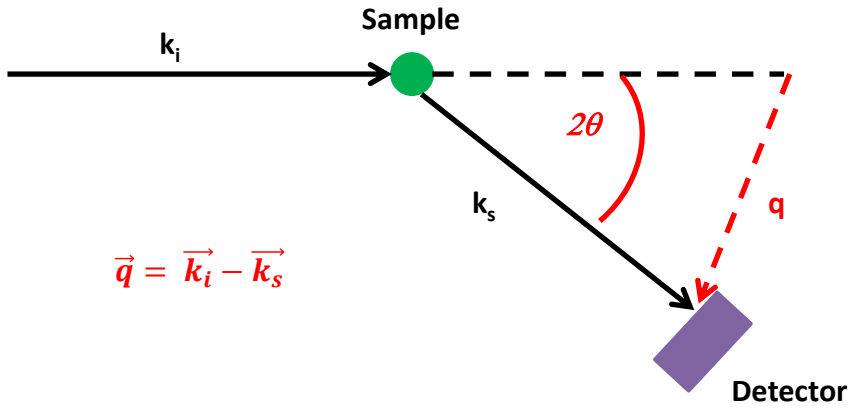

Figure A.1: *Schematic representation of a scattering experiment leading to the definition of the scattering vector q.*

The incident wave is characterized by the momentum k_i, defining the propagation direction of the wave, with modulus of $\frac{2\pi}{\lambda_i}$, where λ_i is the incident wavelength. Analogously, the scattered wave reaching the detector is characterized by the momentum k_f, with modulus $\frac{2\pi}{\lambda_f}$, where λ_f is the scattered wavelenght. If the incident wave is elastically scattered by the sample, $\lambda_f = \lambda_i$, the incident and the scattered wave will have the same momentum modulus. Under this condition, the transferred momentum will only depend on the change of direction of the scattered wave with respect to the direction of the incoming wave.

As already mentioned in the previous paragraph, the sample can be treated as an ensemble of scatterers. Thus, the detected wave is the sum of the scattered waves emitted by each scatterer.

According to the Born approximation, the scattered amplitudes can be regarded as perturbation of the incoming wave amplitude, as reported in equation A.3.

$$A(q) = A_0 \sum_{i=1}^{N} b_i e^{-i\vec{q}\cdot\vec{r_i}} \tag{A.3}$$

Where A_0 is the amplitude of the incident wave, b_i and r_i are respectively the scattering length and the position of the scatterer i. The scattering length depends on the nature of the used incident wave as well as of the scatterers. Equation A.3 can be rewritten in a continuous notation as in the equation A.4.

$$A(\vec{q}) = A_0 \int_V n(\vec{r}) e^{-i\vec{q}\cdot\vec{r}} d\vec{r} \tag{A.4}$$

The volume, which is considered in the integral of equation A.4, is the illuminated volume, which is the portion of the sample illuminated by the incident wave. The sum in equation A.3 is thus substituted by the integral of the function $n(r)$, which is the spatial density of the scatterers.

The fundamental result contained in equation A.4 is that the scattered amplitude is related to the Fourier transform of the scatterer spatial density. This means that, in principle, the spatial distribution of the scatterers composing the sample could be achieved by measuring the scattered amplitude by simply applying the inverse Fourier transform. In particular, by performing an X-ray or neutron scattering experiment, the electron density map or the exact position of all the nuclei in the sample could be directly obtained. Unfortunately, things are not so simple. It has to be considered that, in the Fourier transform expression, the integration limits are -∞ and +∞, but it is evident that, during a scattering experiment, data concerning a finite volume are the only one accessible. Furthermore, the quantity that is actually measured during a scattering experiment is the scattered intensity and not the scattered amplitude. Fortunately, theoretical and experimental approaches are available to solve these issues.

The scattered intensity is proportional to the scattering cross section and related to the square modulus of the scattered amplitude (equation A.5).

$$I(\vec{q}) \propto \frac{d\Sigma}{d\Omega} = |A(\vec{q})|^2 = \left| A_0 \int_V n(\vec{r}) e^{-i\vec{q}\cdot\vec{r}} d\vec{r} \right|^2 \tag{A.5}$$

It is worth to note that the equation A.5 was obtained within the kinematic approximation. In particular, some assumptions were made in describing the scattering event: i) the sample was considered as composed by an ensemble of scatterers which occupy fixed position in space; ii) the interaction between the sample and the incoming wave was assumed to be very weak, so that most of it is transmitted and only a small fraction is scattered; iii) no energy transfer occurs between the

scatterers and the incoming wave, which is scattered coherently (a phase relation exists between the waves scattered by different point of the sample). However, in a real experiment the atoms in the sample, which are responsible for the scattering event, do not occupy fixed positions. Equation A.5 can be still used if *r* is considered as the average position at thermal equilibrium. Furthermore, the experimenter has to be very careful in treating the collected data and subtract, as part of background, all the contributions that are not originated from the elastic and coherent scattering.

Taking into account all these considerations about equation A.5, equation A.6 is obtained if the square of the scattered amplitude modulus is expressed.

$$I(\vec{Q}) \quad d\Omega \quad \int_V \rho(\vec{r}) e^{-i\vec{Q}\cdot\vec{r}} \int_V \rho(\vec{r}) e^{i\vec{Q}\cdot\vec{r}} \tag{A.6}$$

Where $\rho(\vec{r})$ is the product of the scattering length and the spatial density of the scatters and, thus, represents the scattering length density. Equation A.6 can be rearranged according to equation A.7, where the change of variable $r' = r + R$ was taken into account.

$$I(\vec{Q}) \quad d\Omega \quad \int_V \rho(\vec{r}) \rho(\vec{r}+\vec{R}) e^{-i\vec{Q}\cdot\vec{R}} \tag{A.7}$$

From equation A.7, the pair correlation function *P(R)*, also known in crystallography as Patterson function, can be defined as in equation A.8.

$$P(\vec{R}) = \int_V \rho(\vec{r}) \rho(\vec{r}+\vec{R}) dr \tag{A.8}$$

The pair correlation function correlates the probability that the incident wave is scattered at the position *r* with the probability that the same wave is scattered at the position *r* + *R*. Clearly, this probability depends on how the scatterers are distributed in space, and thus P(R) is function of the relative distances of the scatterers within the sample. Equation A.8 can also be rewritten substituting $\rho^*(r)$ with $\rho(r)$. This substitution can be done since the complex part of the scattering length density is connected with the absorption of the incident wave by the scatterers, which, at least for neutrons and X-rays, is usually very low.

By comparing equation A.5 and A.7 it is possible to conclude that while the scattered amplitude can be connected by Fourier transform to a function of the absolute position of the scatterers, the scattered intensity can only be Fourier transformed in a function of the relative position of the scatterers.

The description of the scattering phenomenon was carried out by directly introducing the scattered amplitude expression as equal to the incident amplitude times a factor introducing the incident wave perturbation produced by the sample.

In the case of neutron scattering, from a quantum mechanics point of view the scattered wave can be obtained by solving the Schroedinger equation (equation A.9).

$$-\frac{h^2}{8\pi^2 m}\nabla^2\psi(r)+V(r)\psi(r)=E\psi(r) \qquad (A.9)$$

Where h is Plank constant, $\psi(r)$ is the neutron wave function and E is the neutron energy.

The expression of the scattered wave and its energy are estimated by considering, in the eigenvalue equation, the interaction potential V. In the case of neutron scattering the derivation of this potential is not simple, since the interaction between the neutrons and nuclei involves nuclear forces, which have not been yet fully described. Most of the theory on neutron scattering has been developed on the base of the *pseudo*-potential introduced by Fermi (equation A.10).

$$V=\frac{h^2}{2\pi m}\rho \qquad (A.10)$$

The *pseudo*-potential includes the scattering length density, quantifying the interaction between neutrons and nuclei. It is worth to underline that the neutron scattering length densities for the different nuclei are obtained experimentally.

A.3 X-ray and neutron scattering.

In the previous discussion, the equations describing the intensity scattered by a sample were illustrated without distinguishing neutron or X-ray scattering. As already highlighted, the difference between the two techniques is in the meaning of the scattering length b.

X-rays are electromagnetic radiation with wavelengths in the range of 10^{-2}-10^{2} Å. However, the typical wavelengths used to investigate the matter are in the rage of 0.5-2.5 Å. The X-ray beam used for a scattering experiment can be the K_α radiation from a copper target tube or a molybdenum target tube. Alternatively, X-rays with well-defined wavelength can also be selected by means of a monochromator from the broad spectrum emitted by a synchrotron radiation source.

For an isolated electron interacting with unpolarized X-rays, the expression of its scattering length (b_e) is given by the *Thomson Formula* (equation A.11).

$$b_e=r_e\left(\frac{1+\cos^2 2\theta}{2}\right)^{1/2} \qquad (A.11)$$

Where r_e is $\frac{e^2}{mc^2}$ with e and m being respectively the electron charge and mass, while c is the light speed constant. For an atom containing Z electrons, the scattered amplitude is given by equation A.12.[2]

$$A(\vec{q}) = -b_e \sum_{i=1}^{Z} e^{-i\vec{q}\cdot\vec{r}_i} \tag{A.12}$$

In equation A.12, the term b_e is taken out of the sum sign, since it is equal for all the electrons. Upon substitution of the sum with the integral, we can now define the structure atomic factor as in equation A.13, which does depend on the spatial coordinate of the electrons within a certain atom. This means that each atom is characterized by its atomic structure factor. *F(q)* values are tabulated and they are obtained from theoretical calculations. It is worth to note from the expression of the atomic structure factor that its value depends on the wavelength of the incoming X-ray beam.

$$F(\vec{q}) = \int_{V_{atom}} \rho(\vec{r}) e^{-i\vec{q}\cdot\vec{r}} d\vec{r} \tag{A.13}$$

A real sample is composed by several atoms possibly of different elements. Thus, the expression of the scattered amplitude can be written as in equation A.14.

$$A(\vec{q}) = -b_e \int_{V} \rho(\vec{r}) F(\vec{q}) e^{-i\vec{q}\cdot\vec{r}} d\vec{r} \tag{A.14}$$

By comparing equation A.12 with the equation A.14 the scattering length for X-rays is evidently the product of the electron constant b_e and the atomic structure factor of all the atoms present in the sample.

As underlined in the beginning of this discussion, only the elastic scattering was considered, which, in the case of X-rays, represents the strongest component. However, X-rays can indeed transfer a small amount of energy to the electrons. This phenomenon is known as Compton-modified scattering. Experiments, devoted at determining the sample structure, are based on elastic scattering detection. The Compton-modified scattering is treated as part of the measurement background.

Neutrons are non-charged particles having mass of $1.675 \cdot 10^{-27}$ kg, spin of ½ and a magnetic moment of -1.9132 nuclear magnetons. Owing to their spin and magnetic moment, neutrons can interact in two different ways with the nuclei composing the sample, giving rise to the nuclear and magnetic scattering. The nuclear scattering involves complex nuclear interactions between the spin states and the magnetic moments of the interacting nucleus and the neutrons. For this reason, a general trend of

[2] *The X-ray scattering from the nucleus can be neglected due to the large difference of mass.*

the atomic ability to scatter neutrons cannot be identified through the periodic table. On the other hand, the X-rays scattering ability can be easily correlated to the atomic number. In addition, neutrons are differently scattered from isotopes of a same element, since they present different nuclear properties.

The magnetic scattering is associated to magnetic samples and it is due to the interaction between the magnetic moments of unpaired electrons spins and nuclear magnetic moment of neutrons. In principle, also X-rays can be magnetically scattered from a magnetic sample because of the interaction between the magnetic field associated to the X-rays and the electron orbital magnetic moments. However, X-ray magnetic scattering is very weak.

Neutrons can be produced in nuclear reactors from chain reactions involving ^{235}U fission. Spallation sources, where accelerated protons or electrons hit a heavy nucleus, can be as well exploited for neutrons production. In both type of sources, neutrons are obtained with a very high energy (hot neutrons) and need to be thermalized in order to be used for the scattering experiments. Thus, the produced neutrons are scattered by a moderator, which is composed by light nuclei. The inelastic collisions between the neutrons and moderator atoms reduce the neutron energy. If the moderator is enough large, the equilibrium condition at the moderator temperature for the produced neutrons might be approximately achieved. Hence, the energy and wavelengths of the neutrons can be controlled by setting the moderator temperature. The relation between neutron wavelength and the temperature is reported in equation A.15:

$$\frac{h^2}{2m\lambda} = K_B T \tag{A.15}$$

Where K_B is the Boltzmann constant, h is the Planck constant and m is neutron mass.

According to their temperature, neutrons can be classified in hot, thermal or cold neutrons. Among them, thermal neutrons are characterized by energy corresponding to about 20 meV. If this energy value is converted in terms of wavelength, by applying equation A.15, it can be shown that thermal neutrons have typical wavelength value close to X-rays, but way much less energy. Typical energy of X-rays used for scattering experiment is of about 10 keV. Hence, at the same wavelength, X-rays are characterized by a sensibly higher energy than neutrons.

The energies associated to atomic motions arising from vibrations, rotations and translations in solid and liquids are similar to the typical energies of the thermal neutrons. Thus, thermal neutrons are an effective probe for both the structure and the dynamics of the sample under investigation. Furthermore, neutron scattering is particularly suitable for the characterization of biological systems, since the high energy associated to X-rays might cause sample damage, unless short-time exposure are used.

The interaction between neutrons and nuclei is quantified by the neutron scattering length b_n. The values of b_n are tabulated for the different isotopes and are experimentally obtained. In case of neutron scattering, the scattered amplitude can be expressed according to equation A.16.

$$A(\vec{q}) = A_0 \int_V b_n \rho(\vec{r}) e^{-i\vec{q}\cdot\vec{r}} d\vec{r} \tag{A.16}$$

Since b_n is different for different nuclei we have to consider b_n distribution over the illuminated volume. In equation A.17 the sum of the scattering lengths is averaged over the illuminated volume.

$$A(\vec{q}) = A_0 \sum_{i=1}^{N} \langle b_{n_i} \rangle e^{-i\vec{q}\cdot\vec{r}} \tag{A.17}$$

During scattering experiments, the measured quantity, the scattered intensity, is proportional to the square of the scattered amplitude (equation A.18)

$$I(\vec{q}) = \frac{d\sigma}{d\Omega} = \sum_{i,j}^{N} \langle b_{n_i} \cdot b_{n_j} \rangle e^{-i\vec{q}\cdot(\vec{r}_i - \vec{r}_j)} \tag{A.18}$$

The complex component of the neutron scattering length is neglected since the neutron absorption from the nuclei has a very low probability with the exception of a few nuclei, i. e. gadolinium or cadmium. Equation A.18 leads to equation A.19, if the terms referring to equal nuclei (i=j) and different nuclei (i≠j) are separately taken into account.

$$I(\vec{q}) = \frac{d\sigma}{d\Omega} = N \langle b_n^2 \rangle + \sum_{i \neq j}^{N} \langle b_{n_i} \cdot b_{n_j} \rangle e^{-i\vec{q}\cdot(\vec{r}_i - \vec{r}_j)} \tag{A.19}$$

Since the scattering lengths of two different nuclei in two different position are not correlated with each other, it is possible to replace $\langle b_{n_i} \cdot b_{n_j} \rangle$ with $\langle b_{n_i} \rangle \cdot \langle b_{n_j} \rangle$ (equation A.20).

$$I(\vec{q}) = \frac{d\sigma}{d\Omega} = N \langle b_n^2 \rangle + \sum_{i \neq j}^{N} \langle b_{n_i} \rangle \cdot \langle b_{n_j} \rangle e^{-i\vec{q}\cdot(\vec{r}_i - \vec{r}_j)} \tag{A.20}$$

$$I(\vec{q}) = \frac{d\sigma}{d\Omega} = N \langle b_n^2 \rangle + \langle b_n \rangle^2 \sum_{i \neq j}^{N} e^{-i\vec{q}\cdot(\vec{r}_i - \vec{r}_j)} \tag{A.21}$$

The addition and subtraction of term for i=j in equation A.20 leads to equation A.22.

$$I(\vec{q}) = \frac{d\sigma}{d\Omega} = N \left[\langle b_n^2 \rangle - \langle b_n \rangle^2 \right] + A_0^2 \langle b_n \rangle^2 \sum_{i,j}^{N} e^{-i\vec{q}\cdot(\vec{r}_i - \vec{r}_j)} \tag{A.22}$$

Equation A.22 is composed by two terms. The first term depends on the mean value of the scattering length, and takes into account the relative position of the nuclei within the sample. This term represents the coherent component of the scattered intensity, which leads to structural information

about the sample. On the other hand, the second term of equation A.22 depends on the difference in scattering length due to the inhomogeneity of the sample, i.e. nuclei of different element or different isotopes. This term takes into account the random fluctuations of the scattering length over the illuminated volume and it is the incoherent component of the scattered intensity, since the neutrons scattered by different nuclei lose their phase relation. The different interactions between neutrons ad nuclei of the same isotopes, but in different spin states, also contributes to the incoherent scattering, since there is no correlation between nuclei positions and their spin states. In particular, hydrogen interacts very differently with neutrons depending on its spin states and, thus, has a very intense incoherent scattering. On the other hand, deuterium is responsible for a rather irrelevant incoherent scattering.

In equation A.22, the incoherent term is simply a constant, which does not depend on q (if no time dependence of the nuclear position is taken into account). It is worth to note that during inelastic scattering experiments, the coherent and incoherent terms lead to very different information about the dynamics of the sample. Indeed, the coherent term depends on the relative movements of the nuclei within the sample, while from the incoherent term the dynamic of An isolated specie can be studied. During elastic scattering experiments, the incoherent scattering represents a background that has to be removed. In soft matter, substitution of hydrogen with deuterium, is a common approach to reduce the measurement background and eventually highlight specific part of the sample.

A.4 Small Angle X-ray and Neutron Scattering.

By combing the definition of q with the Bragg law (equation A.23), the scattering vector is demonstrated to be inversely proportional to the characteristic length of the sample d.

$$\lambda = 2d\sin(\vartheta) \quad \text{(A.23)}$$

Hence, large-scale structures within the sample require very small values of q for their exploration. Conversely, small distances are observed in the large-q range. This result is fundamental in order to identify the appropriate technique, according to the length scale of interest, which has to be used to gain structural information about the sample. The q-range suitable to characterize structures of sizes of about 10 Å or lager is usually considered as corresponding to small angle. Thus, the scattering techniques associate to this kind of characterization are named after the employed q-range as Small Angle Scattering (SAS).

SAS experiments often aim to investigate the shape and the size of particles dispersed in a homogenous matrix. The particles under investigation can be macromolecules, such as proteins or

polymer chains, but they can also be aggregates of different molecular units or inorganic nanoparticles. In order to observe neutron scattering in the small-angle region, the system must present fluctuations of the scattering length density. Thus, the condition in which different microscopic regions of the sample contribute to the scattered amplitude with different scattering length densities must be achieved. This concept is mathematically expressed in the equation A.24.

$$I(\vec{q}) = \frac{d\Sigma}{d\Omega}(q) = (\rho_1 - \rho_0)^2 \int_V e^{-i\vec{q}\cdot\vec{r}}\,d\vec{r} \int_V e^{i\vec{q}\cdot\vec{r}}\,d\vec{r} \tag{A.24}$$

The scattered intensity depends only on the difference of the scattering lengths but not directly on the specific value of the scattering length of the particle (b_1) and the matrix (b_0). Thus, for example, in Small Angle Neutron Scattering (SANS) similar curves are collected if a deuterated molecule is dispersed in a hydrogenated solvent or the same hydrogenated molecule is dispersed in the deuterated solvent. The only difference that can be observed is in the background, since the system containing the hydrogenated solvent will produce a higher incoherent scattering. For this reason, usually, SANS measurement are performed with deuterated solvents.

The difference of the scattering length densities is also indicated as contrast. The contrast match, available within SANS experiments, is based on the possibility of suitable mixing hydrogenated and deuterated solvents to mask a defined portion of the dispersed particles, and thus obtain structural information on a specific part of the system.

Equation A.24 can be rewritten in a discrete form separating the term arising from the same particle from the ones corresponding to different particles, as reported in equation A.25 and A.26. The scattered intensity is normalized by the sample volume. In equation A.25 and A.26 R_{ij} is the distance between distinct positions within the same particle or between different particles

$$\frac{1}{V}\frac{d\Sigma}{d\Omega}(\vec{q}) = (b_1 - b_0)^2 \frac{1}{V}\left[N\sum_{i_1 \neq j_1}^{z} e^{-i\vec{q}\cdot\vec{r}_{i_1 j_1}} + N^2 \sum_{i_1 \neq j_2}^{z} e^{-i\vec{q}\cdot\vec{r}_{i_1 j_2}} \right] \tag{A.25}$$

$$\frac{1}{V}\frac{d\Sigma}{d\Omega}(\vec{q}) = (b_1 - b_0)^2 \frac{1}{V}\left[\left(N\sum_{i_1 \neq j_1}^{z_1} e^{-i\vec{q}\cdot\vec{r}_{i_1 j_1}} \right) \cdot \left(\frac{1}{2}\left(1 + N\sum_{i_1 \neq j_2}^{z_{1,2}} e^{-i\vec{q}\cdot\vec{r}_{i_1 j_2}} \right) \right)^2 \right] \tag{A.26}$$

In equation A.25, *N* particles each one composed by *z* scattering units were considered. The first term in equation depends on the internal structure of each particle, while the second term depends on the spatial correlation existing between different particles.

We can now define the form factor *P(q)* [3] and the structure factor *S(q)* as in equations A.27 and A.28, that will lead to express the scattered intensity as in equation A.29.

$$P(\vec{q}) = \frac{1}{z^2}\left(N\sum_{i_1 \neq j_1}^{z_1} e^{-i\vec{q}\cdot(\vec{r}_{i_1}-\vec{r}_{j_1})} \right) \tag{A.27}$$

$$S(\vec{q}) = \frac{1}{z^2}\left(1 + N\sum_{i_1 \neq j_2}^{z_{1,2}} e^{-i\vec{q}\cdot(\vec{r}_{i_1}-\vec{r}_{j_2})} \right) \tag{A.28}$$

$$\frac{1}{V}\frac{dI(\vec{q})}{d\Omega} = (b_1 - b_0)^2 \frac{1}{V}\left[P(\vec{q})\cdot S(\vec{q}) \right] \tag{A.29}$$

Both the form factor and the structure factor are normalized to 1 for q=0 by the factor $1/z^2$.
Using the integral notation, the scattered intensity can be expressed as in equation A.30.

$$\frac{1}{V}\frac{dI(\vec{q})}{d\Omega} = (\rho_1 - \rho_0)^2 V_1 \varphi \left[P(\vec{q}) + N S(\vec{q}) \right] \tag{A.30}$$

Where the volume fraction $\varphi = \frac{NV_1}{V}$ was taken into account.

If the sample under investigation is considered as composed by a dilute suspension of particles, such that the interparticle interactions are neglectable, the structure factor will be equal to 1. In case no correlation distances between the scattering particles can be identified, and the scattered intensity depends only on the form factor (equation A.31). Thus, the pattern of the collected experimental data will be diagnostic of the shape and the size of the particles composing the sample. The previously described situation is not so unusual during SAS experiment. Indeed, the sample is often prepared with the appropriate composition that will avoid interparticle interaction, or different concentrations are explored in order to separately study the effect of the form factor and the structure factor.

$$\frac{1}{V}\frac{dI(\vec{q})}{d\Omega} = (\rho_1 - \rho_0)^2 V_1 \varphi P(\vec{q}) \tag{A.31}$$

As already discussed in the previous section, the structural information about the sample cannot be obtained directly from the collected data. The approach used in SAS to solve this ancestral problem is based on the use of model functions. Indeed, the scattered intensity can always be calculated from the knowledge of the structure of the sample, but the reverse is not true. Thus, if the particle shape is known on from independent experiments, or it is reasonably hypothesized on the base of chemical consideration, the corresponding model function can be compared to the experimental data. Once the

[3] *In SANS equation the form factor is usually indicated as P(q). The used symbolism should not be confused with the Patterson function also indicated with P.*

appropriate model function is identified, the structural parameters can be optimized to give the best agreement with the experimental data.

In the case of spherical particles, a simple analytical expression of the form factor can be calculated. The scattered intensity arising from a spherical particle, owing to its high symmetry, does not depend on the particle orientation. Thus, the form factor can be expressed according to equation A.32.

$$P(q) = \frac{1}{V_1^2}\left|\int_0^{2\pi} d\phi \int_0^{\pi} d\vartheta \int_0^{R} r^2 \frac{\sin(\mathrm{qr})}{qr}\right|^2 = \frac{1}{V_1^2}\left|\frac{4\pi}{3} r^3 \left(3\frac{\sin(qr) - qr\cos(qr)}{(qr)^3}\right)\right|^2 \qquad \text{(A.32)}$$

Another approach to obtain some general information about the sample can be based on the analysis of the experimental data considering separately the low and large q region. In particular, for low-q values, the form factor of the scattering particles can be approximated as in equation A.33.

$$P(q) = 1 - \frac{1}{3} q^2 \overline{R}_g^{\,2} + \ldots \qquad \text{(A.33)}$$

By neglecting the higher order of the series in equation A.33 (Guinier law), the size of a rigid particle as well as of flexible molecules can be obtained in terms of the radius of gyration R_g, defined in equation (A.34). The radius of gyration is the average distance of the z elements composing the particle or the molecule from its center of mass.

$$\overline{R}_g^{\,2} = \frac{1}{z}\sum_{i=1}^{z}\left\langle r_i^2 \right\rangle \qquad \text{(A.34)}$$

The limit, in term of q values, for the Guinier law to be safely applied, is established by $q \cdot \overline{R}_g \leq 1.3$. If this condition is not fulfilled, the Guinier law does no longer represent an appropriate approximation of the scattering data.

For the large-q values, another approximation of the scattered intensity is given by the Porod law equation A.35.

$$I(q) \approx \frac{2\pi\Delta\rho^2 S}{q^4} \qquad \text{(A.35)}$$

Where $\Delta\rho$ is the scattering length density difference between the particle and the solvent, while S is the characteristic interfacial surface of the particle. Any deviation from the Porod law in the large-q region can be interpreted in terms of diffusiveness of the interfacial surface.

Even if the Guinier and Porod laws can be used to preliminary characterize the system under investigation, they are approximations. A definitive characterization of the system can be achieved only by interpreting the scattered intensity in the entire q-range explored.

The differential cross section, which leads to the structural properties of the sample, can be obtained from the reduction of the experimental data. Indeed, the measured intensity is related to the differential cross section as in equation A.36.

$$I(\vec{q}) = I_0 \Omega_0 \varepsilon A d T \frac{d\sigma}{d\Omega} \tag{A.36}$$

Where I_0 is the intensity of the incoming beam, Ω_0 is the angle of acceptance of the detector ε is the detector efficiency, A is the sample illuminated area, d is the sample thickness and T is the sample transmission. While d, A and Ω_0 are known from sample preparation and instrumental set up, I_0, ε and T are usually evaluated before the measurement during the calibration of the instrument.

Data reduction consists in normalizing the experimental data for the intensity of the incident neutron flux, the efficiency of the detector and the transmission of the sample. Furthermore, also the contribution coming from the cell, in which the sample was placed, and the background have to be removed. At the end of the data reduction process a set of data which are independent of the instrument and the facility, where they have been collected, is obtained. The reduced data can be then compared with the one collected from other experiments.

SAS data analysis can be performed with suitably developed softwares, which contain a library of several equations for the form factor and the structure factor. These equations can be used to simulate a SAS curve or fit the experimental data.

Appendix B - *Neutron Reflectometry*

B.1 Introduction.

Reflectivity techniques analyze the scattering from surfaces and represent complementary methods to microscopy techniques, with the advantage of introducing only small perturbation into the system under investigation. Furthermore, surfaces at solid-liquid or liquid-liquid interfaces, which are usually inaccessible with microscopy, can be properly characterized.

During a reflectivity experiment, the measurement geometry is different from that of SAS experiment. Flat surfaces reflect the incoming wave and scatter it at the same incident angle. Information about the composition profile normal to the sample surface can be obtained by measuring the intensity of the reflected wave, over the incident one, as function of the scattering vector q,.

In Appendix A, the scattered intensity in the large q-range of a SAS curve was demonstrated to behave according to the Porod law, which connect the collected intensity with the characteristic interface area of the sample. Reflectivity measurements represent an optimized approach to extend Porod law to flat surfaces, thus leading to the characterization of the interface between at least two media.

Two different kind of reflectivity experiments can be distinguished. Specular reflectivity is devoted to the characterization of the interface in the direction (z) normal to the surface. Thus, only the intensity reflected at the same angle of the incident wave is analyzed. This means that the interface is considered as having homogeneous composition in the x,y plane and that the scattering properties of the sample can change only in the z direction (Figure B.1). On the other hand, off-specular reflectivity is used to measure the reflected wave at angles different from the incident one. From this kind of experiments information about inhomogeneities in the direction parallel to the surface are accessible.

As for the scattering phenomenon, also for the reflection from a flat surface, general equations, independent on the nature of the incoming wave, can be identified.

In the first part of this section we do not distinguish if light, X-rays or neutrons are used as probe.

The second part is more focused on neutron reflectivity. A more detailed discussion of neutron and X-ray reflectivity can be found in the references.[95, 128, 129]

B.2 Basics of reflectivity theory.

According to the scheme in Figure B.1, an incoming wave that hit a surface through a medium 0, it is partially reflected by the surface with the same incident angle and partially transmitted through the second medium 1.

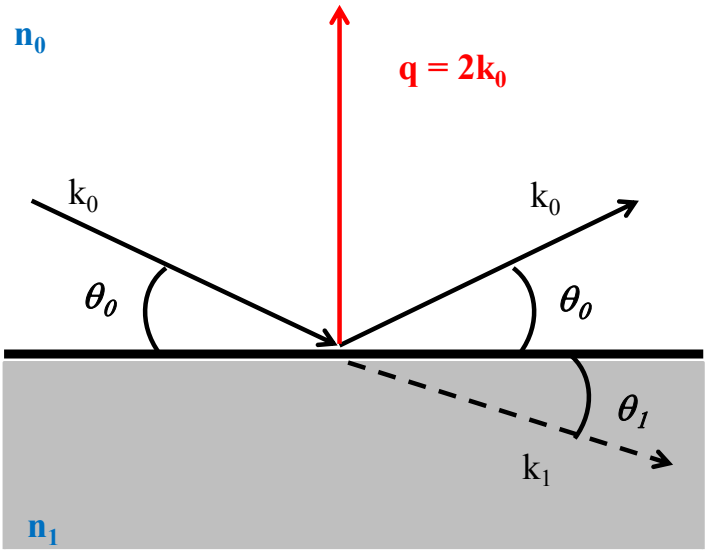

Figure B.1: *Schematic representation of the reflectivity experiment.*

The fundamental laws of optics can be initially recalled to describe this phenomenon. The refractive index is the property of each material that determines the change of direction when an incoming wave approaches the interface between two materials. The refractive index depends on the interaction between the material and the incoming wave, thus it is not surprising that its expression is the one reported in equation (B.1), which contains the scattering length density ρ.

$$n = 1 - \delta + i\beta \tag{B.1}$$

Where $\delta = \frac{\lambda^2 \rho}{2\pi}$ and the second term, $i\beta$, is responsible to the absorption of the incoming wave. As for the theoretical description of the scattering event, also for the reflection, the absorption is neglected. At least for the X-rays and neutrons this condition is often fulfilled. In the case of both X-rays and neutrons, for most of the materials the value of δ is very small corresponding to the order of magnitude of 10^{-6}.

The fundamental laws describing the reflection of an incident plane wave from a flat surface are reported in equations B.2 and B.3.

$$\cos\theta_0 = \cos\theta \tag{B.2}$$

$$n_0 \cos\theta_0 = n_1 \cos\theta_1 \tag{B.3}$$

Where θ_0, θ and θ_1 are respectively the angle of incidence, the one of reflection and the one of refraction, while n_0 and n_1 are the refractive indices of the two media in contact with each other. Equation B.2 is also known as law of reflection. On the other hand, equation B.3 is the Snell law, introducing a relation between the refractive indices of the two media and the angles that corresponds to the incoming and refracted waves.

If the reflected wave is measured as function of the incoming angle, it is possible to verify the existence of the critical angle (θ_c). For $\theta_0 \leq \theta_c$ the maximum interaction between the incoming wave and the surface occurs, since all the intensity is reflected and there is no transmitted beam. In the special case of medium 0 being vacuum ($n_0 = 1$), the expression of the critical angle is given in equation B.4.

$$\cos\theta_c = n_1 \tag{B.4}$$

Since $\cos\theta = 1 - \frac{\theta^2}{2} + \ldots$ and $n_1 = 1 - \delta_1$, it is possible to obtain and approximated expression of the critical angle as in equation B.5.

$$\theta_c = \lambda\sqrt{\frac{\rho}{\pi}} \tag{B.5}$$

The critical angle value for a certain incoming wave passing through vacuum and then being reflected by the surface, is determine by the composition of the second medium.

The amplitude of the incoming wave ($A_0(z)$) in the z direction is defined as in equation B.6. The total amplitude in the medium 0 ($A(z)$) is the sum of the incoming wave and the reflected one (equation B.7), while the total amplitude in the medium 1 is the transmitted wave (equation B.8). The reflected and transmitted amplitudes are expressed in terms of two coefficients, r and t, which represent respectively the fraction of the incoming wave that is reflected or transmitted. Since the possible contributions coming from wave absorption are neglected, the sum of the two coefficients is equal to the unit.

$$A_0(z) = \exp(ik_0 \sin\theta_0 z) \tag{B.6}$$

$$A(z) = \exp(ik_0 \sin\theta_0 z) + r_{01}\exp(ik_0 \sin\theta_0 z) \tag{B.7}$$

$$A_1(z) = t_{01}\exp(ik_0 \sin\theta_1 z) \tag{B.8}$$

The amplitude as well as its derivative is the same on both side of medium 1; hence the wave amplitude varies smoothly along the interface. The reflectivity can be expressed as equation B.9, in which the definition of R as the square of the reflected amplitude modulus was considered.

$$R = \left|\frac{k_0 \sin\theta_0 - k_1 \sin\theta_1}{k_0 \sin\theta_0 + k_1 \sin\theta_1}\right|^2 \tag{B.9}$$

Equation (B.9) is the Fresnel law for reflection. Other convenient way of reformulating this law can be obtained considering the critical angle definition. In particular, since only for $\theta_0 > \theta_c$ there is a refracted amplitude, the equation B.10 can be formulated.

$$k_{z1} = \left({k_{z0}}^2 - {k_{zc}}^2 \right)^{1/2} \tag{B.10}$$

Where $k_z = k \sin\theta$. Thus, equation B.9 can be rewritten as in equation B.11.

$$R = \left| \frac{k_{z0} - \sqrt{{k_{z0}}^2 - {k_{zc}}^2}}{k_{z0} + \sqrt{{k_{z0}}^2 - {k_{zc}}^2}} \right|^2 = \left| \frac{q_{z0} - \sqrt{{q_{z0}}^2 - {q_{zc}}^2}}{q_{z0} + \sqrt{{q_{z0}}^2 - {q_{zc}}^2}} \right|^2 \tag{B.11}$$

It can be demonstrated that for a large value of the incoming angle with respect to the critical angle, the reflectivity at the interface between two media is given by the simple relation reported in equation B.12.

$$R \approx \frac{16\pi^2}{{q_{z0}}^4} \Delta\rho^2 \tag{B.12}$$

Where $\Delta\rho$ is the difference in terms of scattering length density between the two media. As it is shown in equation B.12, the q^{-4}-factor is found as for the Porod law.

During a reflectivity experiment, the sample is usually deposited on a suitable support and it is in contact with a medium such as air or an appropriate solvent. Thus, the presence of one or more layers has to be considered between the medium 0 and 1. A general approach is based on considering the scattering length density not as a constant, but as a function of z. Thus, the equation B.12 becomes equation B.13

$$R(q_z) = \frac{16\pi^2}{{q_z}^2} \left| \int_{-\infty}^{+\infty} \exp(iq_z z) \frac{d\rho(z)}{dz} dz \right|^2 \tag{B.13}$$

According to equation B.13, the reflectivity is proportional to the Fourier transform of the scattering length density profile ($d\rho(z)/dz$). If the interface is a sharp step between two materials with different scattering length density, ρ_1 and ρ_2, the scattering length density profile is simply given by the difference between ρ_1 and ρ_2 times a delta function ($\delta(z)$). Since the Fourier transform of a delta function is 1, the expression of $R(q_z)$ is given again by equation B.12. In principle, we can add other terms if more than one sharp step with different scattering length density is needed However, a more realistic representation of the system can be achieved by substituting the delta function by a mathematical function describing the interface shape. In particular, it is possible to consider that the

interface is a diffuse interface. This situation can indeed be represented with an error function (equation B.14).

$$\rho(z) = \frac{\Delta\rho}{\sigma\sqrt{2\pi}} \int_{-\infty}^{z} \exp\left(\frac{z^2}{2\sigma^2}\right) dz \tag{B.14}$$

$$\frac{d\rho(z)}{dz} = \frac{\Delta\rho}{\sigma\sqrt{2\pi}} \exp\left(\frac{z^2}{2\sigma^2}\right) dz \tag{B.15}$$

The reflectivity expression is then given by equation B.16.

$$R(q_z) = \frac{16\pi^2}{q_z^{\,2}} \Delta\rho^2(-q_z^{\,2}\sigma^2) \tag{B.16}$$

By comparing equation B.16 with equation B.13, it is evident that in the case of a diffusive interface, the reflectivity is expressed as equation B.12 times a second term taking into account the faster reflectivity decrease with q because of the interface shape. The σ parameter is related to the characteristics of the interface between the two materials, and in particular at its roughness. Indeed, the more a surface is rough, the more the interface with a second material will be diffuse and faster will be the reflectivity decay with q.

The great advantage of the obtained reflectivity expression is that it underlines in a simple way the relation between R and the composition variation along the z direction, which allows determining the sample thickness and the scattering length density profile. However, it is worth to note that even equation B.16 does not represent a complete description of the system. Indeed, the reflectivity expression that was obtained does hold only for large incident angle with respect to the critical angle. In order to obtain an expression of the reflectivity for the entire q range, including the critical angle, the optical matrix method proposed by Born and Wolf can be used.

The optical matrix method allows calculating the reflectivity from any number of parallel homogeneous layers. This means that the sample can be represented by a stack of parallel layers each of them being characterized by a certain thickness and scattering length density. The optical matrix method leads to an exact calculation of the reflectivity profile.

Each of the layer composing the sample can be characterized by a matrix M_i (equation B.17)

$$M_i = \begin{pmatrix} \cos\beta_i & -(i/\nu_i)\sin\beta_i \\ -i\nu_i \sin\beta_i & \cos\beta_i \end{pmatrix} \tag{B.17}$$

Where $\beta_i = kn_i d_i \sin\theta$ and d_i is the thickness of the i layer.

The reflectivity is obtained from the combination of the matrices used to describe the sample. For a two-layers sample the reflectivity can be calculated as in equation B.18.

$$R = \left| \frac{(M_{11} + M_{12}\nu_s)\nu_a - (M_{21} + M_{22})\nu_s}{(M_{11} + M_{12}\nu_s)\nu_a + (M_{21} + M_{22})\nu_s} \right|^2 \quad \text{(B.18)}$$

Equation B.18 evidently resembles equation B.9. However, the terms that appear in equation B.18 are more complex because they take into account of the more complex composition of the sample. Eventually the matrix describing each layer of the sample can be slightly modified to include also the interface roughness. Although it doesn't lead directly to the scattering length density profile, the optical matrix method offers the advantage of exactly calculating the reflectivity at any angle.

B.3 Neutron Reflectometry (NR).

Neutron Reflectometry, because of the energy, the wavelengths and the magnetic moments of thermal neutrons, is a powerful technique for studying systems in soft matter, such as biological membranes or polymer films, but also magnetic or superconducting multilayer systems.

Typically, neutron reflectivity experiments require the sample to be deposited on a highly reflecting flat surface. Different kinds of supports are available such as monocrystalline silicon or sapphire. Before proceeding with the measurements on the sample, neutron reflectivity profiles for the bare support should be collected in order to fully characterize its surface. In particular, silicon crystals present a thin layer of amorphous SiO_2, which is produced by the surface being exposed to the atmosphere. Thus, determining the thickness and the roughness of the SiO_2 layer is desirable, before sample deposition. The structural parameters of the support can be fixed during the data analysis concerning the sample under investigation.

The the sample together with the support is sealed in a suitably developed cell, where it can be placed in contact with different kinds of media such as air or solvents. The support and the medium in contact with the sample are considered as having an infinite thickness and a fixed scattering length density. The sample, which is absorbed on the support surface, can be composed by a single layer or a more complex structure.

In order to analyze the collected data is crucial to subtract the background. The reflectivity in the off-specular geometry is measured to estimate the background and subsequently subtracted from the specular reflectivity. The background is mostly generated from the incoherent scattering coming from the medium in contact with the sample and the cell. Since it does not depend on q, its value will be the same for both off-specular and specular reflectivity. In the experiment aimed at characterizing solid/liquid interface, it has to be considered that the liquid medium, especially in the case of water, is responsible for a very strong background. Thus, in order to improve the signal/noise ratio, usually

the solid/liquid cell is mounted in the instrument such that the incoming wave passes through the solid support and is successively reflected at the solid/liquid interface.

Once the experimental data are reduced to absolute unit, they can be analyzed with suitably developed software to give back the composition profile along the direction normal to the surface. In the case of solid/liquid interface, such as a lipid membrane in contact with water, one reflectivity profile may not provide a unique scattering length density profile. Thus, the use of different isotopic contrasts can be adopted in order to achieve a higher degree of confidence with the parameters optimized from the data analysis. As an example, the reflectivity curves corresponding to the a lipid membrane are usually collected in three solvents with different isotopic composition, i.e. H_2O, D_2O and H_2O/D_2O mixtures. Even if the obtained profiles look differently, they are still originated from the same sample. Thus, the simultaneous interpretation of the reflectivity curves in the different solvents leads to an unambiguous model for the sample structure.

Appendix C - *Dynamic Light Scattering*

C.1 Introduction.

Appendix A demonstrated that by measuring the intensity of the wave scattered from a sample, as function of the scattering vector q, information about the shape and the size of particle dispersed in a uniform matrix can be obtained. Even if the particular case of X-ray and neutron scattering was treated in details, it can be demonstrated that the same kind of conclusions are valid also for light scattering. In the previous discussions, the time dependence of the positions of the particles was not taken into account, which leads a great simplification of the equation describing the scattering event. In order to avoid the explicit the time-dependence, the intensity scattered from the sample, was considered as arising from the average positions of the scatterers at thermal equilibrium. In light scattering, this assumption represents the base of Static Light Scattering (SLS). Thus, all the equation reported in Appendix A, can be mutated to describe the theory of SLS.[1], X-ray and neutron scattering have access to a different q-range with respect to light scattering, since q depends on the angle, but also on the incoming wavelength. In particular, light scattering is suitable to characterize the sample at larger scale-length than neutron and X-ray scattering. However, in the case of a hierarchical system it is very powerful to combine these techniques and fully characterize the sample at all its characteristic scales.

Dynamic Light Scattering (DLS), also known with the general name of Quasi-Elastic Scattering is a technique aimed at the obtainment of dynamical information about the system under investigation. With respect to SLS, the time-dependence of the positions of the particles is now taken into account. As already highlighted in the previous sections, different probes can be used leading to the characterization of the sample at different length or time scales. Thus, if QES measurements are performed using visible light the Brownian diffusion of a dilute particle suspension can be characterized. On the other hand, if QES measurements are performed using thermal neutrons, atomic motions can be investigated. As an example, Quasi-Elastic Neutron Scattering (QENS) experiments are used to investigate hydrogen dynamics, which for example can be related to water dynamics into a matrix such as a polymer film.

[1] *An interesting application of SLS involves the analysis of data collected at different concentration of particles dispersed in a liquid medium to obtain their mean molecular weight. Further details about this application of SLS experiments can be found in the references.*

DLS has become a very popular technique and many instruments are now found in most of the laboratories. The great success of this technique is based on the simplicity of the instrumental setup and the solid software that is available for the data analysis. The measurement time can be very low (a few seconds), so the kinetic of the processes in solution can be suitably investigated. Since DLS deals with the diffusion of particles, liquid samples are needed. In particular, dilute suspensions of particles are recommended to avoid multiple scattering events. The particle composition can be very different, so many applications of DLS are found for the characterization of amphiphilic aggregates diffusion, but also aggregates formation, as well as proteins, polymer and in general macromolecules diffusion.

Even if this appendix is focused on DLS, a general formalism will be recalled in order to highlight the complementarity of information that can be obtained if a different probe instead of light is used. A detailed presentation of the theory and experimental application of QES can be found in the references.[90, 98, 130, 131]

C.2 Basics of QES theory.

In the case of light scattering, the electric component of the incoming wave is responsible for the interaction with the electrons of the sample. In particular, the incoming electric field induces an oscillating dipole moment according to the particle polarizability.

$$\vec{\mu} = \alpha \cdot \vec{E}_i \tag{C.1}$$

$$E_i(\vec{r},t) = n_i E_0 \exp i\left[\vec{\kappa}_i \cdot \vec{r} - \omega_i t\right] \tag{C.2}$$

In the general expression of the induced dipole, the polarizability is a tensor, since it depends on the shape and the size of the particle. However, in the special case of spherical particles, a highly symmetric system, the polarizability is a constant. Equation C.1 also underlines that the induced dipole moment oscillates with the same frequency of the incoming electric field. If no other interaction occurs between the incoming wave and the sample, i.e. absorption, the induced dipole moment will be the secondary source of the scattered electric field. At distance R from the sample, the expression of the scattered electric field can be derived considering the scheme reported in Figure A.1.

$$E_s(\vec{R},t) = \frac{}{4\pi R\varepsilon_0} \exp i(\kappa_f R - \omega_i t)\alpha_{if}(\vec{q},t) \tag{C.3}$$

In particular, the sample was considered as characterized by a mean dielectric constant ε_0, while $\delta\varepsilon_{if}$ represent the fluctuation of the dielectric constant in the sample, related to the particle spatial distribution. The dielectric constant fluctuation was already expressed in equation C.3 as the Fourier transform in q-space of the corresponding function of r (equation C.4).

$$\delta\varepsilon(\vec{q},t) = \int_V \delta\varepsilon(\vec{r},t)\, e^{\quad} \, d\vec{r} \tag{C.4}$$

A similar expression of the scattered electric field can be obtained in terms of polarizability a particle, which can be easily related to its structural properties.[2]

$$E_s(\vec{R},t) = \frac{}{4\pi R\varepsilon_0} \exp i(k_f R - \omega_i t)\, \delta\alpha_{if}(\vec{q},t) \tag{C.5}$$

$$\delta\alpha_{if}\left(\vec{q},t\right) = (n_i \cdot n_f)\alpha \sum_{j=1}^{N} e^{iq(r_j(t)} \tag{C.6}$$

As the dielectric constant, the polarizability varies in space and time (equation.6) because of the spatial distribution of the particles and their motions (vibration, rotation and translation).

By considering the square modulus of the scattered electric field, the measured scattered intensity has an expression very close to the one obtained for X-ray and neutron scattering (equation A.24). The main difference is that the fluctuation of the scattering length is now substituted by the polarizability fluctuation. In all the equations, the electric field and the polarizability fluctuation depends on both the spatial coordinates and time.

The scattered intensity arising from a particle suspension, measured at fixed q value, thus at constant incident wavelength and fixed scattering angle, is reported in Figure C.1. Since the scattered intensity depends on the positions particles, which do change with time, the scattered intensity will look like a noise pattern, composed by fluctuations around an average value. The scattered intensity has to be converted in the corresponding autocorrelation function to extract information about the particle motion. This is actually a standard approach to treat randomly fluctuating quantities. Before dealing with the intensity autocorrelation function, the electric field autocorrelation is introduced, recalling equation (C.5).

$$\left\langle E_s^*(\vec{R},t) E_s(\vec{R},t) \right\rangle = \frac{}{16\pi^2 R^2 \varepsilon_0^{\,2}} \left\langle \delta\alpha_{if}(\vec{q},t)\delta\alpha_{if}(\vec{q},t) \right\rangle e \tag{C.7}$$

[2] *In general, a particle within a suspension can present electronic charge distortion due to inter-particle collisions. For this reason, in the expression of the scattered electric field, the isolated particle polarizability should be replaced by an effective polarizability, which takes into account of the effects of collisions.*

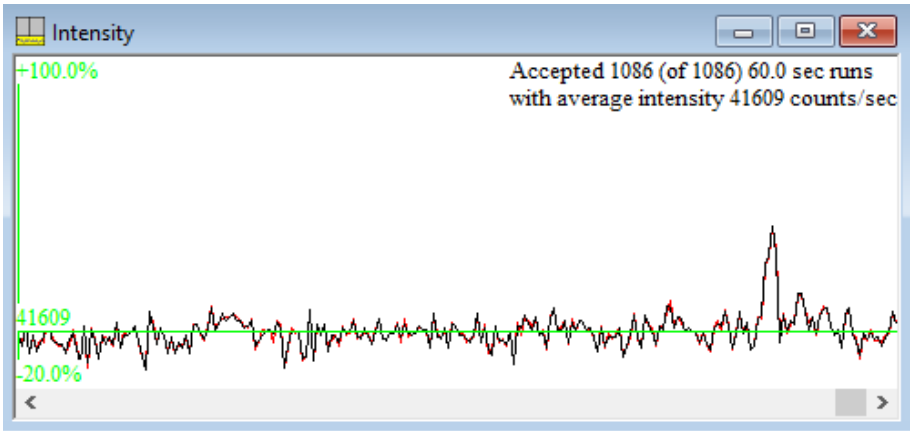

Figure C.1: *Scattered intensity as function of time. Data showed in the picture refers to a suspension of inorganic nanoparticles. The collected data were visualized and analyzed with PrecisionDeconvolve software.*

The autocorrelation function, reported in equation C.7, gives information about how the scattered electric field changes at time *t* with respect to its initial value at time *0*. The bracket indicates that the product between the two scattered electric field values is averaged over the measurement time, which has to be large with respect to the typical fluctuation time. The electric field autocorrelation function can be converted into the electric field spectral density by means of Fourier transformation.

$$I_E(\omega) = \frac{1}{2\pi}\int_{-\infty}^{+\infty} \left\langle E^*(0)E(t)\right\rangle e^{i\omega t}dt \tag{C.8}$$

Fourier transform connect a function of time (the electric field autocorrelation function) with a function of frequency, ω, (the electric field spectral density). The shape of the I_E in the frequency domain is governed by the difference between ω_f and ω_i, respectively the scattered and incident frequency. Equation C.9 is obtained by substituting equation C.7 into equation C.8.

$$I_E(\vec{q},\omega_f,n) = \frac{}{2\pi}\frac{}{16\pi^2R^2\varepsilon_0^{\,2}}\int_{-\infty} \alpha_{if}(\vec{q},0)\alpha_{if}(\vec{q},t)e \qquad dt \tag{C.9}$$

Where n_i and n_f define the direction of the incoming and the scattered wave.

In the case of an elastic scattering event, ω_f and ω_i are the same, and the spectral density is a line. However, owing to the *Uncertainty Principle*, it is impossible to detect a line spectrum. Indeed, there is always a finite probability for the incoming wave to exchange energy with the sample. All these considerations explain the broadening of the line in the spectral density to give a peak. This peak is also known as elastic peak. Besides the *Uncertainty Principle*, the elastic peak is additionally

broadened because of the motions of the scatterers. The techniques that aim to characterization of the broadening of the purely elastic peak are named Quasi-Elastic Scattering (QES) techniques.[3]
Whatever is the probe used for the experiment, the motions of the scatterers within the sample produce fluctuations of the scattered intensity. The temporal correlation function of these fluctuations provides information about the diffusion coefficient of the scatterers.

C.3 Dynamic Light Scattering.

In DLS field it is possible to identify two different kind of approach for determining the electric field autocorrelation function, also known as $g^1(t)$. The first one is the filter method, which consists on analyzing the scattered intensity in terms of frequency, and thus measuring the spectral density. As reported in equation C.9, once the spectral density is measured, the electric field autocorrelation function can be calculated. On the other hand, the optical mixing methods directly measure the autocorrelation functions. Among the optical mixing method, the homodyne and heterodyne methods can be distinguished. The homodyne method, which will be discussed in this section, measures the scattered intensity from the sample and calculates its autocorrelation function, also known as $g^2(t)$. The heterodyne method combines the intensity scattered from the sample with a fraction of the intensity coming from the laser source. By using this approach, it can be demonstrated that even if more complex instrumental setup and data analysis with respect to the homodyne method are involved, $g^1(t)$ can be directly determined.
Typical samples analyzed by means of DLS are dilute suspensions of particles, where the scattered intensity from each particle can be considered independent. Under this condition, $g^2(t)$ is related to $g^1(t)$ according to equation C.10.

$$g^2(t) = I_s^2\left(1+\beta\left|g^1(t)\right|^2\right) \tag{C.10}$$

Where I_s^2 represent the square of the average intensity scattered by the sample and β is an efficiency factor, related to the instrumental setup. In particular, if the illuminated area is small compared to the coherence area[4] $\beta \approx 1$. Hence, equation C.10 demonstrates that by measuring the scattered intensity autocorrelation function, the scattered electric field autocorrelation function can be calculated. The

[3] *The self-correlation term in equation A.22, where also the position time dependence is taken into account, is related through Fourier transformation to the Van-Hove self space-time correlation function. This function can be obtained from a similar argument to the one used for the Patterson function. The Van-Hove correlation function correlates positions of the same particles but at two different time.*
[4] *The coherence area defines the area where the spatial correlation function of the electric field is substantially different from zero.*

time fluctuations of the scattered electric field are produced by the polarizability fluctuations, which are related to the motion of the particles. From the evaluation of $g^1(t)$, characteristic parameters of the dynamics of the particles within the suspension can be derived upon identifying a suitable model to describe the particle motion. In the case of Brownian motion, for an ensemble of equal particles, the particle displacement is related to its translational diffusion coefficient (D) by equation C.11.

$$\Delta r_j = 6D\Delta t \qquad \text{(C.11)}$$

If the equation C.11 is substituted in the expression of the scattered electric field (equation C.5) and $g^1(t)$ is calculated according to equation C.7, equation C.12 is obtained.[5]

$$g^1(t) = \mathrm{e}^{-Dq^2t} \qquad \text{(C.12)}$$

In particular, the above reported simple expression of $g^1(t)$ takes into account of the electric field autocorrelation function normalization for the incoming intensity. Equation C.12 holds for a system composed by particle, showing all the same size and shape. However, in a real sample $g^1(t)$ depends on a the distribution of diffusion coefficients reflecting the sizes and shapes of the particles. In other words, equation C.12 has to be reformulated in order to take into account of the polydispersity of the system under investigation.

$$g^1(t) = \int G(\Gamma)\,\mathrm{e}^{-\Gamma t}\,d\Gamma \qquad \text{(C.13)}$$

Where $\Gamma = Dq^2$ and is the inverse of the characteristic diffusion time of the particles, which also represent the time at which the correlation between the scattered electric field values is lost.

In conclusion, the scattered electric field autocorrelation function can be calculated from DLS measurement of the intensity autocorrelation function. The collected data can be analyzed according to equation C13 and the mean diffusion coefficient as well as its distribution function can be estimated. Suitably developed algorithms are available in order to perform data analysis even in the case of complex systems composed by different populations of diffusing particles.

Under the specific condition of spherical non-interacting particles that diffuse in a continuum medium, the Stokes-Einstein relation (equation(C.14)) can be used to calculated the hydrodynamic radius (R_h)of the particles from their diffusion coefficient.

$$D = \frac{K_B T}{6\pi\eta R_h} \qquad \text{(C.14)}$$

[5] *It can be demonstrated that according to the diffusion theory, $g^1(t)$ can be fitted as a single exponential $e^{-t/\tau}$, where τ is the particle characteristic time of diffusion. Since $\tau=(q^2D)^{-1}$, equation (C.11) was obtained.*

Where η is the viscosity of the medium. Thus, DLS can also be used to determine the hydrodynamic radius of the particles in the suspension, which is the effective radius of the particle plus the solvation shells that are diffusing with it

Appendix D - *In vitro and in vivo experiments*

D.1: In vitro bioscreens.

The biological activity of the functionalized SPIONs was tested by means of citoxicity *in vitro* experiements. In particular, SPIONs with the lysophosphocholine 18LPC were tested in order to evaluate their cellular toxicity. In addition, the toxicity with respect to different cancer cell lines was investigated for the SPIONs functionalized with the ruthenium complex ToThuCholRu.

In details, Human HaCaT keratinocytes , murine 3T3L-1 fibroblasts, human Calu-6 and A549 lung carcinoma cell lines were grown in Dulbecco's modified Eagle's medium (DMEM, Invitrogen, Paisley, UK) containing high glucose (4.5 g/l), while human MCF-7 breast adenocarcinoma cells were grown in RPMI 1640 medium (Invitrogen, Paisley, UK). Media were supplemented with 10% fetal bovine serum (FBS, Cambrex, Verviers, Belgium), L-glutamine (2 mM, Sigma Aldrich), penicillin (100 units/ml, Sigma Aldrich) and streptomycin (100 mg/ml, Sigma Aldrich). All the cells were cultured in a humidified 5% carbon dioxide atmosphere at 37 °C.

The nanoparticles bioactivity was investigated by the estimation of a "cell survival index", arising from the combination of cell viability evaluation with cell counting. The cell lines were washed with PBS buffer solution (Sigma Aldrich), collected by trypsine (Sigma Aldrich) and then inoculated in a 96-microwell culture plates at density of 10^4 cells/well. Cells were allowed to grow for 48 h, then the medium was replaced with fresh medium and treated for further 48 h with different functionalized SPION concentration. Using the same experimental procedure, cell cultures were also incubated with the low molecular weight ruthenium complex AziRu and cisplatin (*c*DDP), as positive control for cytotoxic effects. Cell viability was evaluated with MTT assay, which measures the level of mitochondrial dehydrogenase activity using the yellow 3-(4,5-dimethyl-2-thiazolyl)-2,5-diphenyl-2H tetrazolium bromide (MTT, Sigma) as substrate. The assay was based on the redox ability of living mitochondria to convert dissolved MTT into insoluble purple formazan. Briefly, after the treatments the medium was removed and the cells were incubated with 20 µl/well MTT solution (5 mg/ml) for 1 h in a humidified 5% CO2 incubator at 37 °C. The incubation was stopped by removing the MTT solution and by adding 100 µl/well of DMSO to solubilize the purple formazan. Finally, the absorbance was monitored at 550 nm by using a microplate reader (iMark microplate reader, Bio-Rad, Milan, Italy).

Cell number was determined by TC20 automated cell counter (Bio-Rad, Milan, Italy), providing an accurate and reproducible total count of cells and a live/dead ratio in one step by a specific dye (trypan blue) exclusion assay. Following the same principle used in hemocytometers, Bio-Rad's TC20 automated cell counter uses disposable slides, TC20 trypan blue dye (filter-sterilized 0.4% trypan blue dye w/v in 0.81% sodium chloride and 0.06% potassium phosphate dibasic solution) and a CCD camera to count cells based on the analyses of captured images. Once the loaded slide is inserted into the slide port, the TC20 automatically focuses on the cells, detects the presence of trypan blue dye and provides the count. When cells are damaged or dead**,** *trypan blue* can enter the cell allowing dead cells to be counted. Operationally, after bioscreen incubations in standard 96-microwell culture plates, the medium was removed and the cells were collected. Ten microliters of cell suspension, mixed first with 0.4% trypan blue solution at 1:1 ratio, were directly loaded into the chambers of disposable slides. The results are displayed as total cell count (number of cells/ml). If trypan blue is detected, the instrument also accounts for the dilution and shows live cell count and percent viability. Total counts and live/dead ratio fromrandom samples for each cell line were subjected to comparisons with manual hemocytometers in control experiments.

The calculation of the concentration required to inhibit the net increase in the cell number and viability by 50% (IC_{50}) was based on plots of data carried out in triplicates and repeated five times (total n =15). IC_{50} values were obtained using a dose-response curve by nonlinear regression using a curve fitting program, GraphPadPrism 5.0, and are expressed as mean ± SEM (n = 15).

D.2 MRI experiments.

Functionalized SPIONs were also tested as effective MRI contrast agents performing two different set of experiments. Initially, a phantom was prepared consisting of a culture cell plate containing SPIONs in H_2O and 1% agar gel solutions at different concentrations (from 0.016 mg/ml up to 2.5 mg/ml, [Fe] concentration) located in the plate wells. The T_1 and T_2 relaxation profiles of the SPIONs were then assessed at 1.5 and 3 T using clinical scanners (1.5 T Signa Excite and 3 T Signa HDxT, GE Healthcare, USA, respectively). The reception of the MR signal was performed using a clinical head coil to increase the filling factor with the phantom placed at the center of the coil.

The longitudinal (T_1) relaxation time of the solutions was measured using a standard Inversion Recovery (IR) with the following parameters: TR = 9000, TE = 7.6 ms at 3 T and 6.7 at 1.5 T, TI = 100 – 2100 ms in steps of 200 ms, FOV = 18x18 cm for 3 T and 23x23 cm at 1.5 T, matrix 192x192 pixels, slice thickness = 3 mm. The transverse (T_2) relaxation time was measured with a T_2-weighted

Spin Echo sequence using the following parameters: TR = 1500 ms at 3 T and 1000 ms at 1.5 T; TE = 5.2 – 160.3 ms at 1.5 T and 6.9 – 110.1 ms at 3 T; 16 scans, FOV = 16x16 cm at 3 T and 23x23 cm at 1.5 T, matrix 192x192 pixels, slice thickness = 7 mm. To evaluate the effect of low field on T_2-relaxivity we used an 0.32 T open magnet and 0.5 T open magnet (MrOpen, Paramed Medical System), with a dedicated head multi-array coils: a 2-dimensional acquisitions were obtained: proton density (PD)–weighted oblique coronal and oblique sagittal planes, T2-weighted fast spin echo (FSE) oblique coronal and oblique axial planes, gradient echo (GRE) oblique axial plane, and short tau inversion recovery (STIR) oblique coronal plane. The longitudinal (R_1) and transverse (R_2) relaxation rates were calculated as the inverse of T_1 and T_2 relaxation times, respectively. The longitudinal (r_1) and transverse (r_2) relaxivity (expressed in mM^{-1} s^{-1} [Fe] concentration) were then estimated as the slope of the regression line obtained for R_1 and R_2 versus the SPIONs concentration.

Subsequently, SPIONs activity as imaging contrast agents was as well evaluated. In particular, MRI in vivo studies were performed at 3 T using a clinical scanner (Signa HDxT, GE Healthcare, USA) equipped with a dedicated birdcage coil for small animal studies (Rapid Biomedical, Rimpar, Germany). About 0.4 mg (600 μL) of NPs previously diluted in saline solution were manually injected in bolus in the tail vein of Wistar rats (300 mg body weight). Male Wistar rats 10-12 weeks old and weighing 310 ± 3 g were used in the study: rats were anesthetized using Zoletil® + xylazine (50 and 3 mg/kg respectively).

A Fast Spin Echo sequence for T_2 mapping was applied for the acquisition with the following parameters: TR = 1000 ms; TE = 4.7 – 102.9 ms, Echo times = 8; FOV = 18x18 cm, slice thickness = 3 mm; matrix = 224x224, total acquisition time = 24 sec.

Images in coronal plane were acquired in sequence for the first 5 minutes after injection to include a few organs of interest such as liver, kidneys and myocardium. Later the acquisition was performed at increasing time intervals, up to 60 minutes after the injection. A ROI was selected on the image relative to the anatomical district of interest and the corresponding T_2 was assessed for each acquisition; the transverse relaxation rate (R_2) was estimated as the inverse of T_2. Experiments with animals were performed after approval by the dedicated Committee designed by the Board of the Centre for Experimental Biology at the CNR Research Area (Pisa) and were authorised by the Italian Ministry of Health according to current national legislation (dlg26 / 2014). The Design and Realization of the project has been guided by the respect of European guidelines with particular reference to the principle of the "*three R*" and ethical use of animals.

References:

1. Teja, A.S. and P.-Y. Koh, *Synthesis, properties, and applications of magnetic iron oxide nanoparticles.* Progress in Crystal Growth and Characterization of Materials, 2009. **55**(1–2): p. 22-45.
2. Wei, W., et al., *Recent progress on magnetic iron oxide nanoparticles: synthesis, surface functional strategies and biomedical applications.* Science and Technology of Advanced Materials, 2015. **16**(2): p. 023501.
3. Bao, Y., et al., *Magnetic Nanoparticles: Material Engineering and Emerging Applications in Lithography and Biomedicine.* J Mater Sci, 2016. **51**(1): p. 513-553.
4. Dorfman, J.F.a.J., *Spontaneous and Induced Magnetisation in Ferromagnetic Bodies.* Nature 1930. **126**: p. 274-275.
5. Kittel, C., *Theory of the Structure of Ferromagnetic Domains in Films and Small Particles.* Physical Review, 1946. **70**(11-12): p. 965-971.
6. Bean, C.P. and J.D. Livingston, *Superparamagnetism.* Journal of Applied Physics, 1959. **30**(4): p. S120-S129.
7. Zucolotto, B., et al., *Reliable evaluation of magnetic properties of nanoparticle systems.* Journal of Applied Physics, 2015. **118**(11).
8. Ling, D., N. Lee, and T. Hyeon, *Chemical Synthesis and Assembly of Uniformly Sized Iron Oxide Nanoparticles for Medical Applications.* Accounts of Chemical Research, 2015. **48**(5): p. 1276-1285.
9. Lee, N., et al., *Iron Oxide Based Nanoparticles for Multimodal Imaging and Magnetoresponsive Therapy.* Chem Rev, 2015. **115**(19): p. 10637-89.
10. Wang, H., et al., *Cetyltrimethylammonium Bromide-Coated Fe(3)O(4) Magnetic Nanoparticles for Analysis of 15 Trace Polycyclic Aromatic Hydrocarbons in Aquatic Environments by Ultraperformance, Liquid Chromatography With Fluorescence Detection.* Anal Chem, 2015. **87**(15): p. 7667-75.
11. Campanella, A., et al., *Nanocomposites composed of HEUR polymer and magnetite iron oxide nanoparticles: Structure and magnetic response of the hydrogel and dried state.* Polymer, 2015. **60**: p. 176-185.
12. Wu, L., B. Shen, and S. Sun, *Synthesis and assembly of barium-doped iron oxide nanoparticles and nanomagnets.* Nanoscale, 2015. **7**(39): p. 16165-9.
13. Wang, D., et al., *Magnetic and Dendritic Catalysts.* Accounts of Chemical Research, 2015. **48**(7): p. 1871-1880.
14. Ramimoghadam, D., S. Bagheri, and S.B. Abd Hamid, *Stable monodisperse nanomagnetic colloidal suspensions: An overview.* Colloids Surf B Biointerfaces, 2015. **133**: p. 388-411.
15. Kandasamy, G. and D. Maity, *Recent advances in superparamagnetic iron oxide nanoparticles (SPIONs) for in vitro and in vivo cancer nanotheranostics.* International Journal of Pharmaceutics, 2015. **496**(2): p. 191-218.
16. Arami, H., et al., *In vivo delivery, pharmacokinetics, biodistribution and toxicity of iron oxide nanoparticles.* Chem Soc Rev, 2015. **44**(23): p. 8576-607.
17. Tietze, R., et al., *Magnetic nanoparticle-based drug delivery for cancer therapy.* Biochem Biophys Res Commun, 2015. **468**(3): p. 463-470.
18. Tombácz, E., et al., *Magnetic iron oxide nanoparticles: Recent trends in design and synthesis of magnetoresponsive nanosystems.* Biochem Biophys Res Commun, 2015. **468**(3): p. 442-453.
19. Wilczewska, A.Z., et al., *Nanoparticles as drug delivery systems.* Pharmacological Reports, 2012. **64**(5): p. 1020-1037.
20. Rieffel, J., U. Chitgupi, and J.F. Lovell, *Recent Advances in Higher-Order, Multimodal, Biomedical Imaging Agents.* Small, 2015. **11**(35): p. 4445-4461.
21. Lim, E.K., et al., *Nanomaterials for theranostics: recent advances and future challenges.* Chem Rev, 2015. **115**(1): p. 327-94.

22. Patsula, V., et al., *Size-dependent magnetic properties of iron oxide nanoparticles.* Journal of Physics and Chemistry of Solids, 2016. **88**: p. 24-30.
23. Aadinath, W., T. Ghosh, and C. Anandharamakrishnan, *Multimodal magnetic nano-carriers for cancer treatment: Challenges and advancements.* Journal of Magnetism and Magnetic Materials, 2016. **401**: p. 1159-1172.
24. Pineiro, Y., et al., *Iron Oxide Based Nanoparticles for Magnetic Hyperthermia Strategies in Biological Applications.* European Journal of Inorganic Chemistry, 2015(27): p. 4495-4509.
25. Demirer, G.S., A.C. Okur, and S. Kizilel, *Synthesis and design of biologically inspired biocompatible iron oxide nanoparticles for biomedical applications.* Journal of Materials Chemistry B, 2015. **3**(40): p. 7831-7849.
26. Hao, R., et al., *Synthesis, Functionalization, and Biomedical Applications of Multifunctional Magnetic Nanoparticles.* Advanced Materials, 2010. **22**(25): p. 2729-2742.
27. Lu, A.H., E.L. Salabas, and F. Schuth, *Magnetic nanoparticles: Synthesis, protection, functionalization, and application.* Angewandte Chemie-International Edition, 2007. **46**(8): p. 1222-1244.
28. Ling, D.S. and T. Hyeon, *Chemical Design of Biocompatible Iron Oxide Nanoparticles for Medical Applications.* Small, 2013. **9**(9-10): p. 1450-1466.
29. Sun, S. and H. Zeng, *Size-Controlled Synthesis of Magnetite Nanoparticles.* Journal of the American Chemical Society, 2002. **124**(28): p. 8204-8205.
30. Sun, S., et al., *Monodisperse MFe2O4 (M = Fe, Co, Mn) Nanoparticles.* Journal of the American Chemical Society, 2004. **126**(1): p. 273-279.
31. Turcheniuk, K., et al., *Recent advances in surface chemistry strategies for the fabrication of functional iron oxide based magnetic nanoparticles.* Nanoscale, 2013. **5**(22): p. 10729-10752.
32. Mahmoudi, M., et al., *Cell toxicity of superparamagnetic iron oxide nanoparticles.* J Colloid Interface Sci, 2009. **336**(2): p. 510-8.
33. Bhattacharya, D., et al., *Synthesis, characterization, and in vitro biological evaluation of highly stable diversely functionalized superparamagnetic iron oxide nanoparticles.* Journal of Nanoparticle Research, 2011. **13**(9): p. 4173-4188.
34. Thao Truong-Dinh Tran∗, T.V.V., Phuong Ha-Lien Tran, *Design of iron oxide nanoparticles decorated oleicacid and bovine serum albumin for drug delivery.* Chemical Engineering Research and Design, 2015. **9**(94): p. 112-118.
35. Esra Maltas , M.O., *Spectrofluorometric and thermal gravimetric study on binding interaction of thiabendazole with hemoglobin on epoxy-functionalized magnetic nanoparticles.* Materials Science and Engineering C, 2015. **54**: p. 43-49.
36. Kishore Kumar Nair, R.K., Nusrat Iqbal, Abshar Hasan, Samsul Alam and SKRaza, *High yield, facile aqueous synthesis and characterization of C18functionalized iron oxide nanoparticles.* Materials Research Express, 2015. **2**(4).
37. White, E.E., et al., *Functionalized iron oxide nanoparticles for controlling the movement of immune cells.* Nanoscale, 2015. **7**(17): p. 7780-7789.
38. Rahman, M., et al., *Incorporation of iron oxide nanoparticles into temperature-responsive poly (N-isopropylacrylamide-co-acrylic acid) P (NIPAAm-AA) polymer hydrogel.* Journal of Polymer Research, 2015. **22**(3): p. 1-9.
39. Chiper, M., et al., *Colloidal stability and thermo-responsive properties of iron oxide nanoparticles coated with polymers: advantages of Pluronic (R) F68-PEG mixture.* Nanotechnology, 2013. **24**(39).
40. Hauser, H. and P. Fulmek, *The Effect of Mechanical-Stress on the Magnetization Curves of Ni-Single and Fesi-Single Crystals at Strong Fields.* Ieee Transactions on Magnetics, 1992. **28**(3): p. 1815-1825.
41. Khandhar, A.P., et al., *Tuning Surface Coatings of Optimized Magnetite Nanoparticle Tracers for In Vivo Magnetic Particle Imaging.* Ieee Transactions on Magnetics, 2015. **51**(2).
42. Pourcelle, V., et al., *Functionalization of the PEG Corona of Nanoparticles by Clip Photochemistry in Water: Application to the Grafting of RGD Ligands on PEGylated USPIO Imaging Agent.* Bioconjug Chem, 2015. **26**(5): p. 822-9.
43. Gautier, J., et al., *Efficacy and Hemotoxicity of Stealth Doxorubicin-Loaded Magnetic Nanovectors on Breast Cancer Xenografts.* Journal of Biomedical Nanotechnology, 2015. **11**(1): p. 177-189.
44. Halupka-Bryl, M., et al., *Synthesis and in vitro and in vivo evaluations of poly(ethylene glycol)-block-poly(4-vinylbenzylphosphonate) magnetic nanoparticles containing doxorubicin as a potential targeted drug delivery system.* Colloids Surf B Biointerfaces, 2014. **118**: p. 140-7.

45. Chiang, C.S., et al., *Magnetically Targeted Nanocapsules for PAA-Cisplatin-Conjugated Cores in PVA/SPIO Shells via Surfactant-Free Emulsion for Reduced Nephrotoxicity and Enhanced Lung Cancer Therapy.* Adv Healthc Mater, 2015. **4**(7): p. 1066-75.
46. Unterweger, H., et al., *Development and characterization of magnetic iron oxide nanoparticles with a cisplatin-bearing polymer coating for targeted drug delivery.* Int J Nanomedicine, 2014. **9**: p. 3659-76.
47. Hyeon, T., et al., *Synthesis of highly crystalline and monodisperse maghemite nanocrystallites without a size-selection process.* Journal of the American Chemical Society, 2001. **123**(51): p. 12798-12801.
48. Luchini, A., et al., *Developing functionalized Fe3O4-Au nanoparticles: a physico-chemical insight.* Phys Chem Chem Phys, 2015. **17**(8): p. 6087-97.
49. Groult, H., et al., *Phosphatidylcholine-Coated Iron Oxide Nanomicelles for In Vivo Prolonged Circulation Time with an Antibiofouling Protein Corona.* Chemistry – A European Journal, 2014. **20**(50): p. 16662-16671.
50. Mondini, S., et al., *Zwitterion-Coated Iron Oxide Nanoparticles: Surface Chemistry and Intracellular Uptake by Hepatocarcinoma (HepG2) Cells.* Langmuir, 2015. **31**(26): p. 7381-7390.
51. Muro, E., et al., *Small and Stable Sulfobetaine Zwitterionic Quantum Dots for Functional Live-Cell Imaging.* Journal of the American Chemical Society, 2010. **132**(13): p. 4556-+.
52. Kim, D., et al., *Facile preparation of zwitterion-stabilized superparamagnetic iron oxide nanoparticles (ZSPIONs) as an MR contrast agent for in vivo applications.* Langmuir, 2012. **28**(25): p. 9634-9.
53. Estephan, Z.G., J.A. Jaber, and J.B. Schlenoff, *Zwitterion-stabilized silica nanoparticles: toward nonstick nano.* Langmuir, 2010. **26**(22): p. 16884-9.
54. Price, E.W. and C. Orvig, *Matching chelators to radiometals for radiopharmaceuticals.* Chem Soc Rev, 2014. **43**(1): p. 260-290.
55. Gijs, M., et al., *Gallium-68-labelled NOTA-oligonucleotides: an optimized method for their preparation.* J Labelled Comp Radiopharm, 2015.
56. Wang, Z., et al., *Prospective Study of (68)Ga-NOTA-NFB: Radiation Dosimetry in Healthy Volunteers and First Application in Glioma Patients.* Theranostics, 2015. **5**(8): p. 882-9.
57. Chen, F., et al., *In Vivo Tumor Vasculature Targeting of CuS@MSN Based Theranostic Nanomedicine.* Acs Nano, 2015. **9**(4): p. 3926-34.
58. Kumar, A., et al., *Molecular platform for design and synthesis of targeted dual-modality imaging probes.* Bioconjug Chem, 2015. **26**(3): p. 549-58.
59. Yang, B.Y., et al., *Development of a multimodal imaging probe by encapsulating iron oxide nanoparticles with functionalized amphiphiles for lymph node imaging.* Nanomedicine (Lond), 2015. **10**(12): p. 1899-910.
60. Cho, B.B., et al., *Synthesis and characterization of Ga-68 labeled Fe3O4 nanoparticles for positron emission tomography (PET) and magnetic resonance imaging (MRI).* Journal of Radioanalytical and Nuclear Chemistry, 2015. **305**(1): p. 169-178.
61. Kim, S.M., et al., *Hybrid PET/MR imaging of tumors using an oleanolic acid-conjugated nanoparticle.* Biomaterials, 2013. **34**(33): p. 8114-8121.
62. Monopoli, M.P., et al., *Biomolecular coronas provide the biological identity of nanosized materials.* Nat Nanotechnol, 2012. **7**(12): p. 779-86.
63. Lynch, I. and K.A. Dawson, *Protein-nanoparticle interactions.* Nano Today, 2008. **3**(1-2): p. 40-47.
64. Milani, S., et al., *Reversible versus Irreversible Binding of Transferrin to Polystyrene Nanoparticles: Soft and Hard Corona.* Acs Nano, 2012. **6**(3): p. 2532-2541.
65. Montis, C., et al., *Interaction of nanoparticles with lipid membranes: a multiscale perspective.* Nanoscale, 2014. **6**(12): p. 6452-7.
66. Yue, T.T., X.R. Zhang, and F. Huang, *Molecular modeling of membrane responses to the adsorption of rotating nanoparticles: promoted cell uptake and mechanical membrane rupture.* Soft Matter, 2015. **11**(3): p. 456-465.
67. Mahmoudi, M., et al., *Interaction of stable colloidal nanoparticles with cellular membranes.* Biotechnol Adv, 2014. **32**(4): p. 679-92.
68. Simonelli, F., et al., *Monolayer-Protected Anionic Au Nanoparticles Walk into Lipid Membranes Step by Step.* The Journal of Physical Chemistry Letters, 2015. **6**(16): p. 3175-3179.

69. Santhosh, P.B., et al., *A study on the interaction of nanoparticles with lipid membranes and their influence on membrane fluidity.* 17th International School on Condensed Matter Physics (Iscmp): Open Problems in Condensed Matter Physics, Biomedical Physics and Their Applications, 2012. **398**.
70. Heikkila, E., et al., *Cationic Au Nanoparticle Binding with Plasma Membrane-like Lipid Bilayers: Potential Mechanism for Spontaneous Permeation to Cells Revealed by Atomistic Simulations.* Journal of Physical Chemistry C, 2014. **118**(20): p. 11131-11141.
71. Li, Z. and A.A. Gorfe, *Deformation of a Two-domain Lipid Bilayer due to Asymmetric Insertion of Lipid-modified Ras Peptides.* Soft Matter, 2013. **9**(47).
72. Tatur, S., et al., *Effect of Functionalized Gold Nanoparticles on Floating Lipid Bilayers.* Langmuir, 2013. **29**(22): p. 6606-6614.
73. Troiano, J.M., et al., *Direct Probes of 4 nm Diameter Gold Nanoparticles Interacting with Supported Lipid Bilayers.* Journal of Physical Chemistry C, 2015. **119**(1): p. 534-546.
74. Becucci, L., et al., *Interaction of Mixed-Ligand Mono layer-Protected Au-144 Clusters with Biomimetic Membranes as a Function of the Transmembrane Potential.* Langmuir, 2014. **30**(27): p. 8141-8151.
75. Lee, Y.K., et al., *Massively Parallel and Highly Quantitative Single-Particle Analysis on Interactions between Nanoparticles on Supported Lipid Bilayer.* Journal of the American Chemical Society, 2014. **136**(10): p. 4081-4088.
76. Mateo, C.R., A.U. Acuna, and J.C. Brochon, *Liquid-Crystalline Phases of Cholesterol Lipid Bilayers as Revealed by the Fluorescence of Trans-Parinaric Acid.* Biophysical Journal, 1995. **68**(3): p. 978-987.
77. Foglia, F., et al., *Interaction of Amphotericin B with Lipid Monolayers.* Langmuir, 2014. **30**(30): p. 9147-9156.
78. Vitiello, G., et al., *Fusion of raft-like lipid bilayers operated by a membranotropic domain of the HSV-type I glycoprotein gH occurs through a cholesterol-dependent mechanism.* Soft Matter, 2015. **11**(15): p. 3003-3016.
79. Vitiello, G., et al., *Cholesterol modulates the fusogenic activity of a membranotropic domain of the FIV glycoprotein gp36.* Soft Matter, 2013. **9**(28): p. 6442-6456.
80. Lind, T.K., et al., *Antimicrobial peptide dendrimer interacts with phosphocholine membranes in a fluidity dependent manner: A neutron reflection study combined with molecular dynamics simulations.* Biochim Biophys Acta, 2015. **1848**(10 Pt A): p. 2075-84.
81. Santhosh, P.B., et al., *Influence of nanoparticle-membrane electrostatic interactions on membrane fluidity and bending elasticity.* Chem Phys Lipids, 2014. **178**: p. 52-62.
82. Bailey, C.M., et al., *Size dependence of gold nanoparticle interactions with a supported lipid bilayer: A QCM-D study.* Biophysical Chemistry, 2015. **203**: p. 51-61.
83. Le Bihan, O., et al., *Cryo-electron tomography of nanoparticle transmigration into liposome.* J Struct Biol, 2009. **168**(3): p. 419-25.
84. Huang, J., J.T. Buboltz, and G.W. Feigenson, *Maximum solubility of cholesterol in phosphatidylcholine and phosphatidylethanolamine bilayers.* Biochim Biophys Acta, 1999. **1417**(1): p. 89-100.
85. Fuhrmans, M., et al., *Mechanics of membrane fusion/pore formation.* Chem Phys Lipids, 2015. **185**: p. 109-128.
86. Schulz, M., A. Olubummo, and W.H. Binder, *Beyond the lipid-bilayer: interaction of polymers and nanoparticles with membranes.* Soft Matter, 2012. **8**(18): p. 4849-4864.
87. Pera, H., et al., *Coverage and Disruption of Phospholipid Membranes by Oxide Nanoparticles.* Langmuir, 2014. **30**(48): p. 14581-14590.
88. Becker, C., et al., *Uptake of magnetic nanoparticles into cells for cell tracking.* Journal of Magnetism and Magnetic Materials, 2007. **311**(1): p. 234-237.
89. Biswas, N., et al., *Interplay of electrostatics and lipid packing determines the binding of charged polymer coated nanoparticles to model membranes.* Physical Chemistry Chemical Physics, 2015. **17**(37): p. 24238-47.
90. Lomakin, A., D. Teplow, and G. Benedek, *Quasielastic Light Scattering for Protein Assembly Studies*, in *Amyloid Proteins*, E. Sigurdsson, Editor. 2005, Humana Press. p. 153-174.
91. Kotlarchyk, M. and S.H. Chen, *Analysis of small angle neutron scattering spectra from polydisperse interacting colloids.* The Journal of Chemical Physics, 1983. **79**(5): p. 2461-2469.

92. Cubitt, R. and G. Fragneto, *D17: the new reflectometer at the ILL.* Applied Physics a-Materials Science & Processing, 2002. **74**: p. S329-S331.
93. Vorobiev, A., et al., *Recent upgrade of the polarized neutron reflectometer Super ADAM.* Neutron News, 2015. **26**(3): p. 25-26.
94. Devishvili, A., et al., *SuperADAM: Upgraded polarized neutron reflectometer at the Institut Laue-Langevin.* Review of Scientific Instruments, 2013. **84**(2): p. 025112.
95. Fragneto-Cusani, G., *Neutron reflectivity at the solid/liquid interface: examples of applications in biophysics.* Journal of Physics-Condensed Matter, 2001. **13**(21): p. 4973-4989.
96. Gerelli, Y., *Aurore: new software for neutron reflectivity data analysis.* Journal of Applied Crystallography, 2016. **49**(1): p. 330-339.
97. Parratt, L.G., *Surface Studies of Solids by Total Reflection of X-Rays.* Physical Review, 1954. **95**(2): p. 359-369.
98. Höök, F., *Development of a Novel QCM Technique for Protein Adsorption Studies*, ed. n. Doktorsavhandlingar vid Chalmers tekniska högskola. Ny serie. 1997, Göteborg: Department of Applied Physics, Chalmers University of Technology.
99. Cans, A.S., et al., *Measurement of the dynamics of exocytosis and vesicle retrieval at cell populations using a quartz crystal microbalance.* Analytical Chemistry, 2001. **73**(24): p. 5805-5811.
100. *National Bureau of Standars (U. S.) Monograph 25.* 1967. **5**.
101. Noginov, M.M., et al., *Magnetic resonance in iron oxide nanoparticles: Quantum features and effect of size.* Journal of Magnetism and Magnetic Materials, 2008. **320**(18): p. 2228-2232.
102. Livingston, C.P.B.a.J.D., Journal of Applied Physics, 1959. **30**(120S).
103. Armen, R.S., O.D. Uitto, and S.E. Feller, *Phospholipid component volumes: Determination and application to bilayer structure calculations.* Biophysical Journal, 1998. **75**(2): p. 734-744.
104. Wennerström, H., J. Morris, and U. Olsson, *Homogeneous Nucleation in an Emulsion/Droplet Microemulsion System.* Langmuir, 1997. **13**(26): p. 6972-6979.
105. Stafford, R.E., T. Fanni, and E.A. Dennis, *Interfacial Properties and Critical Micelle Concentration of Lysophospholipids.* Biochemistry, 1989. **28**(12): p. 5113-5120.
106. Neugebauer, J.M., *Detergents - an Overview.* Methods in Enzymology, 1990. **182**: p. 239-253.
107. Na, H.B., I.C. Song, and T. Hyeon, *Inorganic Nanoparticles for MRI Contrast Agents.* Advanced Materials, 2009. **21**(21): p. 2133-2148.
108. Menichetti, L., et al., *Iron Oxide-Gold Core-Shell Nanoparticles as Multimodal Imaging Contrast Agent.* Ieee Sensors Journal, 2013. **13**(6): p. 2341-2347.
109. Bulte, J.W.M., et al., *Frequency dependence of MR relaxation times II. Iron oxides.* Journal of Magnetic Resonance Imaging, 1993. **3**(4): p. 641-648.
110. Ruiz, A., et al., *Short-chain PEG molecules strongly bound to magnetic nanoparticle for MRI long circulating agents.* Acta Biomaterialia, 2013. **9**(5): p. 6421-6430.
111. Mulder, W.J.M., et al., *Lipid-based nanoparticles for contrast-enhanced MRI and molecular imaging.* Nmr in Biomedicine, 2006. **19**(1): p. 142-164.
112. Tanimoto, A., et al., *Relaxation effects of clustered particles.* Journal of Magnetic Resonance Imaging, 2001. **14**(1): p. 72-77.
113. Boni, A., et al., *Design and optimization of lipid-modified poly(amidoamine)dendrimer coated iron oxide nanoparticles as probes for biomedical applications.* Nanoscale, 2015. **7**(16): p. 7307-7317.
114. de Meyer, F. and B. Smit, *Effect of cholesterol on the structure of a phospholipid bilayer.* Proc Natl Acad Sci U S A, 2009. **106**(10): p. 3654-8.
115. McMullen, T.P.W., R.N.A.H. Lewis, and R.N. McElhaney, *Cholesterol–phospholipid interactions, the liquid-ordered phase and lipid rafts in model and biological membranes.* Current Opinion in Colloid & Interface Science, 2004. **8**(6): p. 459-468.
116. Krzyzanowski, N., et al., *Reply to the 'Comment on "Cholesterol Solubility Limit in Lipid Membranes probed by Small Angle Neutron Scattering and MD simulations"' by R. Epand, Soft Matter, 2015, 11, DOI: 10.1039/C4SM02819H.* Soft Matter, 2015. **11**(27): p. 5582-5584.
117. Shabtai, Y. and D.L. Gutnick, *Tolerance of Acinetobacter calcoaceticus RAG-1 to the cationic surfactant cetyltrimethylammonium bromide: role of the bioemulsifier emulsan.* Appl Environ Microbiol, 1985. **49**(1): p. 192-7.
118. Wacklin, H.P., *Neutron reflection from supported lipid membranes.* Current Opinion in Colloid & Interface Science, 2010. **15**(6): p. 445-454.

119. Wacklin, H.P., *Composition and asymmetry in supported membranes formed by vesicle fusion.* Langmuir, 2011. **27**(12): p. 7698-707.
120. Berkowitz, M.L., *Detailed molecular dynamics simulations of model biological membranes containing cholesterol.* Biochim Biophys Acta, 2009. **1788**(1): p. 86-96.
121. de Almeida, R.F.M., A. Fedorov, and M. Prieto, *Sphingomyelin/Phosphatidylcholine/Cholesterol Phase Diagram: Boundaries and Composition of Lipid Rafts.* Biophysical Journal, 2003. **85**(4): p. 2406-2416.
122. Montis, C., et al., *Nucleolipid bilayers: A quartz crystal microbalance and neutron reflectometry study.* Colloids and Surfaces B-Biointerfaces, 2016. **137**: p. 203-213.
123. Vitiello, G., et al., *Cationic liposomes as efficient nanocarriers for the drug delivery of an anticancer cholesterol-based ruthenium complex.* Journal of Materials Chemistry B, 2015. **3**(15): p. 3011-3023.
124. Mangiapia, G., et al., *Anticancer cationic ruthenium nanovectors: from rational molecular design to cellular uptake and bioactivity.* Biomacromolecules, 2013. **14**(8): p. 2549-60.
125. Simeone, L., et al., *Cholesterol-based nucleolipid-ruthenium complex stabilized by lipid aggregates for antineoplastic therapy.* Bioconjug Chem, 2012. **23**(4): p. 758-70.
126. Montesarchio, D., et al., *A new design for nucleolipid-based Ru(III) complexes as anticancer agents.* Dalton Trans, 2013. **42**(48): p. 16697-708.
127. Mangiapia, G., et al., *Ruthenium-based complex nanocarriers for cancer therapy.* Biomaterials, 2012. **33**(14): p. 3770-82.
128. Higgins, J.S.B., H. C., *Polymers and Neutron Scattering* 1997: Oxford Series on Neutron Scattering in Condensed Matter.
129. Roe, R.J., *Methods of X-ray and neutron scattering in polymer science*. 2000: Oxford University Press.
130. Wadsater, M., et al., *Aligning nanodiscs at the air-water interface, a neutron reflectivity study.* Langmuir, 2011. **27**(24): p. 15065-73.
131. Cardenas, M., et al., *Structure of DNA-cationic surfactant complexes at hydrophobically modified and hydrophilic silica surfaces as revealed by neutron reflectometry.* Langmuir, 2011. **27**(20): p. 12506-14.